High-Resolution Study of the O_2 *A*-Band using Frequency Stabilized Cavity Ring-Down Spectroscopy

Thesis by

David J. Robichaud

In partial fulfillment of the requirements

For the Degree of
Doctor of Philosophy

California Institute of Technology
Pasadena, California

2008

(Defended October 31, 2007)

ACKNOWLEDGEMENTS

There are of course many people worth thanking throughout my graduate career. First and foremost I would like to thank my advisors Drs. Mitchio Okumura and Pin Chen. Both Mitchio and Pin have been fantastic advisors and I've learned many scientific and technical skills from them.

Much of my time as a graduate student was spent at JPL. I've worked with many fantastic researchers including Drs. Stan Sander, Charles Miller, and Linda Brown. They have all influenced my scientific development over the years and have shown great enthusiasm for the projects we've worked on. In addition, I'd like to thank the basement of 231: Brian Drouin and Tim Crawford and the many postdocs (particularly Drs. Leah Alconcel and Jaron Hansen) and staff (Dave Natzic) I've encountered at JPL. It was always a pleasure to sit and chat on topics ranging from the completely mundane to scientifically abstract. I'd also like to thank my collaborators from NIST: Drs. Joseph Hodges and Daniel Lisak as well as Piotr Maslowski – without whom the bulk of this thesis would not have been possible.

Of course any acknowledgements section cannot be complete without thanking the little people. And by that I mean the Okumura group: Andrew Mollner, Julie Fry, Aaron Noell, Kana Takematsu, Laurence Yeung, Matt Sprague, and Kathleen Spencer – not one of them taller than a hobbit. I felt like a giant, and have the concussion to prove it (thanks Kana). This group of people definitely made graduate life fun with our weekly

croquet games, beach trips, and yearly camping trips (which I seem to always have missed). In particular I'd like to thank the incoming class of 2001 (Julie and Andrew). Julie showed me just how many different things can be accomplished if you set your mind to it and Andrew showed me how to take it all in stride.

Finally I would like to thank all those outside of research, particularly my rock-climbing friends Aaron Stern, Joe Olivier, Vera Pavel, Stephanie Chow, and the crew at Hanger 18. No matter how bad research was I knew I could count on a trip to Joshua Tree to ease the tensions (and scrape the knuckles). And lastly to my family, not only for support and a stubborn insistence to never understand what I've done these last 6 years, but for food, laundry, and a place to sleep.

ABSTRACT

This thesis describes laboratory measurements of the O_2 *A*-band spectrum using frequency stabilized cavity ring-down spectroscopy (FS-CRDS). The FS-CRDS allowed the collection of high-resolution (<1 MHz) spectra in conjunction with the exception sensitivity of the CRDS technique. Line positions were measured with an accuracy better than 2×10^{-5} cm^{-1} by calibrating our spectra against the hyperfine components of ^{39}K *D* lines. Line parameters were determined using a variety of lineshape models from the standard Voigt profile to models incorporating speed dependence and collisional narrowing. Clear deviations are shown between the observed and Voigt profiles, while the other profiles considered were found to fit the observed lineshapes well. Line intensities obtained using the Galatry profile are compared with previously measured values and found to be approximately 1% smaller than intensities found in current databases. Many of the other lineshape parameters are in good agreement with previous measurements. However, the pressure-induced shifts of the current work are considered much more accurate than other studies. Finally we report on the line parameters of each of the isotopologues of O_2.

TABLE OF CONTENTS

List of Figures

List of Tables

CHAPTER 1

Frequency-Stabilized Cavity Ring-Down Spectroscopy

1.1. Introduction

The experimental apparatus used to study the O_2 *A*-band is located in Dr. J. T. Hodges laboratory at the National Institute of Technology (NIST) in Gaithersburg, MD.[1-4] The technique is referred to as frequency-stabilized cavity ring-down spectroscopy (FS-CRDS) and is a variant on the established *cw*-cavity ring-down spectroscopy method.

1.1.1. cw-Cavity Ring-Down Spectroscopy

Cavity ring-down spectroscopy is based on the principle that the rate at which light intensity within an optical cavity decays is dependent on both fixed cavity losses (e.g. scattering, absorption, or transmission at the mirrors) and absorption by an analyte gas within the cavity. Light from a laser is first injected into the optical cavity through one of the mirrors, effectively trapping the light within the cavity. This thereby increases the interaction time of the light with the absorbing medium, or in terms of Beer-Lambert's Law, Abs = $\sigma(\lambda)N\,l$, it increases the effective pathlength of the spectrometer. The intensity of the circulating light within an evacuated cavity is attenuated upon each roundtrip due to the losses described above. Transmission through the mirrors upon each roundtrip results in an exponential decay of optical power which can be monitored using a photodetector external to the cavity. The subsequent "ring-down" of the optical cavity is then fit using an exponential function to extract the ring-down time, τ,

$$I(t) = I_0\, e^{\frac{-(1-R)tc}{L_{total}}} \quad \text{with} \quad \tau = \frac{t_r}{2[(1-R)+\alpha L_{eff}]} \quad . \tag{1.1}$$

Comparison of the empty cavity ring-down time ($\alpha = 0$) and that with an absorber ($\alpha = \sigma(\lambda)N$ ($\sigma(\lambda)$ is the cross section of the absorbing gas at the laser wavelength λ and N is the number density) is proportional to the absorbance of the analyte:

$$\alpha = \frac{1}{c}\left(\frac{1}{\tau_{\alpha}} - \frac{1}{\tau_{\alpha=0}}\right). \qquad (1.2)$$

The CRDS technique in general possesses two primary advantages over other high-sensitivity absorption methods: it uses small sample volumes (typically <500 cm^3) and it is insensitive to laser power fluctuations. In addition, *cw*-CRDS gains further advantages over pulsed-CRDS due to the use of very narrow band cw-lasers including: higher resolution (< 10^{-4} cm^{-1}), higher acquisition rates (100 – 1000 Hz) resulting in more averaging per unit time, and better sensitivity due to single mode excitation. The last is especially important in quantitative spectroscopy; multimode excitation using pulsed CRDS has been shown to be non-linear with increasing absorption [5-7]. The drawbacks to *cw*-CRDS are: scanning is time consuming, taking 20+ hours to acquire 100 cm^{-1} due to smaller spectral step-size; *cw*-lasers typically have narrow tuning ranges (10's to 100's of cm^{-1}); and the setup is generally more demanding in regard to alignment of the optical setup and peripheral equipment (e.g. AOMs, isolators, etc).

The optical cavity modes must be considered when performing *cw*-CRDS. The most commonly used optical cavity (and that which is used throughout this thesis) is a Fabry-Perot ètalon comprised of two spherical mirrors with radius of curvature r and separated by a distance l. Because the light within the cavity is circulating between the

two mirrors, it will either constructively or destructively interfere depending on the phase condition on a given roundtrip of the optical cavity. This phase relationship (which is dependent on the wavelength of the laser) results in the presence of cavity modes (narrow wavelength windows with high intra-cavity buildup) with resonant frequencies as described by the Gauss-Hermite transverse, TEM_{mn}, modes [8] :

$$\nu_{qmn} = \frac{c}{2n_0 l}\left\{q + \frac{m+n+1}{\pi}\cos^{-1}\left(1-\frac{l}{r}\right)+\theta\right\}, \tag{1.3}$$

where c is the speed of light, q is the longitudinal mode order, m and n are the transverse mode orders, n_0 is the real part of the index of refraction, and l is the mirror separation. The distance between any two consecutive longitudinal modes with given mn is defined as the free-spectral-range (FSR) as

$$FSR = \frac{c}{2n_0 l}. \tag{1.4}$$

Each cavity mode can be represented by a Lorentzian lineshape with a full width at half maximum given by FSR/finesse. For the cavity used in these experiments with a finesse of 15,000 and an FSR of 202 MHz, the mode width is 13.5 kHz. This width is significantly smaller the instantaneous laser linewidth (~100 kHz) and therefore limits the amount of power that can be effectively coupled into the ring-down cavity. For a 1 mW input into the optical cavity, the peak transmission is less than 1 μW.

1.1.2. Frequency Stabilized-Cavity Ring-Down Spectroscopy

The frequency stabilized-cavity ring-down setup (FS-CRDS) setup located in Dr. Hodges laboratory at NIST was described in detail previously [1-4]. A unique feature of the FS-CRDS setup is that the mirror-to-mirror distance of the optical cavity is actively

stabilized with respect to a frequency-stabilized HeNe laser (0.5 MHz long term uncertainty). This approach, which is used to compensate for variations in the optical pathlength, has the inherent benefit that the spectrum frequency axis is now linked to two precisely measured quantities: the free-spectral-range (FSR) of the ring-down cavity and the frequency shift of the probe laser, determined by counting the number of cavity modes from an arbitrary reference point. Spectra are acquired by step scanning the probe laser over sequential mode orders q of the locked ring-down cavity and by tuning the resonance frequencies of the cavity using a variable-frequency acousto-optic modulator (AOM). The AOM shifts the reference laser frequency, to which the cavity is actively stabilized, and in turn tunes the probe laser frequency by a known amount as given in Eq. 1.5. The underlying premise is that individual resonances of the ring-down cavity can be selectively excited, thus yielding a spectral resolution that is limited by the stability of the cavity modes yet insensitive to variations in the probe laser frequency.

$$\nu_{probe} = \frac{c}{2nl}\Delta q - (2\Delta f_A - \Delta\nu_{HeNe})\frac{\nu_{probe}}{\nu_{HeNe}} + \nu_{ref}\ , \qquad (1.5)$$

where ν_{HeNe} is the stabilized HeNe laser frequency, c is the speed of light, n is the index of refraction of the O_2, l is the effective mirror-to-mirror distance of the ring-down cavity, and ν_{ref} is the reference position (e.g. a saturation dip of ^{39}K). In addition, Δq , Δf_A and $\Delta\nu_{HeNe}$ are the respective changes in longitudinal mode order, AOM frequency and HeNe frequency, and these three changes are with respect to an arbitrary set of reference values for which Eq. 1.3 satisfies the condition $\nu = \nu_{ref}$. The quantity $c/2nl$ is equal to the FSR, which varies with gas density due to the density dependence of n. Therefore, the FSR must be measured for each temperature and pressure condition of the gas sample.

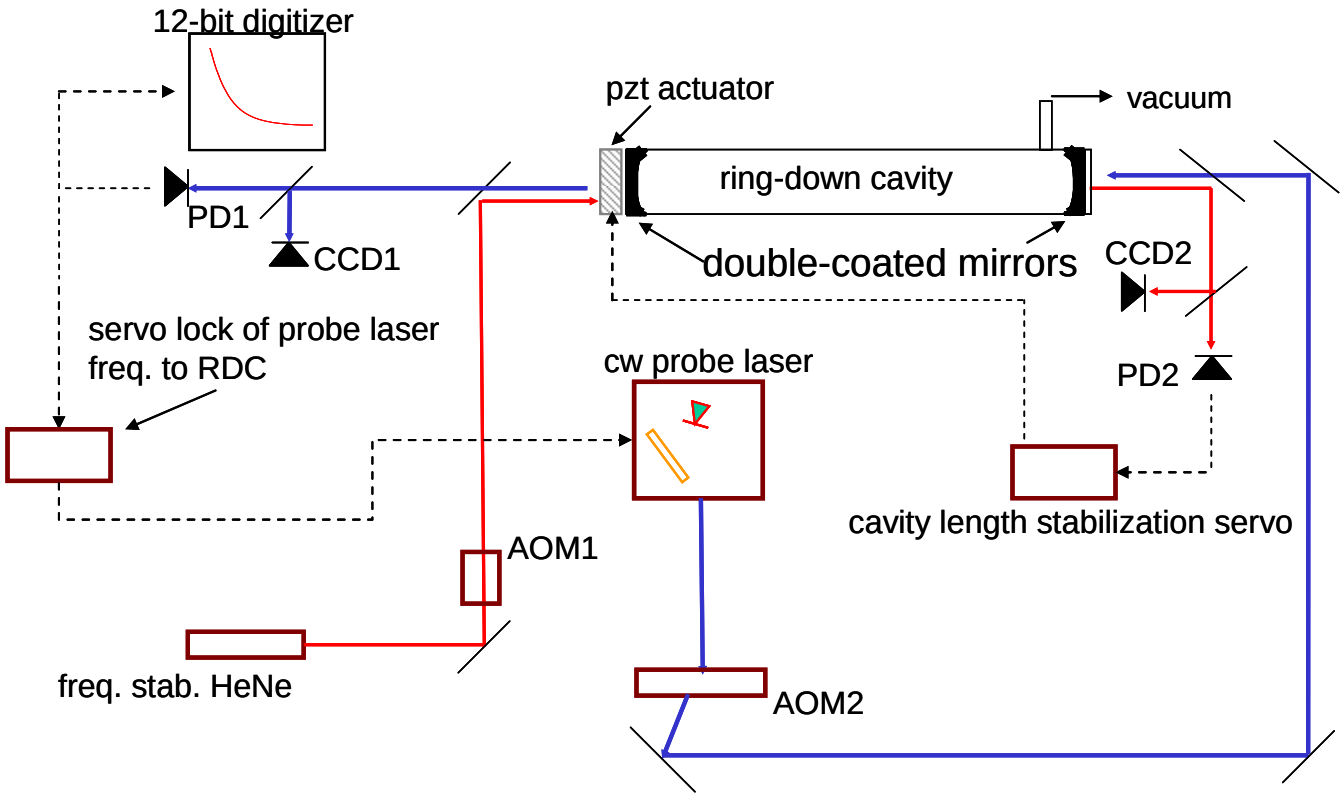

Figure 1.1. Schematic diagram of the FS-CRDS system. Dashed and solid lines indicate electrical connections and optical beams, respectively. AOM: acousto-optic modulator. PD1 – Si-PIN photodetector, 8 MHz bandwidth for ring-down detection; PD2 Si photodetector, 50 kHz bandwidth to lock cavity mode to HeNe wavelength. CCD1 and CCD2: charged-coupled device camera to monitor excited cavity mode structure of probe and HeNe laser, respectively.

The experimental setup is depicted in Fig. 1.1 and will be described in its five components: the optical cavity, cavity-to-HeNe lock, probe laser-to-cavity lock, acquisition and scanning, and sample preparation.

Optical Cavity

The optical cavity is formed using two plano-concave mirrors coated for two reflectivity peaks: the first at 633 nm with R~95% to lock the cavity to the HeNe reference, the second is R~99.98% at the probe wavelength of 760 nm to perform ring-down measurements (see Fig. 1.2 for mirror reflectivity as a function of probe wavelength). The second surfaces of the ring-down mirrors were anti-reflective coated to reduce fringing effects between the ring-down mirrors and other optics/surfaces (e.g. the detector). The cavity was constructed out of stainless steel and vacuum sealed using conflat flanges and VCR connections. The air-to-vacuum interface was two MDC glass-to-metal viewports, both of which were anti-reflective coated at 760 and 633 nm respectively, by Spectrum Thin Films. The pressure within the cell was measured over a 24 hour period, and the leak rate was determined to be less than 1 mtorr/day (Fig. 1.3). No effort was used to distinguish between real leaks and virtual leaks (outgassing), and the reported leak rate should be considered the sum of all possible leaks. The mirror-to-mirror distance was nominally 74 cm, and four invar rods were used to minimize temperature fluctuations of the cavity length. This length was chosen specifically to maximize the distance between the TEM_{00} modes and other higher order modes (see Section 1.2.1 for further details). The back mirror was placed upon a piezoelectric

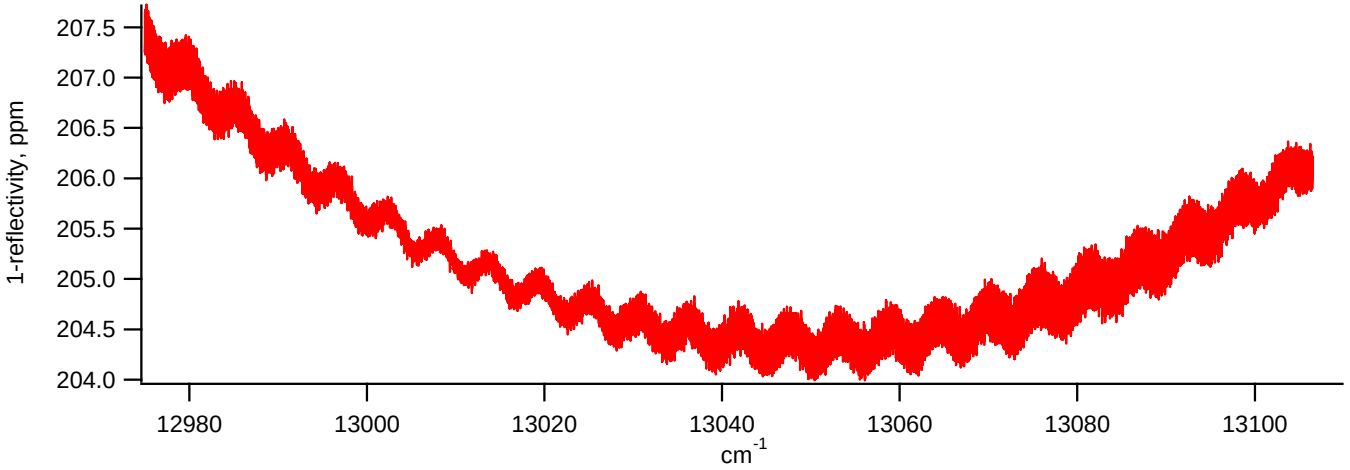

Figure 1.2. Empty cavity scan of the optical cavity. Peak reflectivity is at 13050 cm^{-1}. Scan shows presence of an ètalon with FSR = 5.6 cm^{-1}, corresponding to a 0.8 mm length.

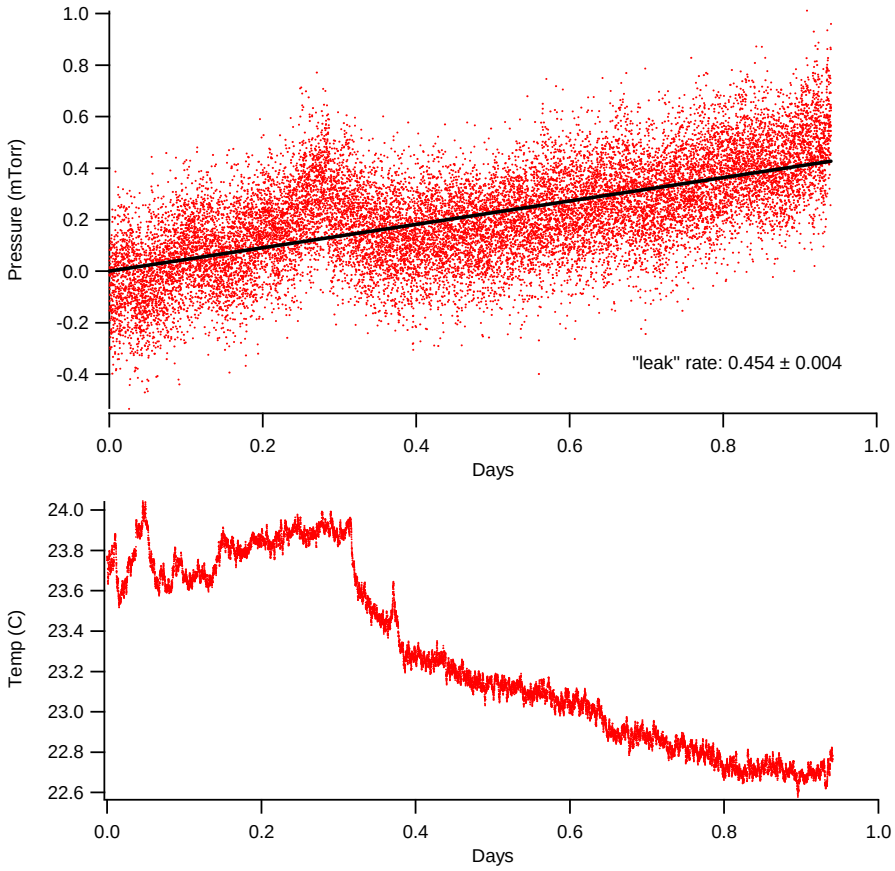

Figure 1.3. Leak rate measurement. Top: pressure measurements (dots) and linear fit (solid line). Leak rate is less than 1 mTorr/day. Bottom: simultaneous temperature measurement. Leak rate in this context is the sum of all virtual (e.g. outgassing) and real leaks.

transducer (pzt) and was used to stabilize the cavity length with respect to the HeNe reference laser. Both the probe laser and the HeNe were mode-matched to TEM_{00} modes of the optical cavity and were counter-propagating through the cavity with respect to each other.

The cell temperature was monitored using a NIST calibrated thermistor (maximum uncertainty <0.1%) in direct thermal contact with the outside of the cell. No effort was used to stabilize or control the temperature of the cell. Over a typical scan (15 minutes) the temperature did not drift by more than 0.1 K, and the 24-hour drift was < 2 K. Cell pressure was monitored using one of two MKS baratron gauges (100 Torr and 1000 Torr heads) recently calibrated by the NIST Pressure and Vacuum group, with maximum uncertainties of 0.01%.

Cavity-to-HeNe Lock

A polarization-stabilized HeNe laser (Melles Griot, linewidth <1 MHz) was used to stabilize the optical cavity length and was counter-propagated through the optical cavity relative to the probe laser (New Focus 6323 external cavity diode laser). The HeNe was modulated at 20 kHz using a double-pass configuration through an

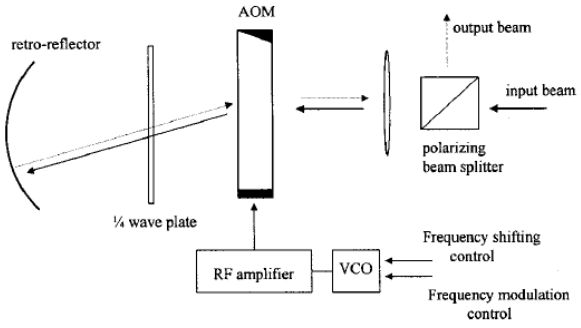

Figure 1.4. Schematic of the double-pass AOM system used for frequency modulating of the frequency stabilized HeNe laser. As f_{AOM} changes, the diffraction angle on the first pass changes proportionally. However, after passing through the AOM on reflection the beam direction remains unchanged. This allows tuning and modulation of the AOM without re-alignment of the HeNe beam with respect to the optical cavity. Figure taken from Ref 2.

acousto-optic modulator (AOM) as depicted in Figure 1.4. The double pass configuration was used to eliminate the diffraction of the HeNe beam due to the AOM, effectively making the beam position insensitive to frequency-dependent shifts caused by the AOM. In addition to modulating the AOM at 20 kHz, a DC voltage was applied in order to shift the HeNe frequency from its nominal wavelength. This enabled us to slightly alter the length of the optical cavity in order to collect data with step sizes less than the FSR of the cavity, as depicted in Eq. 1.5.

The cavity length was servo-locked to the laser in a proportional-integrator feedback scheme using a pzt on the back mirror. The proportional signal was generated using a lock-in amplifier at twice the AOM modulation frequency, and the integration component was computer generated using LabVIEW with a time constant of approximately 0.5 seconds. The cavity-to-HeNe lock was monitored using a CCD camera to ensure the HeNe was matched to a TEM_{00} mode of the cavity. Although the cavity-to-HeNe lock was quite robust, several effects were determined to influence the length of the cavity and thus our ability to maintain the lock. The most obvious influence of the cavity length is thermal expansion of the optical cavity. To minimize this, invar spacers (thermal expansion 1×10^{-7}/K) were placed between the mirror mounts. Second, pressure changes within the optical cavity will alter the refractive index and, therefore, the position of the cavity modes, according to Eq. 1.3. This will be discussed in more detail in a Chapter 3; for now, the maximum change in pressure can be changed and maintain lock is ~40 Torr. Finally, because the bandwidth of the lock is small,

purposefully changing the cavity length (e.g. when scanning using the AOM) too quickly can disrupt the lock placing a practical limit on the scanning speed of the instrument.

In addition to the polarization stabilized HeNe, a second I_2-stabilized HeNe laser is used in some of these experiments. The I_2-stabilized HeNe was designed and constructed by Dr. Howard Layer (NIST). In this laser an I_2 cell is placed inside the laser cavity and the HeNe frequency is locked to a specific ro-vibronic I_2 transition near 632.8 nm with a long-term (24 hours) absolute stability of <5 kHz. Unfortunately, the output power of the I_2-stabilized HeNe was insufficient to use to stabilize the optical cavity. Instead, a portion of the Melles Griot laser was diverted and beat against the I_2-stabilized HeNe laser, allowing for correction for short and long term drift of the Melles Griot HeNe.

Probe Laser-to-Cavity Lock

The probe laser was a New Focus model 6323 external cavity diode laser (ECDL, P 3-8 mW, linewidth ~ 200 kHz) which covered the wavelength range of 763-782 nm. The ECDL could be fine tuned up to 2.5 cm^{-1} using a piezo-electric transducer (PZT) and coarse tuned using a stepper motor (step size approximately 0.3 cm^{-1}) either manually or computer-controlled through a serial GPIB connection. An external ètalon was used to monitor the probe laser wavelength and to look for evidence of mode-hopping or multimode effects in the laser frequency. Near the edge of the tuning range (13,080 – 13,115 cm^{-1}) a significant drop in laser power (P < 1 mW) was evident, which made scanning in that region difficult. Two OFR optical isolators (~35 dB each) were used to

eliminate optical feedback to the laser. The zeroth order output of the AOM was sent to a Burleigh wavemeter (WA-1500, resolution 60 MHz) to monitor the absolute wavelength of the laser. The first order output of the AOM was passed through two turning mirrors and mode-matching optics and coupled to the TEM_{00} mode of the optical cavity. The transmission of the laser was split (90:10) to a Si-PIN photodiode (New Focus 2051, BW ~ 8 MHz) to monitor ring-down events and a CCD camera to observe the mode structure, respectively. The alignment of the laser to the TEM_{00} mode of the cavity was confirmed both by the image of the CCD camera and by modulating the laser greater than the cavity FSR and observing the transmission pattern on an oscilloscope. The majority of the laser power was clearly matched to the TEM_{00} mode; however, ~10-15% of the power was coupled to higher-order modes (see Figure 1.5).

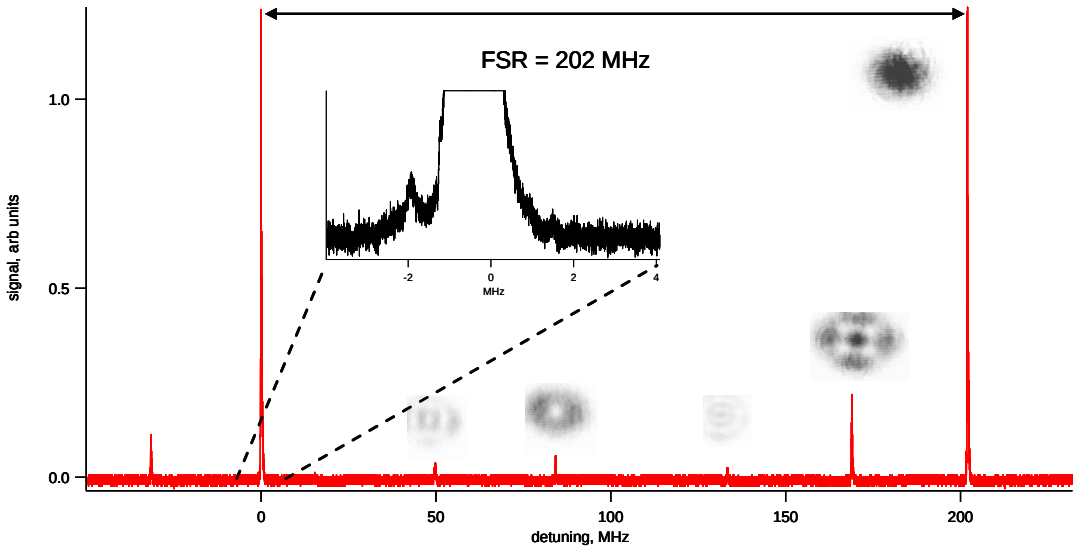

Figure 1.5. Transmission of the optical cavity over one free-spectral range. Cavity modes as seen by a CCD camera are shown next to their respective peaks. Inset shows a weak mode nearly degenerate with the TEM_{00} mode.

The probe laser was servo-locked to the optical cavity as follows. The laser was stepped along a triangle wave path using a computer and LabVIEW program. As the laser went in and out of resonance with a cavity mode, a complicated pattern of transmission bursts of various intensities would occur and was recorded using the Si photodetector. If the bursts were sufficiently strong, they would trigger a digital delay generator and produce a TTL pulse sent to the computer and recorded. The LabVIEW program monitored the location and occurrence of these bursts, generating a probability density of the integrated DDG output and indicating the cavity mode resonant frequency in relation to the center of the triangle wave. The program would adjust the laser frequency to maintain the centroid of the probability density in the center of the triangle wave. It was generally straightforward to discriminate locking to the TEM_{00} mode versus other modes by setting the DDG trigger to an appropriate level. The second DDG was used to trigger AOM2 to switch off the laser power and allow for a clean, single exponential decay. Figure 1.6 shows a typical sequence of transmission bursts encountered when locking the probe laser and the subsequent outputs of the two DDGs. This soft-locking method was developed for use with a T-optica ECDL, which has considerable more laser frequency noise than the New Focus laser used here. As such, it

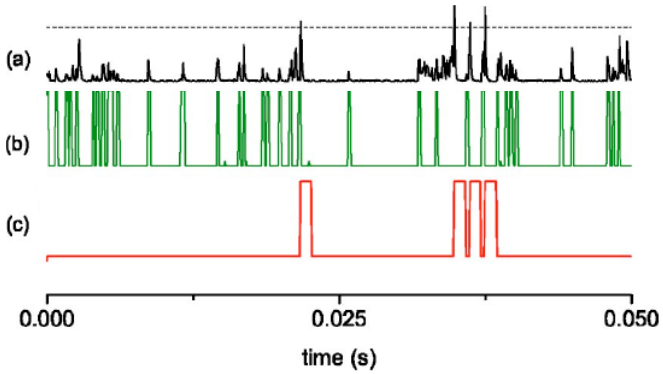

Figure 1.6. Signals used in cavity stabilization servo: (a) cavity transmission when probe laser frequency is near a cavity mode (dashed line is the trigger threshold for ring-down events); (b) output of DDG2 used to lock the probe laser to the cavity; and (c) output of DDG1 used to switch off AOM2 and initiate a ring-down decay. Figure reproduced from Ref 1.

was difficult to lock the New Focus laser if the step size of the triangle wave was too large. A work-around used in this study was to modulate the current of the diode laser at 500 Hz with a depth of 2 MHz. This effectively broadened the New Focus laser linewidth enough for the locking method to work well.

Acquisition and Scanning

Ring-down events were recorded using a Si-PIN photodiode (New Focus Model 2051, 8 MHz) and transferred to the computer using a 12 bit digitizer at 25 MS/s (Gage 12100). The ring-down decays were fit to a single exponential using a fast-fitting algorithm [9] with a typical uncertainty, $\Delta\tau/\tau$, of 0.07% and a nominal instrument sensitivity of 6×10^{-10} cm^{-1} $Hz^{-1/2}$ with 200 ppm mirrors (finesse ~15,000). Occasionally, a close lying, higher order mode (Figure 1.5) would trigger a ring-down event, which was evident by both a marked increase in $\frac{\Delta\tau}{\tau}$ and a decrease in the average ring-down time. In addition, the bandwidth of the photodetector could influence the ring-down decay if the decay was too fast. It was empirically determined that an 8 MHz detector could be used to record decays as fast as 4 μs (600 ppm losses for these experiments) or a rule of thumb of $\tau_{min} = 30/BW$. Ideally for these experiments the photodetector should have a bandwidth of 20 MHz for a minimum lifetime of 1.5 μs (1600 ppm losses). However, no photodetector of sufficient bandwidth, gain, and noise is commercially available. Once the lifetime is reduced below 3 μs, the transmitted light intensity is significantly attenuated due to absorption. Therefore, even with a faster photodetector the upper limit on absorption could not exceed 800 ppm.

The setup is controlled by two computers connected via the RS-232 ports. A master computer collects and fits the ring-down decays, records data such as temperature and pressure, and synchronizes its operations with the slave computer. The slave computer locks the probe laser to the cavity and scans the probe laser by either jumping cavity modes or tuning the length of the cavity (and thereby moving the cavity mode). Initially, ring-down events were recorded, fit, and displayed on the computer at 20-30 Hz, which seemed slow. Indeed, the theoretical limit for collecting 100 μs decays is 5 kHz (allowing a generous additional 100 μs for ring-up of power in the cavity). Testing of the capture rate of the computer alone (only acquiring the decays, no fitting, calculations, or displaying of graphics) showed a practical limit of ~ 600 Hz. A vast difference from the typical acquire/fit rate and limited by the time it takes for the laser to become resonant with the cavity mode (i.e. seek time). It was determined that turning off all graphics on the front panel of LabVIEW and streamlining the code (e.g. removing repetitive calculations from for-loops that could be performed outside the loop) increased the acquire + fit speed to 300 Hz – a 10 fold improvement. The acquisition speed could be further enhanced through such means as using a faster computer (i.e. reducing the fitting time), removing the fitting algorithm from the acquisition loop and performing fits during less critical times (i.e. while the laser is scanning using the slave computer), or locking the probe laser to the cavity using the Pound-Drever Hall technique [10, 11] (reducing the "seek time") instead of the looser servo-lock described above. The latter would also have the added benefit of improving the scan time and increasing the transmitted power of the laser, thereby increasing the signal-to-noise of the ring-down decay.

Sample Preparation and Data Collection

All experiments were performed in the static 200 mL ring-down cavity described above. Specific sample preparation details are described in later chapters. Line parameter scans were performed over a 6-20 GHz window centered on a specific transition at 50 MHz steps. Survey scans were performed continuously from 12,975 cm^{-1} to 13,000 cm^{-1} by jumping cavity modes (200 MHz steps). Pressure and temperature readings were taken every 10 mode jumps. A wavemeter reading was taken at every data point and was used to confirm that the laser was not skipping cavity modes during a scan.

For all measurements the total cell pressure used was determined based on the strength of the individual lines. The maximum absorption that could be measured without being influenced by the detector bandwidth was 600 ppm. Therefore, a transition such as $^{P}Q(20)$ of the O_2 *A*-band with a line strength of 1.3×10^{-24} $cm^{-1}/(cm^{-2}$ molecule) could be recorded up to 17 torr in air (21% O_2/N_2). The minimum pressure used was the greater of 1 torr or when the signal-to-noise was approximately 500. All experiments were performed at room temperature ($23 \pm 2^{o}C$).

Recommended Modifications to the Instrument

There are several improvements that can be made to the instrument that are anticipated to increase scanning speed, sensitivity, and robustness. They are outlined here for anyone looking to build one of these instruments.

1. Analog cavity-to-HeNe servo-lock: The current setup using computer integration is slow, with a time constant of ~0.5 seconds, and suffers from additional noise due to the analog-to-digital and digital-to-analog conversions. This limits the ability of the cavity to track the HeNe frequency when fine tuning is attempted, and therefore the laser must be tuned slowly. An analog integration should greatly improve the tracking speed of this lock and should be limited primarily by the bandwidth of the PZT controlling the optical cavity length (approximately 1 kHz). This could reduce the tuning time by up to 30-50% (currently the time is ~3 seconds for a 50 MHz tune). In addition, this reduces the number of computers from three to two.
2. Program enhancements: There are several sections of the program that can be streamlined to improve the data acquisition speed. In addition, taking advantage of multi-core functionality of LabVIEW could increase fitting speed of the ring-down decays.
3. Using a 14- or 16-bit digitizer: It has been put forth in the literature that digitizing noise can cause the measured lifetime to deviate from the true value. Therefore, increasing the resolution of the digitizer used should give a more accurate representation of the true ring-down time within the cavity. Many companies produce 14-bit digitizers that are sufficiently fast to use in cavity ring-down spectroscopy. Fast 16-bit digitizers are harder to come by, but as technology advances these boards will be more commercially available.
4. Faster low-noise detector: The current detector, New Focus model 2051, has a bandwidth of approximately 8 MHz and a noise level of ~5 mV_{pp}. This

corresponds to a minimum ring-down time of 4 μs (effectively 600 ppm cavity losses) before the detector bandwidth adversely affects the measured lifetime. A bandwidth of 20 MHz would reduce the minimum ring-down time to 1.5 μs (or 1500 ppm). Generally, we avoid losses over 800 ppm due to attenuation of light within the cavity; thus our detection would no longer be bandwidth-limited but limited by the transmission of light.

5. Pound Drever Hall (PDH) locking the probe laser to the cavity mode: PDH locking has three primary advantages. First the average transmitted power will be significantly higher (~ 10x) than an unlocked laser, resulting in improved signal to noise in the ring-down decay. Second, the acquisition rate will no longer be limited by the "seek" time (i.e. the time it takes for the laser to become resonant with a cavity mode). Finally, PDH locking should substantially reduce the influence of mode competition in the ring-down decays, improving our ability to average over longer periods of time.
6. Slave HeNe system: Currently, the beatnote between the polarization-stabilized HeNe and the I_2-stabilized HeNe is used to correct the spectral axis for drift in the HeNe frequency. However, this beatnote signal is only collected once per data point and is an after-the-fact correction. The uncertainty in the Melles Griot HeNe is still the dominant source of uncertainty in the cavity mode position. It is possible to lock a HeNe to the I_2-stabilized HeNe. Thereby, the long term frequency stability of the Melles Griot HeNe will be reduced from 1 MHz (caused largely by thermal fluctuations) to a few tens of kHz.

1.2. System Performance

A significant amount of time was utilized to determine system performance in regards to precision, sensitivity, and resolution. These aspects of the setup will be discussed here.

1.2.1. Sensitivity

As mentioned previously, the minimum detectable absorption level (MDAL) of the setup was determined to be 6×10^{-10} cm^{-1} $Hz^{-1/2}$ by the equation

$$MDAL = \frac{\Delta\tau}{\tau} \times \frac{\tau_{vacuum}}{\sqrt{rate}}, \tag{1.6}$$

where $\frac{\Delta\tau}{\tau}$ is the uncertainty of the ring-down decay time, 0.07%, τ_{vacuum} is the empty cavity life time of 11.9 μs, and the acquisition rate is 200 Hz. Effectively, $\frac{\Delta\tau}{\tau}$ is

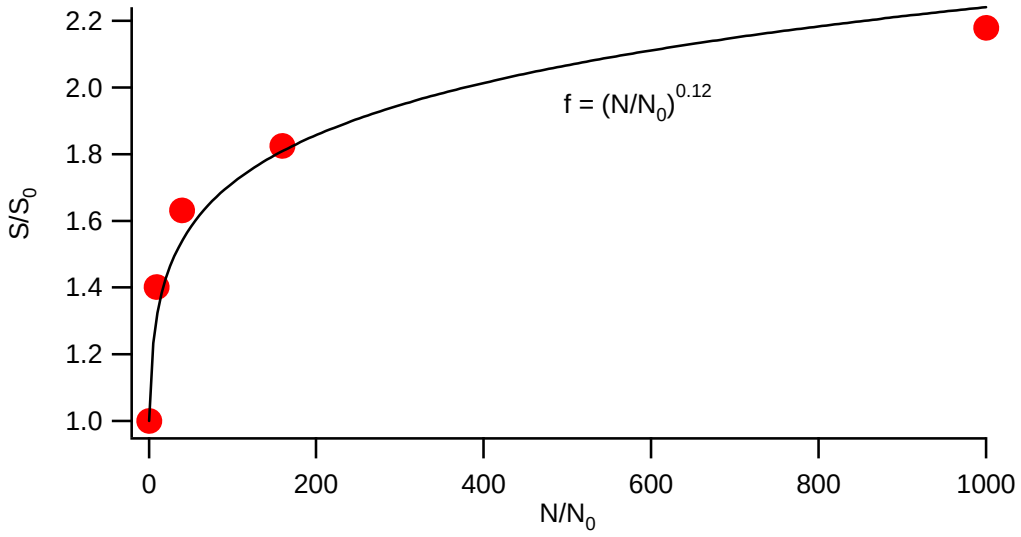

Figure 1.7. Signal to noise versus number averaged for the ^{P}P(23) transition. Clearly shows the noise does not scale as the $\sqrt{N}$. $N_0 = 10$ averages, S_0 is the S/N = 1000 at N_0.

inversely proportional to the peak signal-to-noise in the ring-down decay. In these experiments the typical noise level is 5 mV_{pp}, nearly entirely due to detector noise. By using a lower noise detector and/or increasing the signal level (i.e. more electronic gain or a stronger laser) it should be straightforward to significantly improve the sensitivity. However, there are no commercial detectors that have less noise while maintaining the necessary gain and bandwidth for ring-down experiments.

Another means of improving sensitivity is by increasing the acquisition rate and averaging. However, the setup quickly reaches the point when additional averaging does not improve the signal-to-noise ratio with the usual $\sqrt{N}$ dependence. As can be seen in Figure 1.7, there is only marginal improvement in S/N with increased averaging time. The Allan variance and autocorrelation (Fig. 1.8) of 100,000 ring-down events collected in a 5 minute span show that the practical averaging limit is reached with as few as 30-50 decays. Although optical fringing could

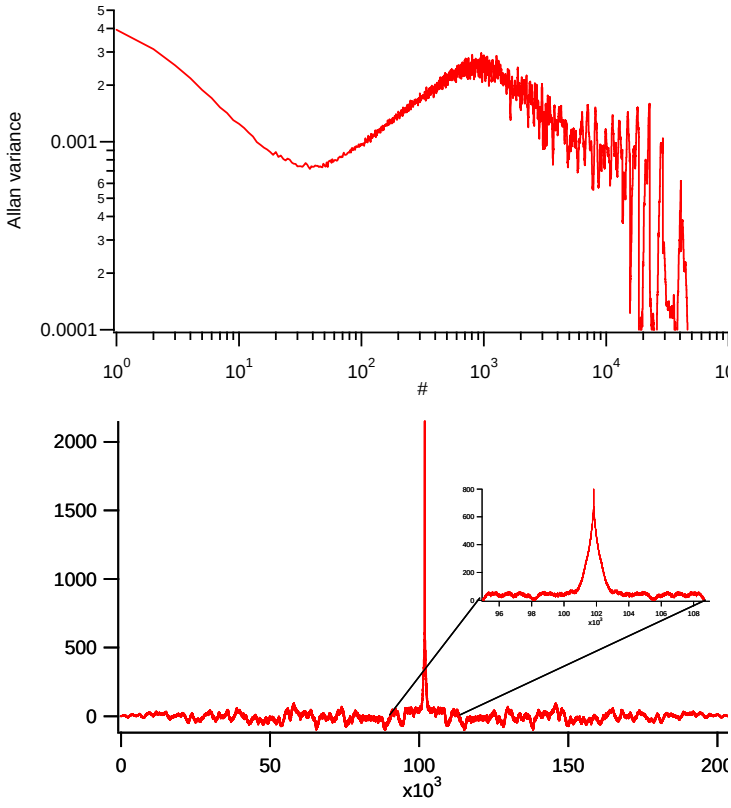

Figure 1.8. Allan variance and autocorrelation for 100,000 ring-down decays at a constant laser frequency.

have influenced the results in Fig. 1.8 which were performed by scanning over the ^{P}P(23) O_2 *A*-band transition, the Allan variance and autocorrelation were performed at a constant wavelength in vacuum. Thus, it is unlikely that ètalons are the cause of this system limitation. In an attempt to isolate the cause of this effect, a square wave generator was connected to the computer via an RC circuit with a time constant of 12 μs (to represent the empty cavity ring-down time), and the time constant was measured using the data acquisition software. The Allan variance did not show correlation until 5000 decays, a 100 fold difference from the ring-down cavity, suggesting the cause is not in the data acquisition or computer algorithms. Furthermore, this averaging effect has been observed by us using different lasers (and wavelength regimes), different detectors, and different reflectivity mirrors. The only constant between all of these experiments has been the optical cavity.

The most obvious explanations for correlation in the ring-down decays are variations in the length of the optical cavity and mode competition. However, given that the optical cavity is locked to the stabilized HeNe, variation in the cavity length is unlikely. The standard fluctuations in the HeNe as measured against an I_2-stabilized HeNe are well within 1 MHz. The fractional change in the cavity length (and thus the ring-down time) will be directly proportional to the fractional change in the HeNe laser, or 1 MHz/474 THz = 2×10^{-9}. This is nearly 6 orders of magnitude below the standard noise in the ring-down time (~0.05%) and, therefore, cannot be the cause.

Table 1.1

$^{\Delta N}\Delta J(N'')$	position, cm^{-1}	# studied	S/N	Line intensity	Air-broadening	Line Position, kHz
$^{P}P(27)$	13010.81266	7	470	0.24%, 0.13%	9%, 6%	433, 257
$^{P}P(25)$	13021.29125	13	800	0.096%, 0.081%	4%, 4%	215, 137
$^{P}P(23)$	13031.39453	7	1400	0.073% ,0.054%	3%, 2%	107, 85

Uncertainties for Galatry lineshape parameters. X, Y. X is the uncertainty of the fit value between scans and Y is the average of the individual fit uncertainties.

Simulations of ring-down decays with varying amounts of bi-exponential behavior (ringing of two cavity modes simultaneously) were performed. If the competing mode is always there, then there are no correlation effects in the Allan variance plot. If the competing mode is only periodically present, a similar Allan variance plot is generated. Furthermore, the competing mode need only have 0.5% the intensity of the TEM_{00} mode is therefore it is indistinguishable in the residuals of the ring-down fit. Due to the "soft" locking mechanism used to lock the probe laser to the cavity, the competing mode theory is entirely plausible. Under the assumption that mode competition is the culprit, there are two readily available solutions. First, better mode-matching of the laser to the cavity will result in less intensity in the higher-order modes. Second, the spacing of the higher order modes is directly related to the nominal length of the cavity. At 74 cm, the nearest mode is 2 MHz away from the TEM_{00} mode and is the $m+n = 12$ mode. However, changing the length to 73.2 cm will increase the distance of the nearest mode to 7 MHz.

1.2.2. Precision

It is preferential to assume that the precision of a lineshape parameter is well approximated by the uncertainty in the fit to the transition, thereby eliminating the need to perform numerous reproducibility experiments for each transition studied. To confirm that fit uncertainties are a reasonable estimate of the measurement precision, the ^{P}P(23), ^{P}P(25), and ^{P}P(27) transitions were measured repeatedly (7 scans for ^{P}P(23) and ^{P}P(27), 13 for ^{P}P(25)) using the same fill (10 Torr air). The results are shown in Table 1.1, where the first number is the uncertainty between scans, and the second number is the average fit uncertainty. As can be seen, the fit uncertainties are a reasonable approximation (within a factor of 2) for all parameters used in a Galatry lineshape fit. In addition, the precision tracks well with increased S/N as anticipated. Although this shows the quality of the reproducibility, the true uncertainty will be higher due to such things as systematic errors, uncertainties in mole fraction (0.2%), number density (<0.1%), and temperature and quality of the lineshape function (0.1–0.3%) used to fit experimental data. One parameter that is difficult to quantize is the thermal gradient between the thermistor on the outside of the cell and the true temperature within the cell. Because of the large lower-state energies, the change in line intensity with temperature is ~1%/K. Therefore, even a slight gradient can cause a significant error in the line intensity. For most experiments the temperature is stable to 0.1 K during the course of the scan. Assuming an uncertainty of 0.1 K translates into a line intensity uncertainty of 0.1%, equivalent to the fit uncertainty for many of the transitions.

1.2.3. Resolution and the Frequency Axis

The FS-CRDS approach provides an extremely precise, accurate, and linear *relative* frequency detuning axis without the need for calibration in terms of external étalons or reference gases. The uncertainties associated with the frequency axis are discussed in detail in Chapters 2 and 3. Typical uncertainties in line positions are generally less than 1 MHz when measured against well-determined absolute calibration standards (e.g. hyperfine components of ^{39}K).

1.3. Conclusions

The FS-CRDS technique is a very precise and sensitive method for recording high-resolution spectra. We have studied the performance of the instrument in both the frequency and amplitude axes. Uncertainties of various parts of the instrument have been measured and/or estimated and presented.

References

[1] J.T. Hodges, R. Ciurylo, Rev. Sci. Instrum. 76 (2005) 023112.

[2] J.T. Hodges, H.P. Layer, W.W. Miller, G.E. Scace, Rev. Sci. Instrum. 75 (2004) 849-863.

[3] J.T. Hodges, D. Lisak, Appl. Phys. B 85 (2006) 375-382.

[4] D. Lisak, J.T. Hodges, R. Ciurylo, Phys. Rev. A 73 (2006) 012507.

[5] J.T. Hodges, J.P. Looney, R.D. van Zee, Appl. Opt. 35 (1996) 4112-4116.

[6] P. Zalicki, R.N. Zare, J. Chem. Phys. 102 (1995) 2708-2717.

[7] A.K. Mollner. Cavity Ring-down Spectroscopy Studies of Atmospheric Reactions: Peroxynitrous Acid Formation and Alkoxy Radical Isomerization. California Institute of Technology, Pasadena, 2007.

[8] A. Yariv, *Optical Electronics in Modern Communications: 5th Edition*. Oxford University Press: 1997.

[9] D. Halmer, G. von Basum, P. Hering, M. Murtz, Rev. Sci. Instrum. 75 (2004) 2187-2191.

[10] R.W.P. Drever, J.L. Hall, F.V. Kowalski, J. Hough, G.M. Ford, A.J. Munley, H. Ward, Applied Physics B-Photophysics and Laser Chemistry 31 (1983) 97-105.

[11] E.D. Black, American Journal of Physics 69 (2001) 79-87.

CHAPTER 2

High-Precision Pressure Shifting Measurement Technique using Frequency-Stabilized Cavity Ring-Down Spectroscopy

This chapter was published as:

D.J. Robichaud, J.T. Hodges, D. Lisak, C.E. Miller, M. Okumura,, "High-Precision Pressure Shifting Measurement Technique using Frequency-Stabilized Cavity Ring-Down Spectroscopy," J. Quant. Spectrosc. Rad. Trans. (2007) doi:10.1016/j.physletb.2003.10.071

2.1 Abstract

We describe a high-precision method for measuring pressure shifting of absorption lines. The technique involves the acquisition of high-resolution spectra using a cavity ring-down spectrometer whose length is continuously locked to a frequency-stabilized reference laser over a range of sample pressures. We discuss a relatively large correction arising from the pressure-dependence of dispersion in the cavity modes, and we demonstrate pressure shifting measurements in air for transitions in the O2 A band. Pressure shifts in the range −0.011 cm^{-1} atm^{-1} to −0.007 cm^{-1} atm^{-1} are reported. We measured relative positions of line centers to within 70 kHz and determined pressure shifting coefficients over a 5 kPa pressure range with relative uncertainties approximately equal to 1.0 %, which constitutes a five-fold improvement over previous measurements.

2.2. Introduction

Pressure shifting is relevant to high-resolution spectroscopic methods that rely on the prediction and/or measurement of individual transition wave numbers and line shapes. For example, the pressure shift of a line must be known in order to predict asymmetrical line shapes that arise from speed-dependent perturber-absorber interactions [1–3]. The line shift effect is quantified by the pressure-shifting coefficient $\delta = d\tilde{\nu}/dp$, which in general will depend upon the collision partners and temperature. In spectroscopic atmospheric retrievals of gas concentration, line positions need to be known within 10^{-4} cm^{-1}. Regardless of the gas pressure, uncertainty in line position will affect line shape simulation and, thus, bias the retrieval. A current and important example of the need for high-accuracy δ values is the near-ir measurements of atmospheric CO_2 and O_2 with NASA's Orbiting Carbon Observatory (OCO), where pressure shift uncertainties < 0.0002 cm^{-1} atm^{-1} are required [4].

For gas-phase atmospheric spectra, air-broadening yields δ ranging in magnitude from ≈ 0.001 cm^{-1} atm^{-1} to 0.1 cm^{-1} atm^{-1} [5]. The shifts are often significantly smaller than transition Doppler widths over the pressure range relevant to atmospheric spectra. Although δ can be measured with high-resolution Fourier-transform spectrometers (FTS) calibrated by reference spectra as well as laser spectrometers with frequency axes calibrated in terms of étalons and/or wavelength meters, uncertainty in δ is often unacceptably high, especially for relatively weak transitions.

Here we present a new high-precision method for measuring line shifting, which is based upon the frequency-stabilized cavity ring-down spectroscopy (FS-CRDS) technique. We discuss a relatively important correction that must be taken into account in

order to separate an apparent pressure shift (arising from dispersion of the ring-down cavity modes) from the true pressure shift of the spectra. We demonstrate the technique with regard to measurements of $^{16}O_2$ *A*-band *PP*- and *PQ*-branch lines using room-temperature air samples. The remainder of the paper includes a brief discussion of the measurement technique as well as results comparing new and previous measurements.

2.3. Measurement Technique

2.3.1 Frequency-Stabilized Cavity Ring-Down Spectroscopy

FS-CRDS is an approach to CRDS in which the ring-down cavity's comb of resonant frequencies is actively locked with respect to a reference laser, typically a λ = 633 nm frequency-stabilized HeNe laser. This configuration enables the selective and controlled excitation of a specific longitudinal mode order of the TEM_{00} by a second cw probe laser that is frequency-locked to the ring-down cavity. Detailed descriptions of FS-CRDS spectrometers located at the National Institute of Standards and Technology (NIST), Gaithersburg, MD, can be found in Refs. [6, 7]. Each ring-down event is the exponential decay of one cavity mode, occurring at a specific cavity resonance frequency. Spectra are acquired by step scanning the probe laser frequency from one cavity mode to the next and measuring the succession of ring-down decay rates. To fill in spectral gaps between cavity modes, the reference laser is frequency shifted using a double-passed acousto-optic modulator (AOM). The performance of the FS-CRDS frequency detuning axis is limited by uncertainty in the cavity free spectral range (FSR) and the linewidth of the stabilized ring-down cavity [8], not by laser line width and drift, external étalons, wavelength meters or reference spectra. In a recent FS-CRDS study a frequency

resolution better than 50 kHz was demonstrated by observation of MHz-wide Doppler-free saturation dips in H_2O spectra [9].

In the present study, the ring-down cavity mirror reflectivities were 0.95 and 0.9998 for the reference laser and probe laser wavelengths, respectively, and the cavity length and internal volume were nominally 74 cm and 0.2 L. All measurements were made on static synthetic air samples at room temperature, and the outer wall temperature of the ring-down cell was measured to within 0.1 °C with a NIST-calibrated 2.4 kΩ thermistor. The NIST-certified synthetic air mixture composition (expressed as molar fractions) was 79.28 % N_2, 20.720(43) % O_2, 0.0029 % Ar, 0.00015 % H_2O, and 0.001 % unidentified residual species. The gas pressure was measured with two NIST-calibrated capacitance diaphragm gauges having full scale responses of 13.3 kPa and a 133 kPa, respectively. The cavity FSR = 201.987(30) MHz was measured using the technique given in Ref. [8]. The probe laser was a commercial cw external cavity diode laser (ECDL) tunable over the wavelength range 761 nm to 781 nm, emitting a single mode with approximately 7 mW of power and with a fine frequency mode-hop-free tuning range greater than 70 GHz. A commercial wavelength meter with a standard uncertainty of 60 MHz was used to locate specific lines in the O2 A-band under consideration. Ring-down decay signals were measured with an 8-MHz-bandwidth Si-PIN photoreceiver, digitized at 25 Msamples s^{-1} with a 12-bit digitizer, and fit in real time using the fast algorithm of Halmer et al. [10]. The noise-equivalent-absorption coefficient of the spectrometer was approximately 2×10^{-10} cm^{-1} $Hz^{-1/2}$.

2.3.2 Ring-Down Cavity Frequency Comb

The measurement of pressure shifting in ring-down spectra requires a quantitative

understanding of the pressure-dependence of the ring-down cavity's resonant frequencies. To account for the fact that the reference and probe laser wavelengths are widely separated, we treat the frequency comb of the ring-down cavity as a pair of combs labeled by mode orders j and q. The TEM_{00} resonant frequencies of the cavity near the reference laser wavelength are

$$\nu_j = \frac{c}{2n_j(l+\Delta l_j)}(j+\theta_G+\theta_j) \tag{2.1}$$

with an identical expression labeled by q for the resonances near the probe laser wavelengths. The quantities c, n_j, and l are the speed of light, the real part of the refractive index of the cavity medium at the reference laser wavelength, and the geometrical cavity length, respectively. θ_G is the wavelength-independent Guoy phase shift, which can be treated as a constant for small displacements of the cavity mirror. $\Delta l_j << l$ accounts for slight penetration of the cavity mode into the dielectric stack comprising the mirror coatings [11], an effect also influencing the phase shift θ_j at the coatings. To a high-degree of approximation, FSR is independent of wavelength and given by $c/(2n_q l)$.

2.3.3 Pressure-Dependence of FS-CRDS Frequency Axis

At fixed gas pressure, the FS-CRDS frequency axis $\Delta\nu_q$ relative to the first point in the spectrum is given by

$$\Delta\nu_q = \frac{c}{2n_q l}\Delta q - 2\Delta f_A \frac{\nu_q}{\nu_j}, \tag{2.2}$$

where $\Delta f_A = f_A - f_{A,0}$ is the change in AOM frequency f_A, and $f_{A,0}$ is the AOM frequency at $\Delta\nu_q = \Delta q = 0$. Accuracy in the detuning axis therefore comes directly from knowledge of

the cavity FSR. In this experiment the relative standard uncertainty in the FSR was estimated to be less than 0.015 % [8].

To measure δ, ring-down spectra are acquired over a range of pressures, and line centers are determined from least-squares fits of model line shapes to the data. In order to determine the frequency shift of a line in terms of the above parameters, the cavity must remain locked to the same mode order j at the reference laser wavelength (or shifted by a known number of mode orders). However, increases in gas pressure augment the optical pathlength $n_j l$ of the cavity. In this experiment, as the gas sample pressure is increased, the cavity length stabilization servo maintains resonance with the reference laser frequency by displacing one ring-down cavity mirror, thus compensating for the change in optical pathlength. The pressure range over which the cavity lock can be maintained is approximately 5 kPa, limited by the 10-μm range of motion of the pzt-actuated ring-down cavity mirror.

At fixed j and letting $d\nu_j$ =0, Eq. 2.1 can be differentiated to give

$$dl = -l\frac{dn_j}{n_j} = -ld\ln(n_j), \tag{2.3}$$

where we have neglected changes in θ_j, and Δl_j that might be caused by changes the gas refractive index. A similar analysis at the probe laser condition, this time substituting the previous equation and solving for $d\nu_q$, gives

$$d\nu_q = \nu_q[d\ln(n_j) - d\ln(n_q)]. \tag{2.4}$$

Assuming that the length-stabilization servo maintains cavity lock with respect to the reference laser, then differential changes in the wavelength-dependent refractive index (driven by changes in the gas pressure) will shift ν_q. Consequently, the resonant

frequencies of the locked ring-down cavity comb in the vicinity of the probe laser frequency are pressure-dependent, an effect that must be taken into account when comparing spectra taken at different gas pressures. The frequency shift can be accurately predicted using the following correlations for the refractive index of dry standard air. Here the composition by molar percentage of standard air corresponds to 78.09 % N_2, 20.95 % O_2, 0.93 % Ar, and 0.03 % CO_2 [12]. Ciddor [13] expresses the refractivity n − 1 of standard air in terms of wave number $\tilde{\nu}$, gas pressure p, and temperature T. Ignoring the correction terms for H_2O content, these results can be recast in terms of ν as

$$n(\nu, p, T) - 1 = (n_s(\nu) - 1) \times f(p, T)\,, \tag{2.5}$$

where $n_s(\nu) - 1 = 10^{-8}[(k_1/[k_0-(\nu/c)^2])+(k_3/[k_2-(\nu/c)^2])]\times[1+k_c(x_c-x_c,0)]$ is the purely dispersive component of n, evaluated at a reference temperature of 15 °C. This dispersive term is corrected for variations in CO_2 molar fraction x_c by the linear term in brackets in which $x_c,0$ is a reference CO_2 molar fraction equal to 4.5×10^{-4}. In Eq. 2.5, $f(p,T) = (p/p_s)(T_s/T)(Z_s/Z)$ accounts for the density dependence of n, in which the subscript s indicates evaluation at the reference condition (T_s,p_s)=(288.15 K, 101.325 kPa). The compressibility factor for standard air is given by

$$Z(p,T) = 1 - (p/T)(a_0 + a_1 t + a_2 t^2) + (p/T)^2 d\,, \tag{2.6}$$

with $t = T - 273.15$ K. Using the constants (k_0, k_1, k_2, k_3, k_c) and (a_0, a_1, a_2, d), given in Table 2.1, the uncertainties of these equations are estimated to be $< 5\times10^{-8}$ over the range λ = 300 nm to 1690 nm [13]. Substituting Eq. 2.6 into $f(p,T)$ and differentiating with respect to p at fixed T gives

$$df/dp = \frac{T_s Z_s}{p_s T} \times \frac{1}{1-(p/T)a(t)+(p/T)^2 d} \times \left(1 + \frac{p(\frac{a(t)}{T} - \frac{2pd}{T^2})}{1-(p/T)a(t)+(p/T)^2 d}\right), \tag{2.7}$$

where $a(t)=(a_0 + a_1 t + a_2 t^2)$. By differentiating Eq. 2.5 with respect to p and substituting

Table 2.1: Constants for refractive index correlation and compressibility factor for standard air.

k_0 (μm^{-2})	k_1 (μm^{-2})	k_2 (μm^{-2})	k_3 (μm^{-2})	k_c	a_0 ($K\ Pa^{-1}$)	a_1 (Pa^{-1})	a_2 ($K^{-1}\ Pa^{-1}$)	d ($K^2\ Pa^{-2}$)
238.0185	5792105	57.362	167917	0.534×10^{-6}	1.58123×10^{-6}	-2.9331×10^{-8}	1.1043×10^{-10}	1.83×10^{-11}

values from Ciddor [13]

into Eq. 2.4 we obtain

$$d\nu_q / dp = \nu_q [n_s(\nu_j) - n_s(\nu_q)] df / dp \tag{2.8}$$

in which we have assumed $(n_j, n_q) - 1 << 1$. We use Eqs. (2.7) and (2.8) to put a series of spectra, which have been acquired at different pressures but fixed cavity lock, on a common frequency axis by adding the pressure-dependent shift

$$\delta\nu_q = \nu_q [n_s(\nu_j) - n_s(\nu_q)] \tfrac{T_s Z_s}{p_s T}, \tag{2.9}$$

where Δp is the change in gas pressure of a given spectrum with respect to an arbitrary reference pressure and where we have neglected the bracketed pressure-dependent terms on the right-hand-side of Eq. 2.7. At T = 296 K, and for p < 101.325 kPa (1 atm), numerical analysis shows that $1 - Z < 3.5\times10^{-4}$ from which we conclude that the pressure-dependent terms contribute to relative changes in df/dp less than 7×10^{-4}. This means that the mode shift per unit change in pressure is essentially independent of p for the present experimental conditions.

Note that at T =296 K and $\lambda(\nu_j)$= 633 nm, df/dp= 9.61×10^{-3} kPa^{-1} and $[n_s(\nu_j) - n_s(\nu_q)]$= 1.25064×10^{-6} for $\lambda(\nu_q)$= 765 nm. This leads to a pressure-shifting coefficient for the probe comb $d\nu_q/dp$ =4.71 MHz kPa^{-1} (equivalent to the wave number shift $d\tilde{\nu}_q/dp$ =0.0159 $cm^{-1}\ atm^{-1}$), which is about twice the magnitude of the O_2 *A*-band δ values considered here and larger than the anticipated shift coefficient for most atmospheric

species. The temperature dependence of dv_q/dp is weak, showing a fractional change per-unit-temperature of −0.34% K^{-1}. In Fig. 2.1 we show the wavelength dependence of dv_q/dp for CO_2-free dry standard air at T = 296 K. These calculations show that dv_q/dp is negative for λ < 633 nm, increases with λ to a maximum of 6.89 MHz kPa^{-1} at λ = 1100 nm, and then decreases slowly at longer wavelengths. It is important to note that these results are expected to be similar for gases other than air [14] because of similarity in the dispersion function $n_s(\nu)$.

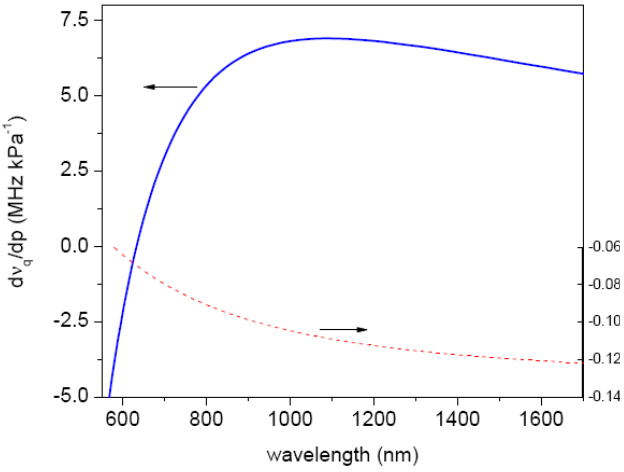

Figure 2.1. The solid line gives the predicted wavelength depedence for the mode shift per unit change in pressure with the ring-down cavity locked to λ = 633 nm for CO_2-free, dry standard air at T = 296 K using the correlations of Ciddor [13]. The dashed line represents the relative difference in the same quantity calculated using the correlations of Birch and Downs [12] and Ciddor for p = 5.4 kPa, T = 296 K, and a CO_2 molar fraction of 0.03 %.

2.3.4 Uncertainty of Refractive Index Correlation

An alternative set of correlations given by Birch and Downs [12] for the refractive index of standard air gives numerical results for $n(\lambda)$ that agree with the Ciddor correlations used here to within 3×10^{-8} [13]. Comparison of the dispersion function for the two cases shows a systematic agreement at the 0.015 % level over the wavelength range 500 nm to 1700 nm. The dashed line in Fig. 2.1 shows the normalized difference between dv_q/dp based on the Birch and Downs correlations and dv_q/dp based on Ciddor, the normalization factor being the latter quantity. At the wavelength region and pressure

range of the present experiment, the two sets of correlations agree to within 0.09 %, with the Birch and Downs calculations systematically low. Given that the dispersion functions are in much better agreement, we primarily ascribe the 0.09 % disparity to differences in $f(p,T)$ for the two models.

The experimental air sample had a composition slightly different than the standard air mixture described above, causing some uncertainty in the determination of dv_q/dp. To estimate the effect of deviations from the standard air mixture, we start with the Lorenz-Lorentz equation which gives the refractive index of mixture of nonpolar gases as

$$\frac{n^2-1}{n^2+2} = \sum_i w_i R_i \quad , \tag{2.10}$$

with w_i and R_i representing the molar fraction and molar refractivity of component i, respectively. To first order we treat the mixture as binary, comprising N_2 and O_2, and having molar fractions that differ from standard air by Δw_{N2} and Δw_{O2}. Differentiation of Eq. 2.10 and some manipulation give

$$\Delta(n-1) = (n_{N_2}-1)\frac{pT_0}{p_0T}(\Delta w_{N_2} + \frac{R_{O_2}}{R_{N_2}}\Delta w_{O_2}) \, , \tag{2.11}$$

where $n_{N2} - 1$ is the refractivity of N_2. Note that Eq. 2.10 can be used to calculate R_{O2} and R_{N2} from the refractivities of N_2 and O_2 reported at the reference condition (p_0, T_0) = (101.325 kPa, 273.15 K). For wavelengths in the visible range, the quantities 10^4 $[n_{N2}(p_0, T_0) - 1]$ and 10^4 $[n_{O2}(p_0, T_0) - 1]$ range from 2.95 to 3.0 and 2.72 to 2.8, respectively, from which we estimate that R_{O2}/R_{N2} ranges from 0.907 to 0.949. From Eq. 2.11 these values yield a change of about 1% in the refractivity of the actual mixture with respect to

the standard CO_2-free dry air mixture. Note, however, that the quantity $d\nu_q/dp$ is driven by dispersion in $n(\lambda)$ associated with the wavelength dependence of the ratio $R_{O2}(\lambda)/R_{N2}(\lambda)$. Using Eq. 2.11 with $\Delta w_{N2} = 1.119\%$ and $\Delta w_{O2} = -0.23\%$ for our synthetic air mixture, we find that $\Delta(n-1)$ changes in magnitude by 0.25% per change in the refractivity ratio R_{O2}/R_{N2}. Assuming $\Delta R_{O2}/R_{N2} < 0.1$ gives a maximum $\Delta(n-1) = 0.025\%$.

Combining the effects of uncertainty in the refractive index correlation due to 1) limitations of the correlations for standard air mixtures and 2) the deviation from a standard air mixture, we assign a relative standard uncertainty in $d\nu_q/dp$ of 0.1 %. As shown below, this systematic uncertainty is at least 9 times lower than the uncertainty in the experimental determination of pressure shifting in the observed spectra.

In order to confirm the foregoing model for pressure-shift of the probe comb frequency, we measured $d\nu_q/dp$ using an optical heterodyne experiment. To this end, a second nominally identical FS-CRDS spectrometer was set up comprising a separate ring-down cell, reference laser, probe laser, etc. Measurements were made near λ=765 nm with air as the sample gas. Each probe laser was fine tuned to nearly the same frequency and locked to its respective ring-down

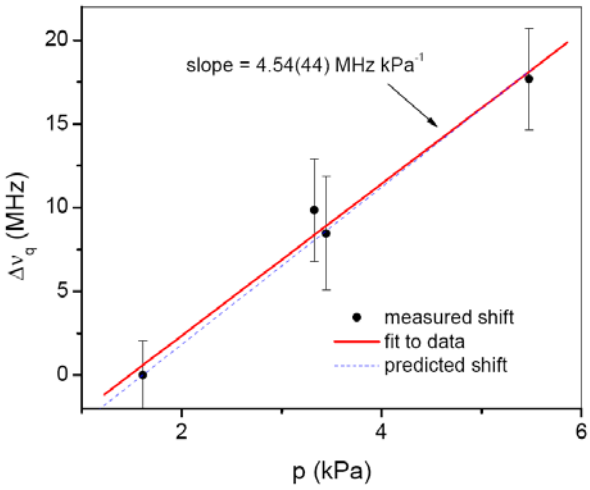

Figure 2.2. Beat-note measurement of probe comb frequency shift at 764.5 nm. Measured values (circles) and linear regression (solid line); prediction based on Eq. 2.9 (dashed line).

cavity, and the two probe laser beams were combined and sampled with a 125-MHz -bandwidth Si-PIN photoreceiver. The beat-note produced by the interference of these two locked lasers was monitored with an RF spectrum analyzer and a frequency counter. The gas pressure in one of the ring-down cavities was varied, while the other cavity was kept under vacuum. The measured (4.54(44) MHz kPa^{-1}) and predicted (4.70 MHz kPa^{-1}) frequency shifts $d\nu_q/dp$ shown in Fig. 2.2 have the same sign and agree to within the uncertainty of the beat note measurement. Although not sufficiently accurate to confirm the foregoing 0.1 % uncertainty estimate, these results give confidence that pressure-shifting of the cavity frequency comb can be properly accounted for using Eq. 2.9.

2.4 Results

Figure 2.3 shows a typical series of spectra for the *P*25 *P*25 transition of $^{16}O_2$, acquired at fixed cavity lock over the pressure range 3.9 kPa to 8.8 kPa. The determination of line centers from experimental spectra depends upon the choice of the line profile that is fit to the data, especially for asymmetric line shapes such as those taking into account speed-dependent effects or line mixing phenomena. For simplicity and since such higher-order line shape analyses were outside the scope of this work, each spectrum was fit to a symmetric Galatry [17] line profile to locate its respective line center. The high precision in both axes of these spectra made it possible to locate the center of the line (relative to an arbitrary starting point) to within ≈70 kHz. The absolute location of line center, however, has a far greater uncertainty and is limited by the 60 MHz standard uncertainty of the wavelength meter. Close inspection of the peaks shown in the inset reveals a small but discernible systematic shift to lower frequencies as

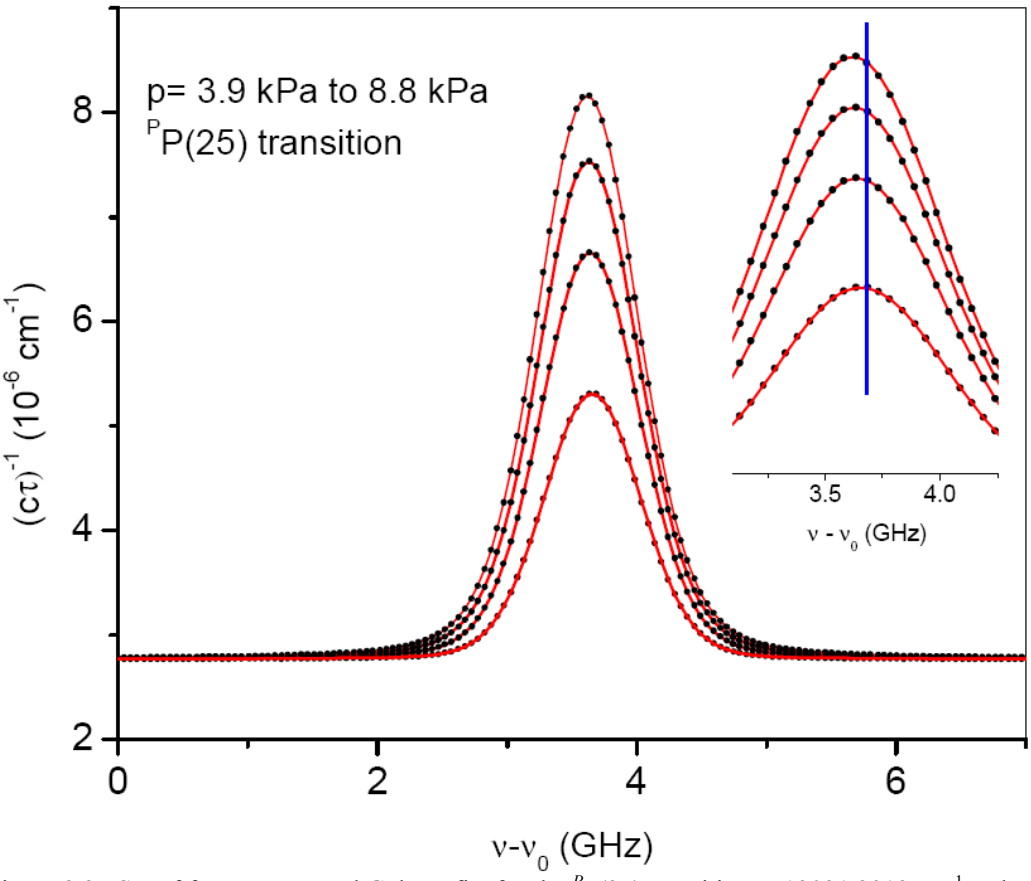

Figure 2.3. Set of four spectra and Galatry fits for the ^{P}P(25) transition at 13021.2913 cm^{-1}. These data were acquired with the ring-down cavity continuously locked to the frequency-stabilized HeNe reference laser; however the frequency axis was not corrected according to Eq 2.9. The quantity τ is the measured ensemble-averaged ring-down time constant at each frequency step. The spectra correspond to the p = 60, 50, 40, and 30 Torr, the peak areas increasing with pressure. The inset shows a zoom of the spectra near line center, and the vertical line is a reference that passes through frequencies corresponding to an identical mode order q. The ratio of peak absorption signal to baseline noise for the highest pressure is ~6500:1.

pressure increases. The majority of this shift, however, is associated with the pressure-dependent mode shifting effect described by Eq. 2.9.

Figure 2.4 shows locked-cavity pressure shift results for three transitions, where the observed peak shift was corrected according to Eq. 2.8. The data were fit by weighted linear regression of the data with the respective slopes assigned to δ for each case. The slope fit uncertainty typically ranged from 0.55 % to 2.2 % and showed a strong correlation with the pressure span Δp over which the measurements were taken. For a fixed Δp, the fractional change in the absorption losses was smaller for the relatively weak high-J lines since these lines were probed at higher pressures than the low-J lines. For example, the spectra of the transitions corresponding to (J' = 32) and (J' = 18) were measured over the pressure ranges (75.6 kPa to 80 kPa) and (0.13 kPa to 1.47 kPa),

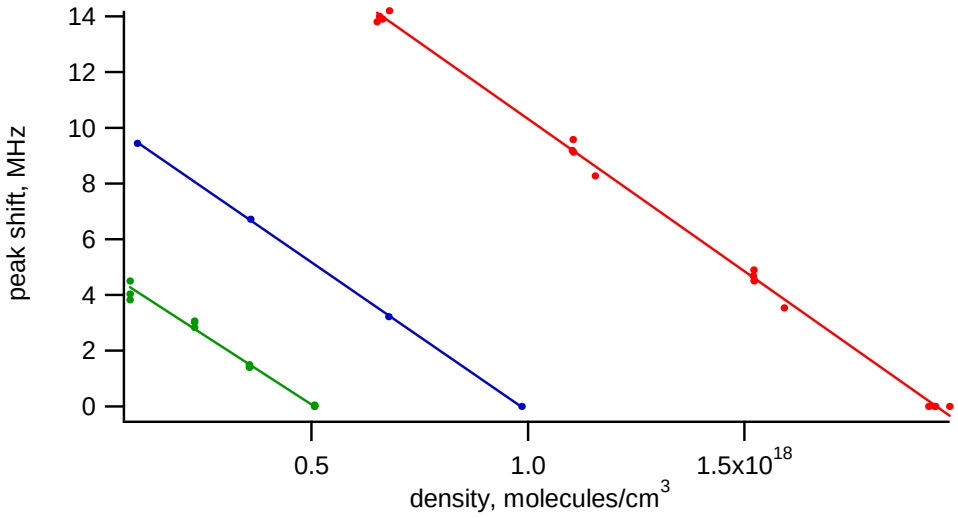

Figure 2.4. Measured peak shifts (symbols) and regressions (solid lines) for the ^{P}P(21), ^{P}P(23), and ^{P}P(25) transitions. The peak shifts for the ^{P}P(21) and ^{P}P(25) transitions were measured on multiple days.

respectively. Consequently, the spectra of the high-J lines had a higher average signal-to-noise-ratio (SNR) than the higher-intensity low-J transitions, thus tending to improve the precision and reproducibility of the measured high-J δ values. The inset of Fig. 2.3 shows the combined relative uncertainty $u_r(\delta)$ and incorporates the slope fit uncertainty and the standard deviation of the measurements. In order to provide a check on these results, line shifts for some transitions were also independently determined using the wavelength meter measurements for starting frequency instead of the correction given by Eq. 2.9. This approach required measurements over pressure ranges approaching 100 kPa because of the relatively low resolution of the wavelength meter. In all cases, the two methods gave agreement within their combined uncertainties. Results of our pressure shifting measurements are presented in Chapters 4 and 5.

2.5 Conclusions

We have shown that the FS-CRDS technique can yield pressure shifting coefficients with relative standard uncertainties $u_r(\delta)$ at the 1.0 % level. We note that Δp = 5 kPa was limited in this study by the finite range of motion of the pzt-actuated mirror used to maintain active lock of the ring-down cavity to the frequency-stabilized reference laser. Since $u_r(\delta)$ scales with the ratio of uncertainty in the measurement of line centers divided by the corresponding Δp, a larger Δp range would tend to reduce $u_r(\delta)$, especially for weak lines probed at high pressure that tend to yield spectra with relatively high SNR. In practice, measurements could be made over a substantially greater Δp before encountering complications arising from excessive line broadening. It is expected that $u_r(\delta)$ could be reduced at least two-fold to < 0.5% by increasing the pressure range over

which the FS-CRDS apparatus maintains a continuous lock with the reference laser. From a practical standpoint this modification seems feasible and would involve the incorporation of the electro-mechanical components necessary to extend the range of motion of the servoed ring-down cavity mirror. Finally, we mention that by doing spectral surveys at various pressures, the FS-CRDS method can be used to measure differential pressure shifting coefficients $\delta - \delta_{\mathrm{ref}}$. This approach will be accurate provided there is a sufficiently low uncertainty on the cavity FSR [8]. Here, δ_{ref} could be the independently measured pressure-shifting coefficient of an arbitrary transition determined using the technique discussed in this article. Such an approach could simplify FS-CRDS-based realization of high-precision δ values for multiple transitions.

Acknowledgements

The authors would like to thank Dr. Linda R. Brown (Jet Propulsion Laboratory) for useful discussions. This work was supported by the Orbiting Carbon Observatory (OCO) project, a NASA Earth System Science Pathfinder (ESSP) mission. Additional support was provided by the NIST Office of Microelectronics Programs.

References

[1] P.R. Berman, J. Quant. Spectrosc. Radiat. Transfer 12 (1972) 1331-1342.

[2] P.M. Sinclair, J.P. Berger, X. Michaut, R. Saint-Loup, R. Chaux, H. Berger, J. Bonamy, D. Robert, Phys. Rev. A 54 (1996) 402-409.

[3] D. Lisak, G. Rusciano, A. Sasso, 72 (2005) 012503.

[4] C.E. Miller, L.R. Brown, R.A. Toth, D.C. Benner, V.M. Devi, Comp. Rend. Phys. 6 (2005) 876-887.

[5] L.S. Rothman, D. Jacquemart, A. Barbe, D.C. Benner, M. Birk, L.R. Brown, M.R. Carleer, C. Chackerian, K. Chance, L.H. Coudert, V. Dana, V.M. Devi, J.M. Flaud, R.R. Gamache, A. Goldman, J.M. Hartmann, K.W. Jucks, A.G. Maki, J.Y. Mandin, S.T. Massie, J. Orphal, A. Perrin, C.P. Rinsland, M.A.H. Smith, J. Tennyson, R.N. Tolchenov, R.A. Toth, J. Vander Auwera, P. Varanasi, G. Wagner, J. Quant. Spectrosc. Radiat. Transfer 96 (2005) 139-204.

[6] J.T. Hodges, H.P. Layer, W.W. Miller, G.E. Scace, Rev. Sci. Instrum. 75 (2004) 849-863.

[7] J.T. Hodges, R. Ciurylo, Rev. Sci. Instrum. 76 (2005) 023112.

[8] D. Lisak, J.T. Hodges, Appl. Phys. B (2007) doi:10.1007/s00340-007-2691-x.

[9] D. Lisak, J.T. Hodges, R. Ciurylo, Phys. Rev. A 73 (2006) 012507.

[10] D. Halmer, G. von Basum, P. Hering, M. Murtz, Rev. Sci. Instrum. 75 (2004) 2187-2191.

[11] C.J. Hood, H.J. Kimble, J. Ye, Phys. Rev. A 64 (2001) 038804.

[12] K.P. Birch, M.J. Downs, Metrologia 30 (1993) 155-162.

[13] P.E. Ciddor, Appl. Opt. 35 (1996) 1566-1573.

[14] B. Edlen, Metrologia 2 (1966) 71-80.

[15] J.C. Owens, Appl. Opt. 6 (1967) 51-59.

[16] *CRC Handbook of Chemistry and Physics, 63rd edition*. CRC Press Inc.: Boca Raton, FL, 1982.

[17] L. Galatry, Phys. Rev. 122 (1961) 1218-1223.

[18] C. Hill, D.A. Newnham, J.M. Brown, J. Mol. Spectrosc. 219 (2003) 65-69.

[19] L.R. Brown, C. Plymate, J. Mol. Spectrosc. 199 (2000) 166-179.

CHAPTER 3

Comparison of Semi-Classical Lineshape Models on the Oxygen *A*-Band

3.1 Abstract

Measurements of the spectral profiles of five transitions in the *P* branch of the O_2 *A*-band are presented at 296 K. The lineshapes are compared with several semi-classical models, from Voigt to speed-dependent Galatry profile. Line intensities retrieved using the Voigt profile deviate by up to 3% from the “true” value and show a clear pressure dependence.

3.2 **Introduction**

The oxygen *A*-band, $b^1\Sigma_g^+ \leftarrow X^3\Sigma_g^-(0,0)$, is the most prominent near-infrared feature in the Earth's atmosphere. It has been used extensively since the 1960's to determine cloud top heights, cloud optical properties, and aerosol optical thickness [1]. Such studies have been extended to the *A*-band spectra from the GOME [2] and SCIAMACHY [3, 4] satellite instruments. Current retrievals incorporate the Voigt line shape profile with line shape parameters from the HITRAN database [5]. Yet the failure of the Voigt line shape to reproduce O_2 *A*-band absorption features accurately is well established [6-8] and may account for the large disparity in reported band strengths [see Table 1 of Brown and Plymate [7]].

Many semi-empirical line shape profiles have been developed [9], each being valid to a certain degree depending on the underlying physical assumptions. Therefore, any measurement of the line intensity or band strength is likely to be no more accurate than the lineshape model, which is used to fit the recorded spectrum.

In this chapter we continue our study of the O_2 *A*-band by investigating the effects of line shape profiles on retrieved parameters (e.g., line intensities).

3.3 Experimental

All data was used from our previous study of the O_2 *A*-band [10] and described in Chapter 5. The specific lines used are from 12999 – 13033 cm^{-1}, shown in Table 3.1.

Table 3.1. Transition wave numbers of the O_2 *A*-band in cm^{-1}.

Assignment $\Delta N\ N''\ \Delta J\ J''$	J'	Observed (cm^{-1})	Assignment $\Delta N\ N''\ \Delta J\ J''$	Observed (cm^{-1})
P23 P23	22	13031.394095	P23 Q22	13033.199679
P25 P25	24	13021.290837	P25 Q24	13023.078606
P27 P27	26	13010.812345	P27 Q26	13012.582476
P29 P29	28	12999.956863	P29 Q28	13001.709512

3.3.1 Line Shape Models

The semi-classical line shape models used in this study have been described in detail elsewhere [9] and will be discussed briefly here. The simplest model takes only the motion of the absorber into account and assumes free motion based on a Maxwellian distribution of the absorber velocity (Doppler lineshape). The additional assumption that the collisional (Lorentzian) width and collisional shift are independent of the absorber velocity leads to the commonly used Voigt profile (VP).

Dicke [11] has shown that the motion of the absorber may be influenced by collisions, resulting in a more narrow line width than predicted by the classical Doppler width at the same temperature. Two simplified models of velocity-changing collisions are commonly used to describe Dicke-narrowing profiles. The Galatry profile (GP) [12] is based on the soft-collision model and assumes that a single collision cannot effect the velocity of the absorber. This soft-collision model is more applicable to the case of a relatively light perturber. In the hard-collision model it is assumed that the post-collision velocity distribution is Maxwellian and independent on the velocity prior to the collision. This assumption leads to the Nelkin-Ghatak profile (NGP) [13]. Including the

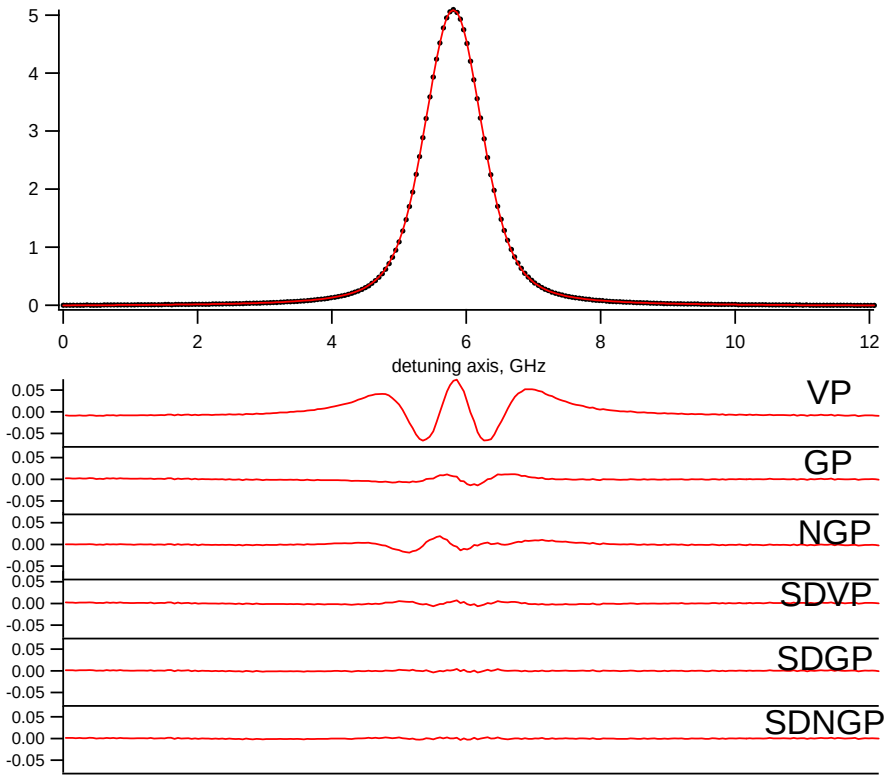

Figure 3.1. Top panel: Recorded spectrum and fit (GP) of the P29 P29 O_2 *A*-band transition at 49.86 Torr and 296.5 K. Residuals for fits using Voigt (VP), Galatry (GP), Nelkin-Ghatak (NGP), Speed-Dependent Voigt, Galatry, and Nelkin-Ghatak (SDVP, SDGP, and SDNGP) profiles are shown. Residuals are shown in order of decreasing χ^2, where SDGP and SDNGP profiles are indistinguishable.

dependence of collisional parameters on absorber velocity, so-called speed-dependent effects, can extend the above profiles to the speed-dependent Voigt (SDVP), speed-dependent Galatry (SDGP), and speed-dependent Nelkin-Ghatak (SDNGP) profiles. Application of these speed dependent profiles requires knowledge of the dependence of the collisional parameters on the absorber velocity, which can be calculated from absorber-perturber interaction potentials. In most cases (and specifically for O_2) exact potentials are not known, but can be approximated by an inverse power form $V(r) = C_q/r^q$. Speed dependent effects may lead to line narrowing and asymmetry near the line center. In addition, to model the speed-dependent asymmetry, one must know the pressure shift of the line.

3.4 Results

The line profile of the *P*29 *P*29 transition at 12999.956863 cm^{-1} is presented in Fig. 3.1 along with residuals of the six lineshape models and is typical of all the transitions used in this study. The Doppler width was constrained to the value corresponding to the measured cell temperature. Pressure-shift was also constrained to the value based on the pressure-shifting coefficients reported previously [14]. All other parameters, Lorentzian width, frequency-, and velocity-changing collisions, and baseline offset and slope were treated as variable fit parameters. As expected, the VP does not reproduce the experimental data well. However, the remaining 5 profiles model the experimental profile quite well, with the SDGP and SDNGP being indistinguishable based on the residuals or χ^2. It is interesting to note that the GP (soft-sphere collisional

model) fits are consistently better by approximately a factor of two than the NGP (hard-sphere model) fits.

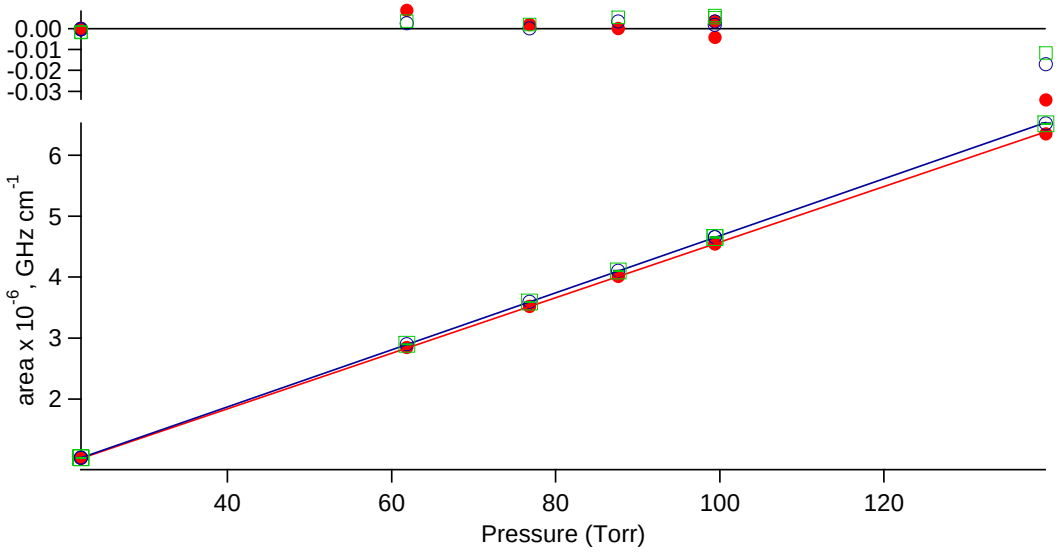

Figure 3.2. Area versus pressure for the P27 P27 transition using VP (red filled in circles), GP (blue open circles), and SDGP (green squares) fits.

Line intensities are clearly the most important line parameter used in spectroscopy. Area vs. pressure plots are shown in Fig. 3.2 for the P27 P27 transition using VP, GP, and SDGP profiles. The intensities retrieved using the VP clearly deviate from the more sophisticated profiles, although all three are effectively linear to within the noise of the measurements. Line intensities relative to the SDNGP intensities are shown in Fig. 3.3 for all of the transitions studied. VP intensities are up to 3% smaller than SDNGP, and the maximum deviation peaks at ~300 Torr, which is the pressure at which the Doppler width ~ Lorentzian width for O_2. This dependence on the deviation with pressure indicates the influence of collisional narrowing. The NGP intensities have deviations approximately an order of magnitude smaller (relative to SDNGP) than the VP

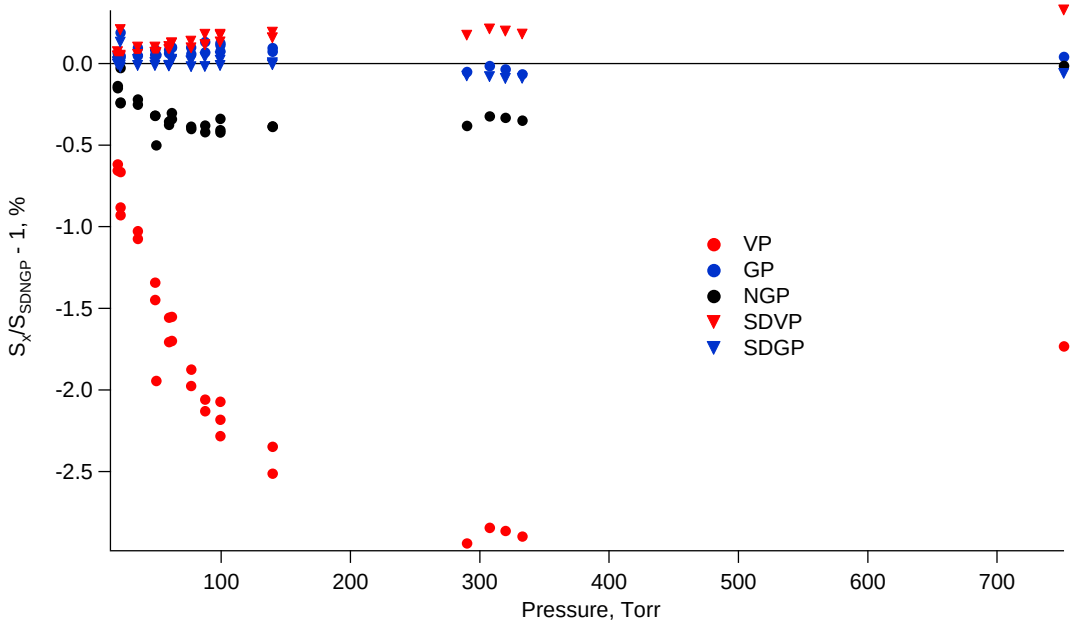

Figure 3.3. Line intensities relative to the SDNGP profile as a function of total pressure at 296 K.

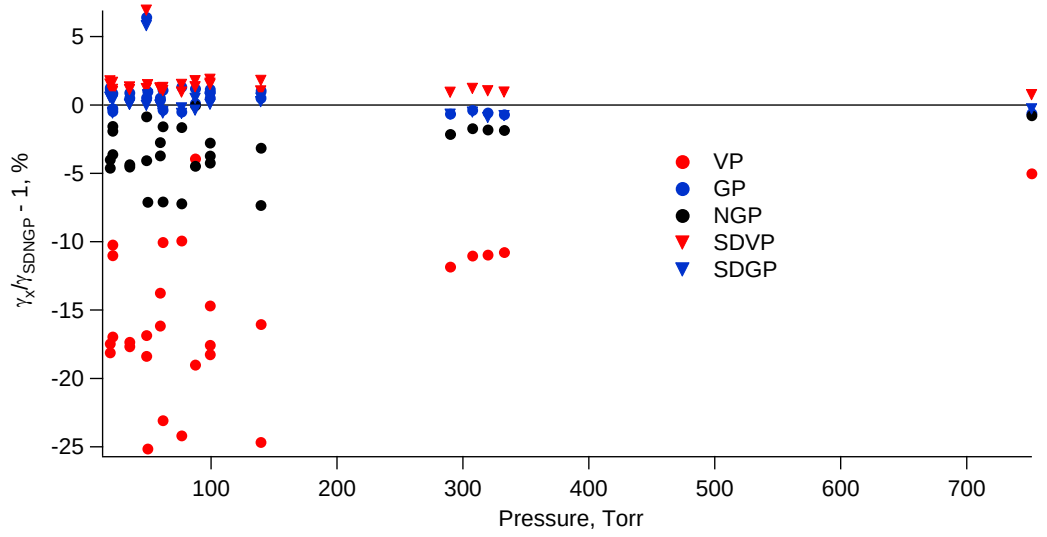

Figure 3.4. Comparison on Lorentz widths.

intensities, but maintain the same pressure dependence. The GP-retrieved intensities are quite good and have deviations no greater than 0.15% from the SDNGP intensities. SDGP and SDNGP have intensities that are nearly identical (<0.05%) and cannot be distinguished within their combined uncertainties.

Pressure-broadened widths are shown in Fig. 3.4 relative to the SDNGP broadened widths. Again, the VP widths deviate the most from the SDNGP values, with ~18% below SDNGP values at low pressures and 5% below at 760 Torr. The other profiles are all within 5% of each other. GP widths are approximately 0.7 % larger than SDNGP widths.

3.5 Conclusions

In this chapter we analyzed the differences between six different semi-classical lineshape profiles from the standard Voigt to speed-dependent soft- and hard-sphere narrowing profiles. It is clear from the data presented that the Voigt profile does not adequately fit the lineshape of transitions in the O_2 *A*-band. Of particular note is intensities retrieved using the VP deviate up to 3% from SDGP and SDNGP intensities and have a strong pressure dependence. Such a deviation could account for some of the discrepancies seen in atmospheric retrievals [5].

Although the SDGP and SDNGP profiles fit the data the best, these methods are probably not the most appropriate for atmospheric retrievals. Both methods are time consuming, particularly the SDGP method, which takes approximately 25 minutes per fit

(SDNGP takes about 5 minutes). Furthermore, the GP profile has intensities that are within 0.15% of the SDGP and SDNGP intensities and takes significantly less computation time. Therefore, we will use the GP profile exclusively for the remainder of this work.

References

[1] D.M. O'Brien, S.A. English, G. DaCosta, J. Atmos. and Ocean. Tech. 14 (1997) 105-119.

[2] K. Chance, J. Quant. Spectrosc. Radiat. Transfer 58 (1997) 375-378.

[3] S. Corradini, M. Cervino, J. Quant. Spectrosc. Radiat. Transfer 97 (2006) 354-380.

[4] B. van Diedenhoven, O.P. Hasekamp, I. Aben, Atmos. Chem. Phys. 5 (2005) 2109-2120.

[5] Z. Yang, P.O. Wennberg, R.P. Cageao, T.J. Pongetti, G.C. Toon, S.P. Sander, J. Quant. Spectrosc. Radiat. Transfer 90 (2005) 309-321.

[6] V.G. Avetisov, P. Kauranen, Appl. Opt. 35 (1996) 4705-4723.

[7] L.R. Brown, C. Plymate, J. Mol. Spectrosc. 199 (2000) 166-179.

[8] K.J. Ritter, T.D. Wilkerson, J. Mol. Spectrosc. 121 (1987) 1-19.

[9] R. Ciurylo, Phys. Rev. A 58 (1998) 1029-1039.

[10] D.J. Robichaud, J.T. Hodges, L.R. Brown, D. Lisak, P. Maslowski, M. Okumura, C.E. Miller, J. Mol. Spectrosc. (2007) submitted.

[11] R.H. Dicke, Physical Reviews 89 (1953) 472-473.

[12] L. Galatry, Phys. Rev. 122 (1961) 1218-1223.

[13] M. Nelkin, A. Ghatak, Phys. Rev. 135 (1964) A4.

[14] D.J. Robichaud, J.T. Hodges, L.Y. Yeung, P. Maslowski, M. Okumura, C.E. Miller, L.R. Brown, J. Mol. Spectrosc. (2007) submitted.

CHAPTER 4

High-Accuracy Transition Frequencies for the O_2 *A*-Band

This chapter was submitted for publication as:

D.J. Robichaud, J.T. Hodges, L.Y. Yeung, P. Maslowski, M. Okumura, C.E. Miller, L.R. Brown, "High-Accuracy Transition Frequencies for the O_2 *A*-Band," J. Mol. Spectrosc. (2007) submitted.

4.1 Abstract

Frequencies for 32 *P*-branch transitions between 12,975 – 13,115 cm^{-1} of the O_2 *A*-band ($b^1\Sigma_g^+ \leftarrow X^3\Sigma_u^-$) were measured using the frequency-stabilized cavity ring-down spectrometer located at NIST, Gaithersburg, MD. Absolute line positions were calibrated using the hyperfine components of ^{39}K D_1 and D_2 atomic transitions yielding uncertainties < 1 MHz ($\cong 3 \times 10^{-5}$ cm^{-1}). Excited $b^1\Sigma_g^+$ state molecular constants were calculated and compared with previously determined values. These new transition frequencies should serve as a convenient secondary calibration standard in the 760 nm region.

4.2 Introduction

The oxygen *A*-band, $b^1\Sigma_g^+ \leftarrow X^3\Sigma_g^-(0,0)$, at 762 nm is the most prominent near-infrared feature in the Earth's atmosphere. It has been used extensively since the 1960's to determine cloud top heights, cloud optical properties, and aerosol optical thickness [1]. Such studies have been extended to the *A*-band spectra from the GOME [2] and SCIAMACHY [3, 4] satellite instruments. There have only been a handful of high-resolution studies to report transition frequencies of the O_2 *A*-band [5-9]. These studies show large systematic biases up to 0.012 cm^{-1} between them, even though the precision for several of these studies are 0.0007 cm^{-1} or better (see Table 8 of Brown and Plymate [5]). The discrepancy in absolute transition frequencies is likely linked to the secondary frequency standards used. The molecular calibration standards used in previous studies of the O_2 *A*-band are either spectrally far removed [5] from the *A*-band or carry large uncertainties [6, 8, 10].

Few standards are available near 700 nm with accuracies better than 0.001 cm^{-1}. Iodine [11, 12] is perhaps the most widely used visible spectroscopic wavelength standard. The I_2-atlas [12] reports lines between 14,250 – 20,000 cm^{-1} with uncertainties of > 0.003 cm^{-1}. Additional studies have extended this range to 12,200 cm^{-1} (e.g. [13]); however, the uncertainties remain > 0.001 cm^{-1}, and the I_2 transitions in this region are quite weak. More recently, argon [14], uranium, and thorium [15] have been studied as potential visible calibration standards with uncertainties of 0.0005 cm^{-1} (Ar) and 0.0002 cm^{-1} (U and Th). However, atomic transitions tend to be widely dispersed throughout the

spectrum, making them less useful unless they are accidentally overlapping with the spectral range being studied.

Recently, Falke et al. [16] recorded the hyperfine components of the ^{39}K *D* lines ($D_1 \cong 12985.185$ cm^{-1} and $D_2 \cong 13042.895$ cm^{-1}) using an optical frequency comb. The precise nature of the frequency comb coupled to a Cs atomic clock enabled them to determine the sub-Doppler hyperfine components with uncertainties < 150 kHz (5×10^{-6} cm^{-1}). In this paper we take advantage of these well-known frequencies to serve as frequency references for our *A*-band spectrum. Furthermore, due to the ubiquitous nature of O_2, the *A*-band is an ideal calibration standard for the visible. If the absolute positions and pressure-induced shifts were to be validated, the O_2 *A*-band would be a convenient secondary calibration standard in this region.

The present study vastly improves our knowledge of the line positions in the O_2 *A*-band at 760 nm. The remainder of this paper comprises discussion of the experimental apparatus and measurement technique, particularly the addition of the ^{39}K absorption reference setup. We report line positions for the $^{16}O_2$ *A*-band transitions from $J' = 2$ to 32 of the *P* branch with combined standard uncertainties of < 1 MHz ($\cong 3 \times 10^{-5}$ cm^{-1}).

4.3 Experimental Apparatus

The frequency-stabilized cavity ring-down spectrometer (FS-CRDS) located at the National Institute of Standards and Technology (NIST), Gaithersburg, MD, has been described in detail previously [17-21]. A unique feature of the FS-CRDS setup is that the

Table 4.1. Experimental Conditions

All scans
Finesse: 15,000
L_{eff}: 3,500 km
Resolution: < 3×10^{-5} cm^{-1}

Oxygen	Potassium
Step size: 50 MHz (1.67×10^{-3} cm^{-1}) Scan range: 8-12 GHz, centered on O_2 spectral line Typical scan time: 10 min Conditions: (pressure, temperature, wave number range) A: 0.502 Torr, 295.2 K, 13,030 – 13,114 cm^{-1} B: 1.015 Torr, 294.4 K, 12,975 – 13,032 cm^{-1} C: 10.055 Torr, 295.2 K, 12,975 – 13,023 cm^{-1}	For each dataset the D_1 and D_2 transitions were measured before and after each scan: 1. 10 MHz/step, 3.2 GHz window centered on transition 2. 0.50 MHz/step, across saturation dips for D_1 3. 0.25 MHz/step, across saturation dips for D_2

mirror-to-mirror distance of the optical cavity is actively stabilized with respect to a frequency-stabilized HeNe laser (0.5 MHz long term uncertainty). This approach, which is used to compensate for variations in the optical pathlength, has the inherent benefit that the spectrum frequency axis is now linked to two precisely measured quantities: the free-spectral-range (FSR) of the ring-down cavity and the frequency shift of the probe laser determined by counting the number of cavity modes from an arbitrary reference point. Spectra are acquired by step scanning the probe laser over sequential mode orders q of the locked ring-down cavity and by tuning the resonance frequencies of the cavity using a variable-frequency acousto-optic modulator (AOM). The AOM shifts the reference laser frequency to which the cavity is actively stabilized and in turn tunes the probe laser frequency by a known amount as given in Eq. (4.1). The underlying premise is that individual resonances of the ring-down cavity can be selectively excited, thus yielding a spectral resolution that is limited by the stability of the cavity modes yet insensitive to variations in the probe laser frequency.

The FS-CRDS approach provides an extremely precise, accurate, and linear *relative* frequency detuning axis without the need for calibration in terms of external étalons or reference gases. Also, in FS-CRDS the excitation of the cavity is inherently single-mode, thus leading to single exponential decay signals. Consequently, FS-CRDS offers significant improvements over traditional cavity ring-down techniques, enabling precise measurements of absorption lineshapes, as well as the measurement of sub-MHz-wide Doppler-free saturation features in low pressure spectra [20, 21].

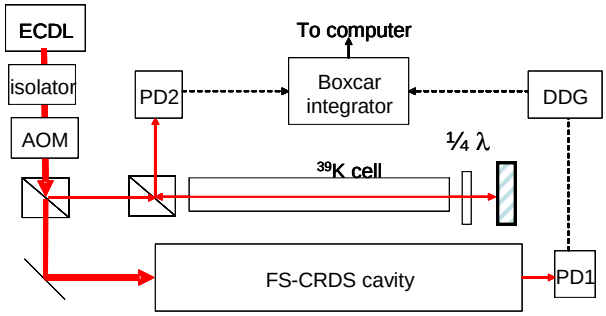

Figure 2.1. Schematics of the experimental setup. ECDL – external cavity diode laser; AOM – acousto-optic modulator; PD – photodetecter; DDG – digital delay generator. See references for a schematic/discussion of the FS-CRDS locking setup.

In the present study we place the FS-CRDS frequency axis on an absolute scale by simultaneous measurement of saturation dips in a reference cell containing ^{39}K vapor. To this end, the ring-down spectra are referenced to the transition frequencies of the hyperfine components of the ^{39}K D_1 ($4s\ ^2S_{1/2} \rightarrow 4p\ ^2P_{1/2}$) and D_2 ($4s\ ^2S_{1/2} \rightarrow 4p\ ^2P_{3/2}$) transitions. When tuned to TEM_{00} resonance of the spectrometer, the absolute frequency of the FS-CRDS probe laser ν_{probe} is

$$\nu_{probe} = \frac{c}{2nl}\Delta q - (2\Delta f_A - \Delta\nu_{HeNe})\frac{\nu_{probe}}{\nu_{HeNe}} + \nu_{ref}\,, \qquad (4.1)$$

where ν_{HeNe} is the stabilized HeNe laser frequency, c is the speed of light, n is the index of refraction of the O_2, l is the effective mirror-to-mirror distance of the ring-down cavity,

and ν_{ref} is the position of the ^{39}K reference transition. In addition, Δq , Δf_A, and $\Delta\nu_{HeNe}$ are the respective changes in longitudinal mode order, AOM frequency and HeNe frequency, and these three changes are with respect to an arbitrary set of reference values for which Eq. (4.1) satisfies the condition $\nu = \nu_{ref}$. The quantity $c/2nl$ is equal to the FSR, which varies with gas density due to the density dependence of n. Therefore, the FSR must be measured for each temperature and pressure condition of the gas sample.

Since the FSR scales the spectrum frequency axis, it is imperative that it be known with low uncertainty, especially for scans spanning a large number of mode orders. To that end the FSR was measured by two methods. We previously reported [22] positions using a commercial wavelength meter to record the probe laser wavelength as a function of Δq. These measurements spanned approximately 15,000 mode orders, which is equivalent to a spectral range of $\cong$100 cm^{-1}. The uncertainty in the wavelength meter reading was $\cong$60 MHz (0.002 cm^{-1}), but the FSR measurement uncertainty was reduced to <200Hz by counting steps in the mode order and measuring the corresponding frequencies over the entire spectral range scanned. However, day-to-day reproducibility of the wavelength meter measurements yielded an effective FSR measurement uncertainty of $\cong$600 Hz. In the present study, we determined the FSR by referencing the cavity modes to the well-known saturation dips in the ^{39}K D_1 and D_2 lines [9]. The determination of these frequencies exhibited no frequency change with daily laboratory variations of temperature or pressure, yielding significantly improved frequency axis determination. Any of the strong transitions in the D_1 line could have been used for this analysis; however, due to the convoluted spectra of the D_2 line we used only the $F'' = 2$

$\rightarrow F' = 3$ transition. Because the ^{39}K D line positions are known to within 150 kHz [16] and spaced by ~55 cm^{-1}, it was straightforward to determine the FSR with low uncertainty (< 80 Hz).

The ring-down cavity mirrors used in this study had nominal transmission losses of 2×10^{-4} (finesse ~ 15,000) centered at 13,050 cm^{-1}, and the cavity length was nominally 74 cm. This corresponds to a theoretical effective pathlength of ~3.5 km. The system noise-equivalent absorption coefficient was approximately 6×10^{-10} cm^{-1} Hz$^{-1/2}$. Ring-down decays, having typical decay times of 4–12 μs, were measured using an 8 MHz Si-PIN photodetector and fit using the algorithm of Halmer et al. [23] All recorded O_2 transitions were fit using a Galatry [24] lineshape, which is based on the soft-collision model and generalizes the Voigt profile for Dicke narrowing effects.

Before entering the optical cavity, ~10% of the probe beam was diverted and used for saturation spectroscopy of the D_1 and D_2 lines of ^{39}K. The reference cell was an all-glass absorption cell, ~46 cm in length that had Brewster's angled windows to reduce étaloning effects. Preparation of the potassium cell included drying at 500 deg C and evacuation to a base pressure < 0.1 μPa. Elemental potassium (99.5 % purity, natural isotopic abundance) was evaporated into the evacuated cell, and the cell was permanently sealed. The potassium cell temperature ranged from 295-298 K and no effort was used to stabilize or control this temperature during the experiments. The 296 K vapor pressure of potassium is ~1.5 μPa and changes by ~12% K^{-1} [25]. The ^{39}K absorption measurement was arranged in a typical double-pass saturation dip configuration, as shown in Fig. 4.1.

Table 4.2. Transition Frequencies of the ^{39}K D_1 and D_2 Lines

D_1			D_2		
F''	F'	ν, MHz	F''	F'	ν, MHz
2	1	850.838 (62)	2	1	980.821 (138)
2	(1,2)	878.612 (88)	2	(1,2)	985.521 (195)
2	2	906.386 (62)	2	2	990.221 (138)
(1,2)	1	1081.706 (88)	2	(1,3)	996.054 (180)
(1,2)	(1,2)	1109.481 (124)	2	(2,3)	1000.754 (180)
(1,2)	2	1137.255 (88)	2	3	1011.286 (116)
1	1	1312.574 (62)	(1,2)	1	1211.690 (195)
1	(1,2)	1340.349 (88)	(1,2)	(1,2)	1216.390 (275)
1	2	1368.124 (62)	(1,2)	2	1221.090 (195)
			(1,2)	(0,2)	1214.737 (275)
			(1,2)	(0,1)	1210.037 (275)
			(1,2)	(1,3)	1226.923 (275)
			(1,2)	(2,3)	1231.623 (275)
			1	0	1439.251 (138)
			1	(0,1)	1440.905 (195)
			1	1	1442.558 (138)
			1	(0,2)	1445.605 (195)
			1	(1,2)	1447.258 (195)
			1	2	1451.958 (138)

An offset of 389 285 GHz and 391 015 GHz was subtracted from the D_1 and D_2 frequencies, respectively. Values in parentheses are 1σ uncertainty in the last digit. Transition frequencies for D_1 are from Falke et al. [16], and crossover peaks are the average of the associated resonant transitions. Transition frequencies for D_2 are calculated based on the Hamiltonian from Buck and Rabi [26] and the hyperfine constants from Falke et al. [16] of A = 6.093 (25) MHz and B = 2.786 (71) MHz.

The laser intensity was 400 μW cm^{-2} and the transmitted beam was measured with a DC-coupled Si-detector having a bandwidth of 200 kHz. To improve the spectral resolution of the technique we incorporated gated detection of the ^{39}K absorption signal. As the probe laser frequency became resonant with an optical cavity mode, bursts (i.e. ring-down events) would appear on the ring-down detector. These bursts were amplified and sent to three digital delay generators (DDG). The first and second DDG were used to lock the probe laser to the TEM$_{00}$ mode of the optical cavity and to trigger the probe laser acousto-optic modulator (AOM) to effectively shut off the light and generate single-

exponential decays as described previously for implementation of the FS-CRDS technique [17, 18]. In the present experiment we added the third DDG and a gated boxcar integrator in order to synchronize the ^{39}K absorption measurement with respect to the FS-CRDS ring-down decays. To this end, the third DDG triggered the boxcar integrator with a 3 μs gate. A total of 1000 shots (~3 seconds) were averaged per spectral point. Since this signal was acquired within 3 μs of the laser frequency's coincidence with the TEM_{00} mode (and its subsequent passive decay) of the frequency-stabilized ring-down cavity, then the effective laser linewidth for the ^{39}K absorption spectrum was insensitive to slow excursions in the laser frequency. This technique yielded an effective laser linewidth of ~300 kHz for the ^{39}K absorption measurements and enabled us to resolve hyperfine structure in the ^{39}K spectra.

All measurements were made at room temperature on static samples of pure O_2. The temperature was measured using a NIST-calibrated 2.4 kΩ thermistor in thermal contact with the outer wall of the cell. Temperatures range from 294-296 K, and no effort was used to stabilize or control the temperature of the cell. Gas pressure was measured with a NIST-calibrated capacitance diaphragm gauge having a full scale response of 13.3 kPa (100 Torr) and standard uncertainty < 1.3 Pa. The ^{39}K *D* lines were recorded during the O_2 scan at the step size of the scan (typically 50 MHz) and immediately after the scan at finer intervals (0.25 - 0.5 MHz/step) for improved precision in locating the saturation dip positions.

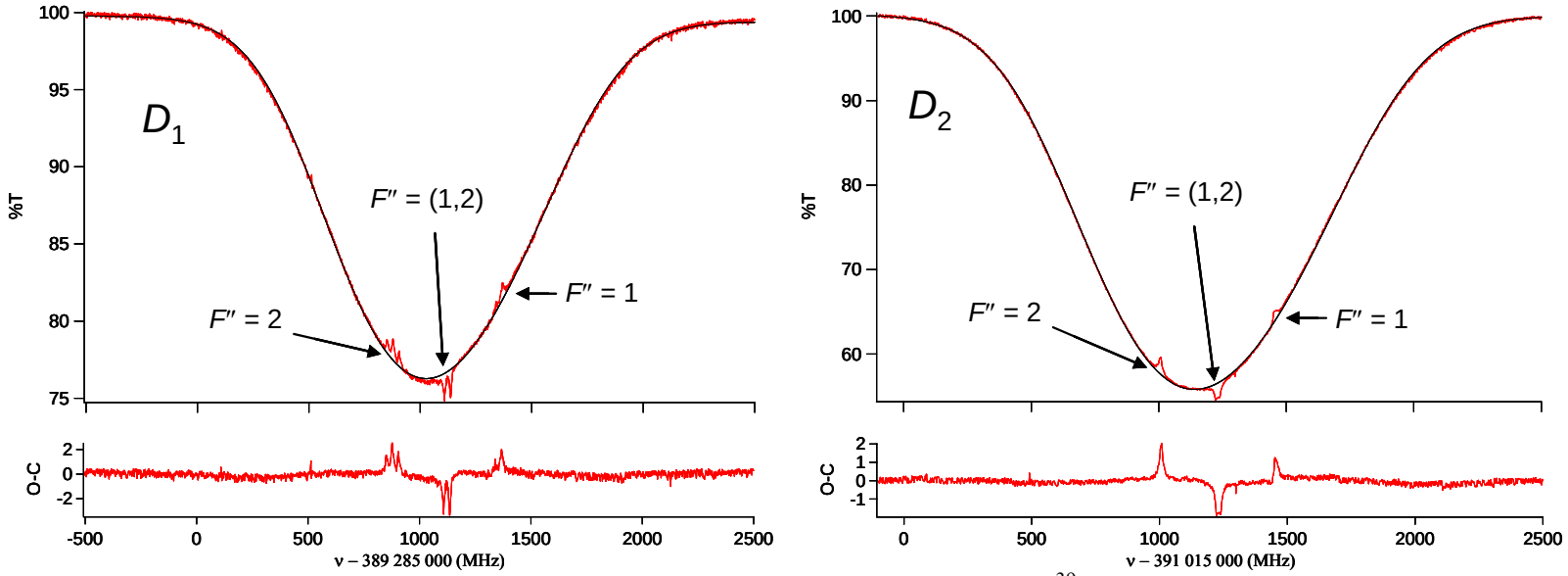

Figure 2.2. Saturation spectra of the transitions belonging to the D_1 and D_2 lines of ^{39}K. Hyperfine components are grouped according to lower state F quantum number. The fits shown are to the Doppler profile only, residual structure is the hyperfine components.

4.4 Results and Discussion

4.4.1 High Resolution Spectroscopy of ^{39}K

Typical saturation spectra of the ^{39}K D_1 and D_2 lines are shown in Fig. 4.2. Over the 2500 MHz frequency range shown in each panel of Fig. 4.2 the uncertainty in the frequency axis is directly tied to the HeNe, which has a long term uncertainty of ~500 kHz. All of the hyperfine components in the D_1 transition at 12985.185 cm^{-1} are reasonably well isolated. The nine predicted lines (four resonant, five crossover) are grouped in sets of three, each with common lower hyperfine level F as shown. The background Doppler feature was fit using the Beer-Lambert law and the sum of four Gaussian functions for the absorption coefficient centered on each of the resonant transition frequencies. The sub-Doppler lines were fit with Lorentzian profiles, where the parameters for the amplitude and center frequency were independent for each transition. The linewidth was assumed the same for all nine transitions and from the least-squares fits was determined to be 9.7 ± 0.7 MHz, full width half maximum (FWHM). This agrees reasonably well with the homogeneous linewidth of 6.0

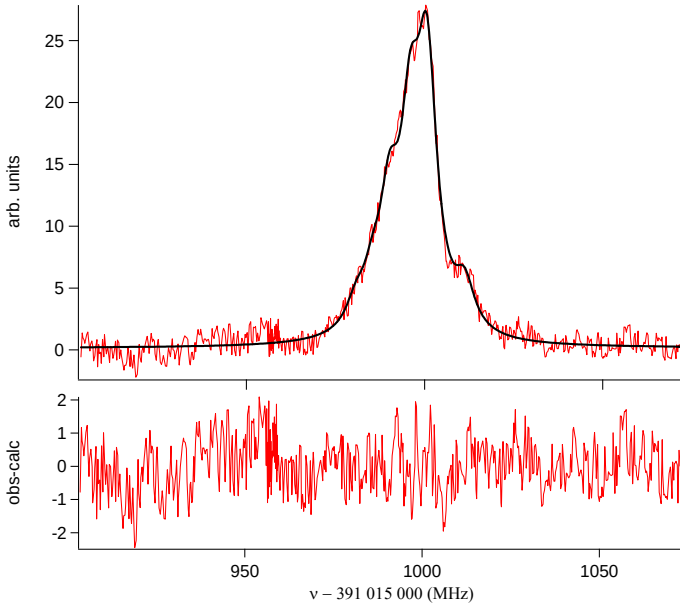

Figure 4.3. Recorded spectrum of the F = 2 hyperfine components of the ^{39}K D_2 line. The $F'' = 2 \rightarrow F' = 3$ transition is the indicated shoulder.

MHz expected from the lifetime of the excited state [27]; the difference is likely due to power broadening. To check the accuracy of our recorded spectrum, we measured the hyperfine splitting constant for the D_1 line to be A = 27.76 ± 0.05 MHz, in good agreement with the 27.775 ± 0.042 MHz value Falke et al. [16] measured using an optical frequency comb and confirming the quality of our frequency axis.

The ^{39}K D_2 line proved to be much more difficult to analyze due to the small hyperfine splitting in the $^2P_{3/2}$ state, A = 6.093(25) MHz [16], and the increased number of transitions originating from the same ground state. For instance, the cluster of lines originating from F = 2 comprised 6 transitions, 3 resonant and 3 crossover, all within 12 MHz of each other (Table 4.2, Fig. 4.3). The Doppler profile was fit in the same manner as the D_1 line except that six Gaussian functions were used, one for each of the resonant transitions. For the saturation transitions belonging to F = 2, the transition frequencies were fixed to the values in Table 4.3, which were based on the hyperfine splitting constants of Falke et al. [16] As in the case of D_1, all the widths were made the same.

4.4.2 Uncertainty Budget

The square of the combined standard uncertainty in frequency is derived from Eq. (4.1) by adding the component uncertainties in quadrature,

$$u_c^2(\nu_{probe}) = \Delta q^2 u^2(FSR) + \frac{\nu_{probe}^2}{\nu_{HeNe}^2}\left(4u^2(\Delta f_{AOM}) + u^2(\Delta\nu_{HeNe})\right) + u^2(\nu_{ref}) + u^2(\delta\nu_q)\,, \quad (4.2)$$

and including a term $\delta\nu_q$ equal to the line width of the ring-down cavity (representing the

limiting uncertainty with all other quantities being known). The square root of the first term in Eq. (4.2) $\Delta q \times u(\mathrm{FSR})$ represents the cumulative error accrued by moving an integral number of mode orders Δq from the reference line. This quantity will grow linearly with Δq and eventually will become the largest source of uncertainty in the absence of another reference point. The FSR is determined by measuring Δq_{21} and Δf_{A} as discussed above, and its standard uncertainty is

$$u(FSR) = \frac{1}{\Delta q_{21}} \sqrt{u^2(\nu_{D1}) + u^2(\nu_{D2})} \quad , \tag{4.3}$$

where Δq_{21} represents the integral number of ring-down cavity mode orders separating the reference transitions, and $u(\Delta\nu_{\mathrm{D1}})$ and $u(\Delta\nu_{\mathrm{D2}})$ are the uncertainties with which the respective ^{39}K lines located at $\nu_{\mathrm{ref}} = \nu_{D1}$ and $\nu_{\mathrm{ref}} = \nu_{D2}$ can be measured. The pair of reference transition uncertainties incorporates the Type B (systematic) uncertainty for their reported frequencies, the uncertainties in the fits to the saturation spectra, optical-power-induced shifts of the saturation spectra, and the uncertainties in the measured AOM frequency shifts. For our system, Δq_{21} is nominally 8560 and can be determined with 0 uncertainty given that initial wavelength-meter-based measurements give $u(\mathrm{FSR})/\mathrm{FSR} << 1/\Delta q_{21}$. Note that the $u(\nu_{\mathrm{ref}})$ term in Eq. (4.2) represents the combined uncertainty in the measurement of the specific ^{39}K transition frequency to which the scan is referenced, after the FSR has been determined. Substituting Eq. (4.3) into (4.2) gives the combined uncertainty

$$u_c^2(\nu_{probe}) = \left(\frac{\Delta q}{\Delta q_{21}}\right)^2 \times \left(u^2(\nu_{D1}) + u^2(\nu_{D2})\right) + \frac{\nu_{probe}^{\ 2}}{\nu_{HeNe}^2}\left(4u^2(\Delta f_{AOM}) + u^2(\Delta\nu_{HeNe})\right) + u^2(\nu_{ref}) + u^2(\delta\nu_q) \quad (4.4)$$

There are additional Type B (systematic) uncertainties that need to be considered, three of which are related to dispersion effects. In particular, we note that the FSR will depend to some extent on frequency because of: 1) group-delay dispersion (GDD) in the ion-beam-sputtered (IBS) quarter-wave stack (QWS) dielectric ring-down cavity mirrors, 2) broadband (non-resonant) frequency dependence of the refractive index, and 3) absorption by the sample gas. These effects will cause the comb of resonant frequencies to deviate slightly from a perfectly regular comb. The GDD effect causes changes in l (and hence changes in the round-trip resonance condition) because the intra-cavity beam penetration length into the mirrors varies with frequency [28, 29]. Thorpe et al. [30] and Diels et al. [31] measured the GDD of IBS-QWS dielectric mirrors, obtaining GDD values with magnitudes typically < 50 fs^2. The former measurements were in excellent agreement with theoretical predictions for GDD in IBS-QWS mirrors and for non-

Table 4.3. Component standard (1σ) uncertainties for the absolute frequency-axis determination of the FS-CRDS system.

	uncertainty	Description
FSR	64 Hz	Uncertainty in determination of FSR
$\Delta\nu_{HeNe}$	500 kHz	Long term stability of HeNe reference laser
$\delta\nu_q$	13 kHz	FWHM of the cavity resonance
Δf_{AOM}	1.5 kHz	Uncertainty in AOM frequency
ν_{D1}	100 kHz	Position and fitting of ^{39}K D_1 hyperfine line
ν_{D2}	250 kHz	Position and fitting of ^{39}K D_2 hyperfine line
O_2	100 kHz	Typical uncertainty in fit of O_2 positions
	15 kHz	Upper bound for dispersion of cavity modes

Combined total uncertainties are shown in Figure 4.4.

resonant dispersion by air. Based on calculations provided by the manufacturer, the GDD of our IBS-QWS mirrors varied linearly with frequency and ranged from −7.0 fs^2 at $\tilde{\nu}$ = 12975 cm^{-1} to −4.2 fs^2 at $\tilde{\nu}$ = 13115 cm^{-1}. Lehmann [32] estimates that absorption-induced dispersion (the third mechanism given above) shifts the frequencies of the ring-down cavity modes by $< c\alpha(6\pi)^{-1}$, where α is the absorption coefficient of the medium. Further, we note that for symmetric absorption line shapes, the dispersion has odd symmetry about the center of each absorption transition. Consequently, displacements in the resonant frequencies take on positive and negative values, leading to little net displacement relative to a uniformly spaced comb for frequencies far from the absorption lines. For the present study, we estimate the combined contribution of the three dispersive mechanisms to the overall frequency uncertainty to be less than 15 kHz.

The component uncertainties represented in Eq. (4.4) are given in Table 4.3 for the spectral range covered in this study. The evaluation of Eq. (4.4) depends on the choice of reference frequency (i.e. D_1 or D_2 transition of ^{39}K). In Fig. 4.4 we show the resulting frequency dependence of $u_c(\nu)$, where at a given frequency we have selected

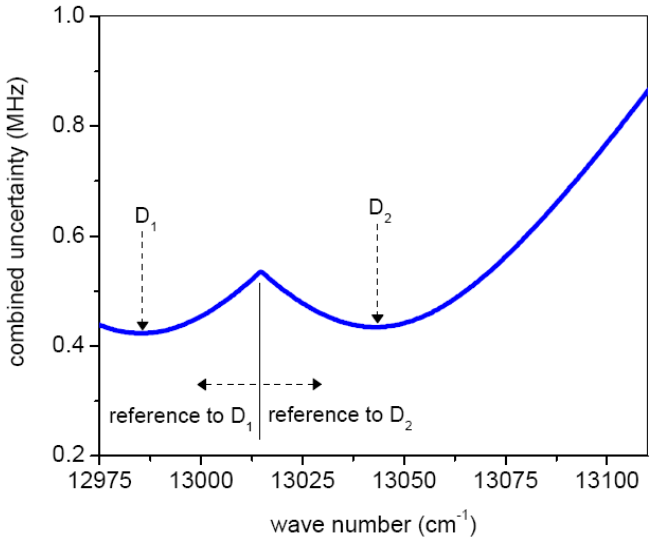

Figure 4.4. Combined standard uncertainty for the FS-CRDS frequency axis based on component uncertainties given in Table 4.3.

the minimum value of the two references frequency cases. The two largest component uncertainties driving $u_c(\nu)$ are $u(\Delta\nu_{HeNe})$ and $u(\nu_{D2})$, the former being dominated by variations in the FS-CRDS reference HeNe laser stability, and the latter by imprecision in measuring and fitting the hyperfine spectrum of the ^{39}K D_2 F'' = 2 group of transitions. The FS-CRDS reference laser was a commercial, polarization-stabilized HeNe laser, emitting at 633 nm, for which the manufacturer specified a stability of ± 2 MHz over an 8 hour period. We also measured variations in this laser by beating it against an I_2-stabilized HeNe having a long-term frequency stability <10 kHz. These measurements revealed that short-term (10 min) frequency variation in the FS-CRDS reference laser were < 200 kHz, whereas over a time scale of 8 hours, excursions as large as 1 MHz were observed. The effect of slow variation in the FS-CRDS reference frequency was also quantified by repeated measurement of the well-resolved crossover transition peak locations in the ^{39}K D_1 line (where the positions were measured *vis á vis* the FS-CRDS frequency axis). These tests presumably captured the effect of variations in the FS-CRDS reference laser occurring over the several-hour time scale required for spectral acquisition and yielded a standard deviation in peak positions of about 0.4 MHz, which after weighting by the ratio ν_{HeNe}/ν_{probe} corresponds to $\Delta\nu_{HeNe}$ = 0.5 MHz.

4.4.3 O_2 A-*Band Line Positions*

The line positions of 32 transitions of the O_2 *A*-band are listed in Table 4.4. The total cell pressure was chosen to reduce the influence of pressure shifting on our

Table 4.4. Transition wave numbers of the O_2 *A*-band in cm^{-1}.

Assignment $\Delta N\ N''\ \Delta J\ J''$	J'	Observed (cm^{-1})	Δ_{O-C} ($10^{-6}cm^{-1}$)	δ, $cm^{-1}\ atm^{-1}$	Assignment $\Delta N\ N''\ \Delta J\ J''$	Observed (cm^{-1})	Δ_{O-C} ($10^{-6}cm^{-1}$)	δ, $cm^{-1}\ atm^{-1}$
P3 P3	2	13112.015874 (29)	5.0	–0.0056 (2)	P3 Q2	13114.100191 (31)	4.9	–0.0051 (3)
P5 P5	4	13105.616870 (27)	0.7	–0.0066 (1)	P5 Q4	13107.628462 (28)	–0.8	–0.0063 (2)
P7 P7	6	13098.848235 (25)	–4.6	–0.0070 (1)	P7 Q6	13100.821746 (26)	0.2	–0.0071 (2)
P9 P9	8	13091.710358 (23)	4.2	–0.0077 (1)	P9 Q8	13093.655837 (24)	8.9	–0.0070 (1)
P11 P11	10	13084.203380 (21)	2.0	–0.0079 (1)	P11 Q10	13086.125133 (22)	9.9	–0.0072 (1)
P13 P13	12	13076.327289 (20)	13.8	–0.0078 (1)	P13 Q12	13078.227526 (20)	–4.1	–0.0074 (1)
P15 P15	14	13068.081801 (19)	–3.3	–0.0074 (1)	P15 Q14	13069.961877 (20)	–7.3	–0.0074 (1)
P17 P17	16	13059.466516 (18)	0.8	–0.0074 (1)	P17 Q16	13061.327271 (19)	8.7	–0.0074 (1)
P19 P19	18	13050.480744 (18)	–4.3	–0.00826 (70)	P19 Q18	13052.322732 (18)	–2.9	–0.00744 (25)
P21 P21	20	13041.123662 (18)	24.9	–0.00837 (34)	P21 Q20	13042.947277 (20)	6.7	–0.00819 (19)
P23 P23	22	13031.394095 (23)	0.7	–0.00874 (8)	P23 Q22	13033.199679 (26)	–2.1	–0.00898 (37)
P25 P25	24	13021.290837 (18)	11.2	–0.00896 (8)	P25 Q24	13023.078606 (22)	–15.0	–0.00874 (11)
P27 P27	26	13010.812345 (19)	3.0	–0.00912 (9)	P27 Q26	13012.582476 (49)	–6.2	–0.00902 (9)
P29 P29	28	12999.956863 (22)	–22.2	–0.00922 (6)	P29 Q28	13001.709512 (23)	0.3	–0.00926 (5)
P31 P31	30	12988.722550 (39)	41.8	–0.00934 (13)	P31 Q30	12990.457781 (31)	25.4	–0.00908 (10)
P33 P33	32	12977.106959 (89)	–74.0	–0.01068 (16)	P33 Q32	12978.824958 (90)	–42.1	–0.00922 (13)

Δ_{O-C} refers to the difference between the observed value and the calculated value determined by a least-squares fit of the molecular constants. Pressure shifting values, δ, in units of $cm^{-1}\ atm^{-1}$ are from reference [22]. Shifts for $J = 16$ were not measured and are estimated values. Note that the two transitions on the same row involve the same upper state energy level and thus provide an assessment of the experimental precision.

measurements while at the same time minimizing the fit uncertainty in the *A*-band positions. Pressure shifts at 1 Torr are ~1×10^{-5} cm^{-1} based on our recent measurement of the pressure shifting coefficient [22], approximately a factor of 2 smaller than our line position uncertainty. As seen in Table 4.5, our line position accuracy, ~600 kHz (2×10^{-5} cm^{-1}), is nearly two orders of magnitude better than previously reported positions [5, 6, 9, 33]. The current HITRAN database [34], based on the study of Brown and Plymate [5], is compared to our results in Fig. 4.5. Positions in the current study are approximately (13 ± 3) MHz (4×10^{-4} cm^{-1}) lower than that of Brown and Plymate. In addition, a systematic discrepancy of –77 kHz/cm^{-1} is observed between the two datasets, likely due to the calibration of the FTS frequency axis the study of Brown and Plymate.

Upper state energy levels were determined using the reported transition frequencies in Table 4.4 and the lower state energies of Rouillé et al. [35] relative to the $N'' = 1$, $J'' = 0$ level. These energy levels were fit using the expression, $E = T + BJ(J+1) - DJ^2(J+1)^2 + HJ^3(J+1)^3$, with each energy level weighted by the position uncertainty. The values for the retrieved molecular constants are shown in Table 4.5 along with values from previous studies [5-7]. The molecular constants determined in this study are in good agreement with previous results. Also shown in Table 4.5 is the rms observed - calculated positions, 1.9×10^{-5} cm^{-1}, which is in excellent agreement with the estimated uncertainty in the line positions (2×10^{-5} cm^{-1}) and further confirms our reported precision.

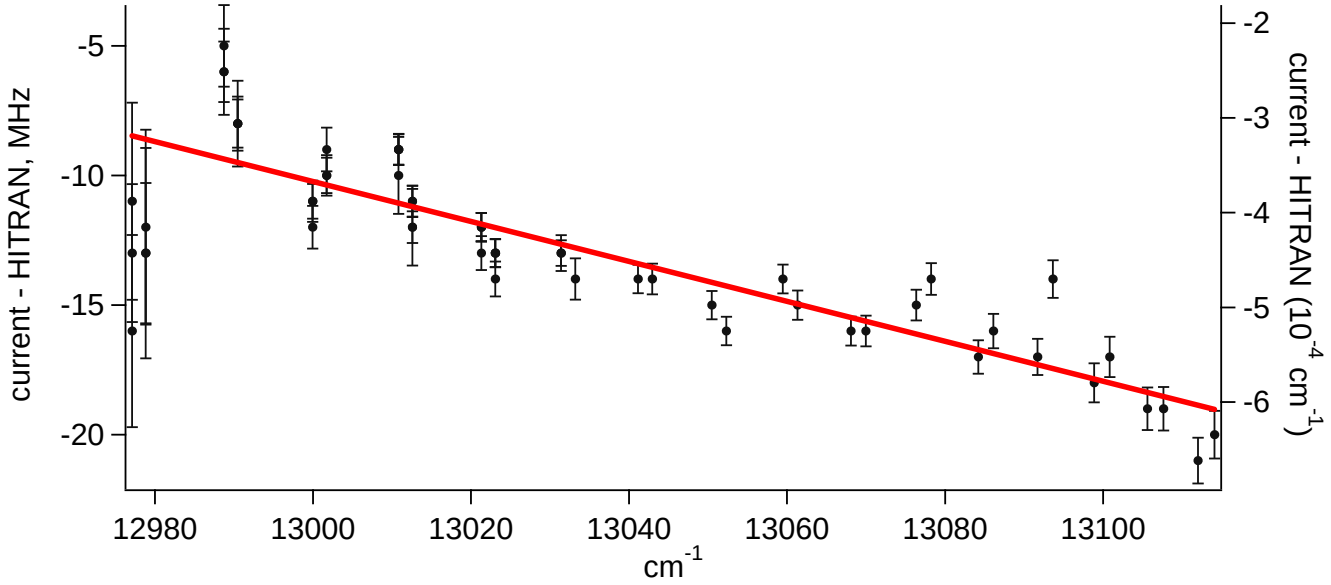

Figure 4.5. Comparison of O_2 *A*-band positions from the current study with the HITRAN2004 database. Error bars represent the total uncertainty (1 σ) in the line position and are typically 600 kHz. Error bars for positions below 12995 cm^{-1} are larger due to larger fit uncertainties corresponding to weak signal-to-noise. The slope of the line is –77 kHz/cm^{-1}.

Table 4.5. Molecular constants for the $b^1\Sigma_g^+$ state of $^{16}O_2$

	T (cm^{-1})	B (cm^{-1})	D ($10^{-6}cm^{-1}$)	H ($10^{-12}cm^{-1}$)	$\sigma_{O\text{-}C}$ ($10^{-4}cm^{-1}$)
This work	13122.00575 (1)	1.3912496 (1)	5.3699 (3)	−1.8 (2)	0.19
Brown and Plymate[a] [5]	13122.0064 (2)	1.391251 (2)	5.373 (5)		4
Kanamori et al. [6]	13122.0071 (8)	1.391247 (5)	5.369 (4)		20
O'Brien et al.[b] [7]	13122.0071 (10)	1.391344 (2)	5.352 (4)	−1.2 (2)	4

Numbers in parentheses are 1σ fit uncertainty in the last digit.
[a]Molecular constants derived using published positions. [b]Combined fit using the data of O'Brien et al. [7] and Brown and Plymate [5].
$\sigma_{O\text{-}C}$ is the standard deviation of the observed – calculated positions.

4.5 Conclusions

Line positions for the O_2 *A*-band have been calibrated against the potassium *D* lines with a typical uncertainty of ~ 2×10^{-5} cm^{-1} (600 kHz), improving the previous accuracy by nearly two orders of magnitude. Recording line positions against the precisely known ^{39}K *D* lines [16] makes the O_2 *A*-band a highly convenient frequency standard in the visible region.

This work accentuates the advantages of recording molecular spectra against atomic resonances using the frequency stabilized cavity ring-down spectroscopy technique. The use of other well-studied atomic lines such as Rb [36] at 778 nm or Cs [37] at 852 nm should prove highly useful in recording molecular spectra throughout the visible and, via frequency doubling, the near-IR.

Acknowledgements

Part of the research described in this paper was performed at the Jet Propulsion Laboratory, California Institute of Technology, under contract with The National Aeronautics and Space Administration (NASA). Additional support was provided by the Orbiting Carbon Observatory (OCO) project, a NASA Earth System Science Pathfinder (ESSP) mission; the NASA Upper Atmospheric Research Program grant NNG06GD88G; and the NIST Office of Microelectronics Program. Laurence Y. Yeung would like to acknowledge the support of the Davidow Graduate Fellowship in Environmental Science. We would also like to acknowledge Jeffrey Anderson (NIST Fabrication Technology

Division) for preparing the potassium reference cell and Dr. Craig Sansonetti (NIST Atomic Physics Division) and Roman Ciuryło (*Uniwesytet Mikołaja Kopernika)* for useful discussions on saturation spectroscopy.

References

[1] D.M. O'Brien, S.A. English, G. DaCosta, J. Atmos. and Ocean. Tech. 14 (1997) 105-119.

[2] K. Chance, J. Quant. Spectrosc. Radiat. Transfer 58 (1997) 375-378.

[3] S. Corradini, M. Cervino, J. Quant. Spectrosc. Radiat. Transfer 97 (2006) 354-380.

[4] B. van Diedenhoven, O.P. Hasekamp, I. Aben, Atmos. Chem. Phys. 5 (2005) 2109-2120.

[5] L.R. Brown, C. Plymate, J. Mol. Spectrosc. 199 (2000) 166-179.

[6] H. Kanamori, M. Momona, K. Sakurai, Can. J. Phys. 68 (1990) 313-316.

[7] L.C. O'Brien, H. Cao, J.J. O'Brien, J. Mol. Spectrosc. 207 (2001) 99-103.

[8] A.J. Phillips, F. Peters, P.A. Hamilton, J. Mol. Spectrosc. 184 (1997) 162-166.

[9] R. Schermaul, R.C.M. Learner, J. Quant. Spectrosc. Radiat. Transfer 61 (1999) 781-794.

[10] R. Schermaul, J. Quant. Spectrosc. Radiat. Transfer 62 (1999) 181-191.

[11] D.R.T. Appadoo, R.J. Le Roy, P.F. Bernath, S. Gerstenkorn, P. Luc, J. Verges, J. Sinzelle, J. Chevillard, Y. D'Aignaux, J. Chem. Phys. 104 (1995) 903-913.

[12] H. Salami, A.J. Ross, J. Mol. Spectrosc. 233 (2005) 157-159.

[13] H. Knockel, B. Bodermann, E. Tiemann, European Physical Journal D 28 (2004) 199-209.

[14] W. Whaling, W.H.C. Anderson, M.T. Carle, J.W. Brault, H.A. Zarem, Journal of Research of the National Institute of Standards and Technology 107 (2002) 149-169.

[15] W. DeGraffenreid, C.J. Sansonetti, J. Opt. Soc. Am. B: Opt. Phys. 19 (2001) 1711-1715.

[16] S. Falke, E. Tiemann, C. Lisdat, H. Schnatz, G. Grosche, Phys. Rev. A 74 (2006) DOI: 10.1103/PhysRevA.74.032503.

[17] J.T. Hodges, R. Ciurylo, Rev. Sci. Instrum. 76 (2005) 023112.

[18] J.T. Hodges, H.P. Layer, W.W. Miller, G.E. Scace, Rev. Sci. Instrum. 75 (2004) 849-863.

[19] J.T. Hodges, D. Lisak, Appl. Phys. B 85 (2006) 375-382.

[20] D. Lisak, J.T. Hodges, R. Ciurylo, Phys. Rev. A 73 (2006) 012507.

[21] D. Lisak, J.T. Hodges, Appl. Phys. B (2007) doi:10.1007/s00340-007-2691-x.

[22] D.J. Robichaud, J.T. Hodges, L.R. Brown, D. Lisak, P. Maslowski, M. Okumura, C.E. Miller, J. Mol. Spectrosc. (2007) submitted.

[23] D. Halmer, G. von Basum, P. Hering, M. Murtz, Rev. Sci. Instrum. 75 (2004) 2187-2191.

[24] L. Galatry, Phys. Rev. 122 (1961) 1218-1223.

[25] B. Shirinzadeh, C.C. Wang, Appl. Opt. 22 (1983) 3265-3270.

[26] P. Buck, I.I. Rabi, Phys. Rev. 107 (1957) 1291-1294.

[27] H. Wang, P.L. Gould, W.C. Stwalley, J. Chem. Phys. 106 (1997) 7899-7912.

[28] D.I. Babic, S.W. Corzine, IEEE J. Quantum Electron. 28 (1992) 514-524.

[29] C.J. Hood, H.J. Kimble, J. Ye, Phys. Rev. A 64 (2001) 038804.

[30] M. Thorpe, R. Jones, K. Moll, J. Ye, R. Lalezari, Opt. Exp. 13 (2005) 882-888.

[31] J.-C. Diels, R.J. Jones, L. Arissian, in: *Femtosecond Optical Frequency Comb Technology: Principle, Operation, and Applications*, J. Ye; S. T. Cundiff, (Eds.) Academic Press: New York, 2004.

[32] K.K. Lehmann, in: *Cavity-Ringdown Spectroscopy: An Ultratrace-Absorption Measurement Technique*, K. A. Busch; M. A. Busch, (Eds.) Oxford U. Press: Oxford, UK, 1998.

[33] A.J. Phillips, P.A. Hamilton, J. Mol. Spectrosc. 174 (1995) 587-594.

[34] L.S. Rothman, D. Jacquemart, A. Barbe, D.C. Benner, M. Birk, L.R. Brown, M.R. Carleer, C. Chackerian, K. Chance, L.H. Coudert, V. Dana, V.M. Devi, J.M. Flaud, R.R. Gamache, A. Goldman, J.M. Hartmann, K.W. Jucks, A.G. Maki, J.Y. Mandin, S.T. Massie, J. Orphal, A. Perrin, C.P. Rinsland, M.A.H. Smith, J. Tennyson, R.N. Tolchenov, R.A. Toth, J. Vander Auwera, P. Varanasi, G. Wagner, J. Quant. Spectrosc. Radiat. Transfer 96 (2005) 139-204.

[35] G. Rouillé, G. Millot, R. Saint-Loup, H. Berger, J. Mol. Spectrosc. 154 (1992) 372-382.

[36] J. Ye, S. Swartz, P. Jungner, J.L. Hall, Opt. Lett. 21 (1996) 1280-1282.

[37] T. Udem, J. Reichert, T.W. Hanch, Phys. Rev. A 62 (2000) 031801.

CHAPTER 5

Experimental Line Parameters of the Oxygen *A*-Band Using Frequency-Stabilized Cavity Ring-Down Spectroscopy

Part of this chapter was submitted for publication as:

D.J. Robichaud, J.T. Hodges, L.R. Brown, D. Lisak, P. Maslowski, M. Okumura, C.E. Miller, "Experimental Line Parameters of the Oxygen *A*-Band Using Frequency-Stabilized Cavity Ring-Down Spectroscopy," J. Mol. Spectrosc. (2007) submitted.

5.1 Abstract

Line intensities, self- and air-broadened linewidths, pressure-induced shifts, and collisional narrowing coefficients were measured from $2 \leq J' \leq 32$ in the *P* branch of the O_2 *A*-band (12,975 – 13,115 cm^{-1}). Spectra were recorded using the frequency-stabilized cavity ring-down spectrometer located at NIST, Gaithersburg, MD with a spectral resolution < 0.0001 cm^{-1} and noise-equivalent absorption coefficient of 6×10^{-10} cm^{-1} $Hz^{-1/2}$. The line intensities determined in the present work are ~1% lower than the values in current spectroscopic databases. However, we measure broadening coefficients that are up to 20% lower than the extrapolated values given in HITRAN 2004. We discuss the implications of our results for accurate remote sensing of surface pressure and photon pathlength distributions.

5.2 Introduction

Almost every physical phenomenon that influences the radiative transfer of a planetary body can be detected and quantified from the variation of specific spectral features [1]. However, the accuracies of molecular parameters are usually the limiting factor in the determination of atmospheric quantities like pressure and temperature from remote sensing spectra. The near infrared absorption of the O_2 *A*-band [2], shown in Fig. 5.1, has been used since the 1960's to determine cloud top heights, cloud optical properties, and aerosol optical thickness [3]. Such studies have been extended to the *A*-band spectra from the GOME [4] and SCIAMACHY [5, 6] satellite instruments. These applications required high radiometric precision but did not resolve individual O_2 rovibronic absorption features.

O'Brien and coworkers [3, 7] demonstrated the feasibility of combining high radiometric precision with high spectral resolution in O_2 *A*-band measurements from the

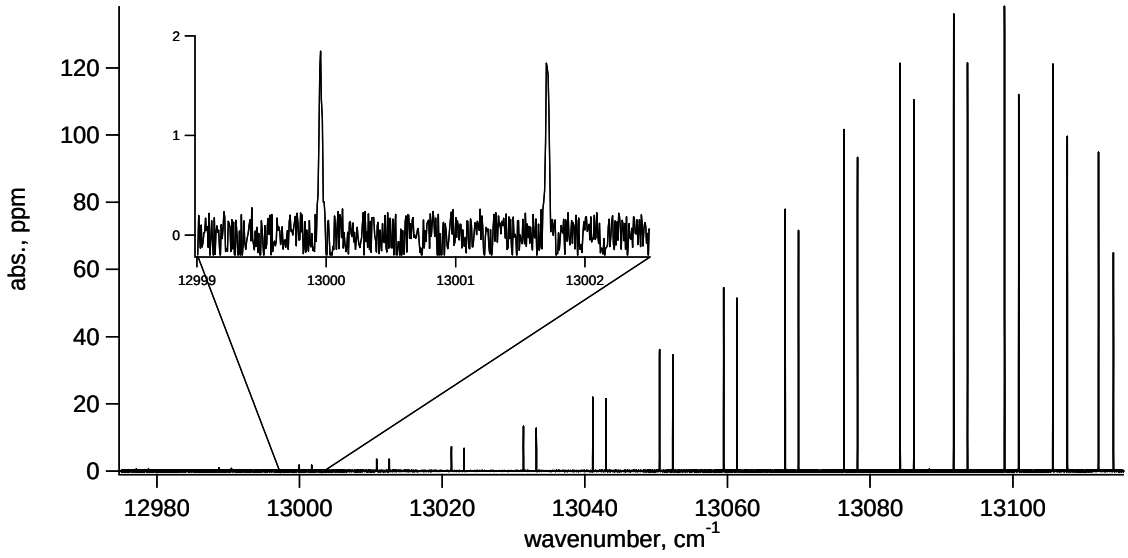

Figure 5.1. Recorded absorption spectrum of the *PP* and *PQ* branch of the O_2 *A*-band with empty cavity losses and Rayleigh scattering subtracted. Effective pathlength is 3.5 km, and the sample pressure is 1.02 Torr of NIST standard air at 295.2 K. Inset shows the typical noise level of ~0.15 ppm near the $J' = 28$ transitions.

ground and from aircraft to retrieve surface pressure with a precision of 0.1% in the presence of clouds, aerosols, and real measurement noise. Heidinger and Stephens [8, 9] demonstrated that O_2 *A*-band spectra could be used to retrieve cloud and aerosol optical and physical properties by sampling a range of O_2 absorption depths in an atmosphere that exhibits both multiple scattering and gaseous absorption.

Yang et al. [10] recorded O_2 *A*-band absorption in direct solar spectra using a ground based high resolution Fourier transform spectrometer. This study demonstrated 0.2% retrieval precision for airmasses < 1.8. However, the lack of an accurate line shape characterization for the *A*-band limited the ultimate precision and accuracy of their retrievals. Error in the line shape parameterization resulted in spurious correlation between retrieved photon path scale factors and the airmasses at which the spectra were recorded. Additionally, Yang et al. needed to extrapolate air-broadened width and shift parameters for $J > 22$ since these were not available from HITRAN [11] and the atmospheric spectra extended past $J' = 50$. Yang et al.[10] speculated that the overestimation of absorption in the near wings and the underestimation of absorption in the far wings of each line could be due to line-mixing and collision induced absorption, respectively, and called for new laboratory measurements of the O_2 *A*-band line shape.

The failure of the Voigt line shape to reproduce O_2 *A*-band absorption features accurately is well established [12-14] and may account for the large disparity in reported band strengths [see Table 1 of Brown and Plymate [13]]. Yang et al. [10] also demonstrated that collision induced absorption (CIA) and line mixing, especially in the

Table 5.1. Summary of high-resolution spectroscopic experiments for the O_2 *A*-band in the past 20 years.

Study	Year	Technique	Focus	#	Band strength[a]
Current study	2007	FS-CRDS	Line param.	16	2.26 (1)
Anderson and Brecha [15]	2007	TDLAS	Line strength	49	2.10 (6)
Tran et al. [16]	2006	FTS	Line shape		2.29 (1)
Di Stefano [17, 18]	2004	Afterglow	Line strength	25	
Pope et al. [19]	2004	FTS	Press. broadening	42	
Hill et al. [20]	2003	FTS	Press. Shifts	37	
O'Brien et al. [2]	2001	ICLAS	Constants	80	
Yang et al. [21]	2000	ICLAS	Line param.	11	2.1-2.3
Brown and Plymate [13]	2000	FTS	Line param.	44	2.28 (4)
Cheah et al. [22]	2000	FTS	Line param.	59	1.9
Xu et al. [23]	1999	CRDS	Line strengths	6	2.28 (7)
Schermaul and Learner [24]	1999	FTS	Line param.	65	2.30 (1)
Van Zee et al. [25]	1999	CRDS	Instrument	1	2.25
Phillips et al. [26]	1997	FTS	Positions and shifts	53	
Kanamori et al. [27]	1990	Zeeman mod.	Positions	36	
Ritter and Wilkerson [14]	1987	Dye laser abs.	Line parameters	50	2.28 (4)

FS-CRDS: frequency stabilized cavity ring-down spectroscopy; TDLAS: tunable diode laser absorption spectroscopy; FTS: Fourier-transform spectroscopy; ICLAS: intracavity laser absorption spectroscopy; CRDS: cavity ring down spectroscopy. Band strengths for Anderson and Brecha, Yang et al. and Cheah et al., and Van Zee et al. are estimated based on their reported line strengths. Estimated band strengths for Yang et al. varied depending on which range of *J* was used.
[a]units of 10^{-22} cm^{-1}/(molecule cm^{-2}) at 296 K.

R-branch bandhead near 13,160 cm^{-1}, may be required to analyze the *A*-band spectrum. Shortly after this, Tran et al. [16] investigated line mixing effects for the *A*-band using theoretical calculations based on the energy corrected sudden (ECS) approximation method. Differences between experimental and calculated spectra were then used to extract the CIA contribution to the absorption. Tran et al. found that neglecting line mixing overestimates absorption in the line wings and underestimates absorption in the line cores. Despite attempts to correct for these effects, significant systematic errors remain (see Fig. 4 of Yang et al. [10]).

It is clear from these results that there are fundamental gaps in the spectroscopic reference data used for remote sensing of the O_2 *A*-band and that this currently limits the accuracy with which sub-orbital and satellite remote sensing data may be retrieved. Such limitations must be overcome to support the sub-1% retrieval goals of planned satellite remote sensing observations such as those to be made by NASA's Orbiting Carbon Observatory (OCO) [28-30]. The objective of the present work is to extend the O_2 *A*-band spectroscopic parameters of Brown and Plymate [13] to higher *J*-values using frequency-stabilized cavity ring-down spectroscopy [31-35].

The spectroscopic reference standard data for the O_2 *A*-band currently recommended by the HITRAN database [11] is based on the positions, widths, and shifts of Brown and Plymate [13] and intensities of [14]. Table 5.1 summarizes the high-resolution spectroscopy of the O_2 *A*-band over the last 20 years [2, 13-15, 17-24, 27, 36]. Brown and Plymate [13] provide a detailed summary of the work prior to 2000. Since

2000 there have been 6 additional high-resolution studies of the *A*-band. O'Brien et al. [2] used intracavity laser absorption spectroscopy to reinvestigate line positions and generated a new set of spectroscopic constants of the $b^1\Sigma_g^+$ state by combining their positions with those measured by Brown and Plymate [13]. Hill et al. [20] addressed the need for more detailed study of the pressure shifting coefficients. However, their results did not resolve the outstanding issues and there remain two sets of O_2 *A*-band pressure shift values: Hill et al. [20] and Phillips and Hamilton [26] report band averaged shifting coefficients around –0.009 cm^{-1} atm^{-1}, while Ritter [36] and Brown and Plymate [13] report values around –0.005 cm^{-1} atm^{-1}. The differences are made more perplexing by the fact that Brown and Plymate and Hill et al. see no difference in shifting coefficients with O_2 mole fraction in N_2, whereas Ritter and Phillips and Hamilton observe air-shifting coefficients that are ~50% larger than self-shifting coefficients. Anderson and Brecha [15] determined self-broadening coefficients which were on average 7% larger than the HITRAN values. This was in agreement with the FTS work of Pope et al. [19], who reported self and N_2 broadening coefficients 10% larger than those of HITRAN.

Three studies focused on line intensities. Yang et al. [21] used intracavity laser absorption spectroscopy to study eleven transitions, including some high *J* lines which had previously not been studied. Their low and high *J* transitions were systematically 5 – 10% lower than the intensities in HITRAN [11], while intermediate *J* transition intensities agreed with the HITRAN values within experimental uncertainty. Anderson and Brecha [15] used tunable diode laser absorption measurements to determine intensities of individual lines with an uncertainty of 3%, but their values were ~8% lower

than those reported in HITRAN. di Stefano [17, 18] determined relative line strengths from a series of afterglow experiments. Table 5.1 also lists the band strengths reported by each study. For studies that only reported intensities for a small number of transitions, we estimated a band strength value based on their average deviation from HITRAN line intensities. It is clear from these comparisons that we lack an experimental consensus on the spectroscopic parameterization of the O_2 *A*-band.

The remainder of this paper comprises discussion of the experimental apparatus and the measurement technique as well as presentation of observed line positions, intensities, shape and shift parameters and frequencies for $^{16}O_2$ *A*-band transitions from J' = 2 to 32. These results are compared to and incorporated with previous measurements, and the *J*-dependence for air- and self-broadening parameters is quantified over the range J' = 0 to 32.

5.3 Experimental Apparatus

The frequency-stabilized cavity ring-down spectrometer (FS-CRDS) located at the National Institute of Standards and Technology (NIST), Gaithersburg, MD has been described in detail previously [31-35]. A unique feature of the FS-CRDS setup is that the mirror-to-mirror distance of the optical cavity is actively stabilized to compensate for variations in the optical path length. This has two inherent benefits. First, the spectrum frequency axis is now linked to the free-spectral-range (FSR) of the ring-down cavity. This provides an extremely precise, accurate, and linear relative frequency axis without the need for calibration in terms of external étalons or reference gases. Second, the

spectral resolution of this setup is limited primarily by the uncertainty of the cavity mode position (<500 kHz), which is itself dependent on the frequency stability of the reference laser (<100 kHz) instead of the probe laser linewidth (>1 MHz). Further, in FS-CRDS the excitation of the cavity is inherently single-mode, thus leading to single exponential decay signals. Consequently, FS-CRDS offers a significant improvement over traditional cavity ring-down techniques enabling very precise measurements of absorption lineshapes as well as the measurement of sub-MHz-wide Doppler-free saturation features in low pressure spectra [34, 35]. In addition, FS-CRDS is not influenced by confounding instrumental functions found in Fourier-transform spectroscopy (FTS) experiments [37]. Finally, we note that given its relatively high detection sensitivity, the FS-CRDS technique is well-suited for quantitative measurements of weak transitions which are inaccessible to many other laboratory-based absorption spectrometers.

The ring-down cavity mirrors used in this study were selected specifically to optimize ringdown performance for the $22 \leq J' \leq 32$ range of the O_2 *A*-band *P*-branch (line intensities between 2×10^{-26} and 1×10^{-24} $cm^{-1}/(molecule\ cm^{-2})$ at 296 K) and had nominal transmission losses of 200 ppm (finesse ~ 15,000) centered at 13,050 cm^{-1}. The cavity length was nominally 74 cm. This corresponds to an effective pathlength of ~3.5 km. The system noise-equivalent absorption coefficient was approximately 6×10^{-10} $cm^{-1}\ Hz^{-1/2}$. Ring-down decays, having typical decay times of 4–12 μs, were measured using an 8 MHz Si-PIN photodetector and fit using the fitting algorithm of Halmer et al. [38] Ring-down decay times less than 4 μs suffered from nonlinear effects in the absorption signal due to the bandwidth of the photodetector. This limited the high end of

the pressure range used for individual transitions. The lowest pressure was the larger of 1 Torr or the pressure at which the signal-to-noise ratio of the spectrum decreased to ~500:1. Total pressures below 1 Torr were avoided to minimize the influence of pressure gauge uncertainties in our measurements.

Spectral scans were automated by two servos. The first servo adjusted the cavity length to keep the frequency-stabilized reference laser in resonance with a ring-down cavity mode and also enabled the cavity to track shifts in the reference laser frequency that were imposed by an acousto-optic modulator (AOM). This approach was used to realize sub-FSR-level steps by precisely displacing the frequency comb of the stabilized ring-down cavity. The second servo maintained lock of an external cavity diode laser (ECDL) to a TEM_{00} mode of the optical cavity. To scan the laser beyond the tuning range of the AOM, the ECDL was hopped to adjacent cavity modes by rapidly breaking the lock, tuning to the next longitudinal mode order of the ring-down cavity, and re-acquiring lock on the new mode. We emphasize that that the relative spectrum frequency axis was based on measurements of the AOM frequency and knowledge of the ring-down cavity FSR: two quantities having uncertainties less than 20 kHz (7×10^{-7} cm^{-1}) [35]. Absolute frequencies of the probe laser were measured at the start of each scan using a Michelson-interferometer wavelength meter with a standard uncertainty of 60 MHz (0.002 cm^{-1}).

The ECDL in these experiments had two mechanisms of frequency control. Fine control was utilized via a piezoelectric (PZT) transducer, up to 2 cm^{-1}, and coarse control

was made possible using a stepper motor (~0.3 cm^{-1}/step); both mechanisms were externally controllable by the computer. The data acquisition and scanning software were modified for these experiments to take advantage of this feature of the ECDL. Wavenumber scans of approximately 2 cm^{-1} in length were recorded using the PZT, as described above. At the end of the 2 cm^{-1} scan, the PZT was reset to its initial value, and the stepper motor and PZT were used to start the next scan at the same cavity mode at which the previous scan ended. The wavemeter was used to determine unambiguously that the laser was locked to the same cavity mode. Thus it was straightforward to record and combine numerous sequential 2 cm^{-1} spectra and combine them into a single global spectrum. This approach allowed for >100 cm^{-1} scans to be collected over hours to days of relatively unattended operation. In this configuration, spectra of up to 120 cm^{-1} long were recorded in a single 24-hour period.

All measurements were made at room temperature on static samples of synthetic air or pure O_2. The synthetic air mixtures were NIST standard reference material (SRM) 2659a and 2657a, hereafter referred to as "NIST standard air" and "NIST 2%," respectively. The NIST standard air mixture composition (expressed as molar

Table 5.2. Experimental Conditions

All scans
Finesse: 15,000
L_{eff}: 3,500 km
Resolution: <0.0001 cm^{-1}
Line Parameters
Step size: 50 MHz (0.00167 cm^{-1})
Scan range: 10 GHz, centered on spectral line
Typical scan time: 10 minutes
Conditions:
NIST standard air J = 18 to 32
Pure O_2 J = 22 to 32
Pressure: transition dependent (see Tables 5.3-5)
Temperature: 295-298 K

fractions) was 79.28% N_2, 20.720% ± 0.043% O_2, 0.0029% Ar, 0.00015% H_2O, and 0.001% unidentified residual species. The NIST 2% composition was 98.05% N_2, 1.9734% ± 0.0053% O_2, 0.004% Ar, 0.00011% H_2O, and 0.001% other residual species. The temperature was measured using a NIST-calibrated 2.4 kΩ thermistor in thermal contact with the outer wall of the cell. Temperatures range from 295-298 K, and no effort was used to stabilize or control the temperature of the cell. Typically, during the course of a single scan (0.3 cm^{-1}) the temperature varied by less than 0.1 K. Gas pressure was measured with two NIST-calibrated capacitance diaphragm gauges having full scale responses of 100 and 1000 Torr, respectively, and readout uncertainties of < 0.01%.

To determine intensities, widths and other lineshape parameters as a function of pressure, spectra of individual transitions were recorded at 50 MHz steps over 10 GHz-wide microwindows centered on the selected transition (Fig. 5.2); each scan took approximately 10 minutes. The Doppler

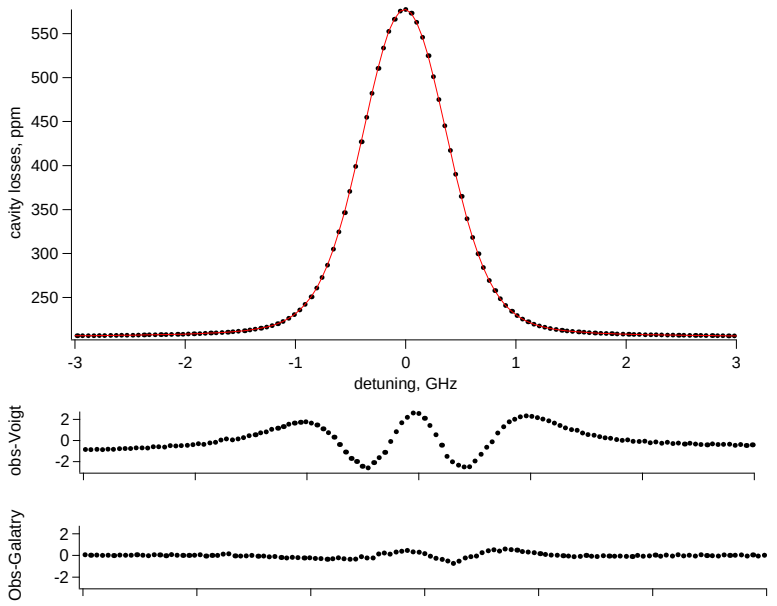

Figure 5.2. Observed (dots) and Galatry fit (line) of the *P*25 *P*25 transition of O_2. Effective pathlength is 3.5 km, and the sample pressure is 60 Torr of NIST standard air at 297.5 K. Signal to noise ratio was 6000:1. Residuals for both the Voigt and Galatry fits are shown (note the axis magnification). The asymmetric residual from the Galatry fit is due to speed dependent effects.

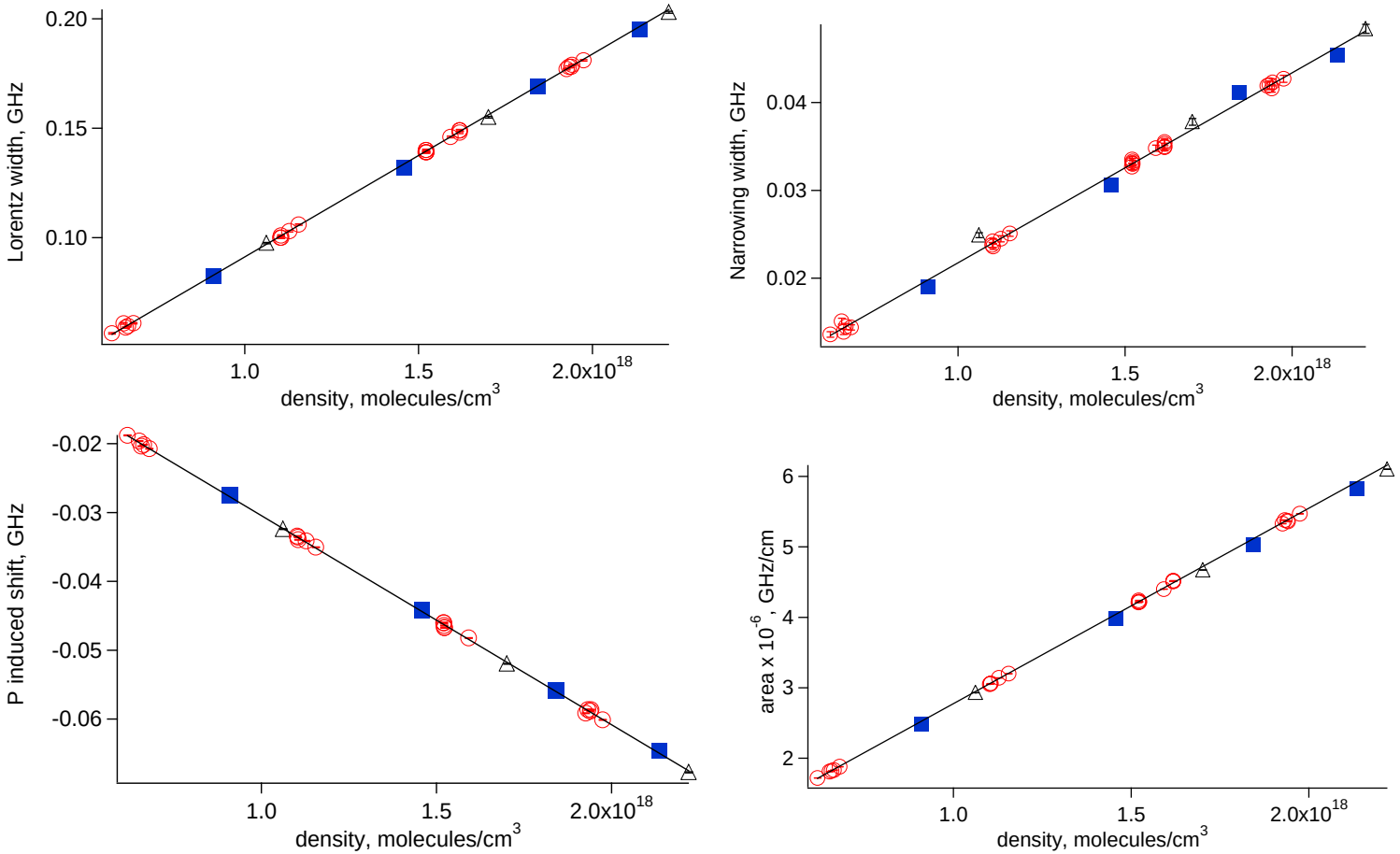

Figure 5.3. Galatry line shape parameters for the *P*25 *P*25 transition of the O_2 *A*-band in NIST standard air as a function of total cell density. This transition was measured over several months and shows the reproducibility of the measurements. Triangles: January 2007, squares: February 2007, circles: March 2007. All error bars are 1σ uncertainty.

width (full-width half maximum) of O_2 in this spectral region is ~850 MHz (0.028 cm^{-1}) at 296 K. Transitions with common J' were scanned together. The cell was recharged with NIST standard air or pure O_2 for each new pair. Typically, 4 to 6 different pressures were studied for each pair of transitions. All recorded transitions were fit using a Galatry [39] lineshape, which is based on the soft-collision model and generalizes the Voigt profile for Dicke narrowing effects. The Galatry lineshape has three shape parameters given by the Doppler, Lorentzian, and narrowing widths, respectively. In the soft-collision limit, the narrowing width is proportional to pressure and directly related to the mass diffusion coefficient of the absorber. Line intensities, pressure-induced broadening and shifting, and collisional narrowing coefficients (Fig. 5.3) were relaxed and determined from best fits of Galatry profiles to the data. Pressure-induced shifts were determined using the method described by Robichaud et al. [40] All of the scans recorded for pressures > 40 Torr exhibited the asymmetric residuals characteristic of speed-dependent lineshape effects, as shown in Fig. 5.2. Preliminary analyses indicated that the bias in the line intensity from neglecting speed dependence is less than 0.2%. The Galatry profile was adopted in this study so that a direct comparison to the Ritter and Wilkerson dataset could be made. A detailed study of speed-dependent effects in the oxygen *A*-band will be the subject of a future publication.

5.4 Results and Discussion

The *A*-band, $b^1\Sigma_g^+ \leftarrow X^3\Sigma_g^-$, is electronic dipole forbidden by both spin and orbital angular momentum selection rules, but is allowed through its magnetic dipole [41]. The rotational levels of the O_2 states are described by the angular momentum

quantum numbers N and J, where N is the rotational angular momentum, S is the spin angular momentum, and J is the total angular momentum, $J = N + S$. The $^3\Sigma_g^-$ ground state is split into three levels, $J'' = N''-1$, N'', and $N''+1$, with only odd values of N'' allowed due to spin statistical weights. The $b^1\Sigma_g^+$ upper state has only levels $J' = N'$, with even values of N' allowed. Therefore, the *A*-band comprises four types of transitions represented by $\Delta N\ N''\Delta J\ J''$, limited to *PP, PQ, RQ,* and *RR*. This study focused on the *PP*- and *PQ*-type transitions due to bandwidth limitations of our laser system. The *PP* and *PQ* transitions are separated by approximately 2 cm^{-1}, forming pairs in the *P* branch. The spacing between pairs range from 6 cm^{-1} at low J up to 12 cm^{-1} at J = 30.

The individual measurements for 16 transitions of the *P*-branch of the oxygen *A*-band are listed in Tables 5.3, 5.4, and 5.5 for NIST standard air, NIST 2%, and pure O_2 experiments, respectively. Line intensities in natural abundance are shown for both air and pure O_2 experiments in units of cm^{-1}/(molecule cm^{-2}) and corrected to 296 K. The pressure ranges over which the line parameters were measured are also reported.

Self- and air-shifting coefficients are reported in Tables 5.3, 5.4, and 5.5 and are effectively the same over the range of transitions measured. This agrees with Hill et al. [20] and Brown and Plymate [13], both of whom saw no change in pressure shift with O_2 molar fraction. However, Ritter [36] and Phillips and Hamilton [26] both reported N_2-shifting to be ~50% larger than self-shifting. Previous pressure-shifting coefficients in the O_2 *A*-band [13, 20, 22, 26, 42-45] have fallen into one of two groups, centered

Table 5.3: Measured Line Parameters of the Oxygen *A*-Band Using NIST Standard Air

Assignment $\Delta N\ N''\ \Delta J\ J''$	Position*	Intensity $\times 10^{-25}$	J'	Air-Half Width	Collisional Narrowing	Pressure-induced Shifts	Pressure range (Torr)	#scans
P19 Q18	13052.32325	20.82 (12)	18	0.04445 (29)	0.0105 (4)	–0.00744 (25)	1.5–10.5	12
P19 P19	13050.48125	22.13 (15)	18	0.04288 (36)	0.0129 (5)	–0.00826 (70)	1.5–10.5	12
P21 Q20	13042.94873	13.04 (3)	20	0.04048 (27)	0.0116 (4)	–0.00819 (19)	1.5–17	21
P21 P21	13041.12513	13.76 (3)	20	0.03993 (20)	0.0130 (3)	–0.00837 (34)	1.5–17	33
P23 Q22	13033.20013	7.641 (16)	22	0.04024 (17)	0.0155 (2)	–0.00898 (37)	1.5–32	10
P23 P23	13031.39453	8.022 (10)	22	0.03986 (14)	0.0169 (2)	–0.00874 (8)	1.5–32	12
P25 Q24	13023.07905	4.209 (5)	24	0.03765 (5)	0.0162 (1)	–0.00874 (11)	20–60	32
P25 P25	13021.29125	4.393 (6)	24	0.03808 (5)	0.0180 (1)	–0.00896 (8)	20–60	32
P27 Q26	13012.58286	2.179 (6)	26	0.03519 (5)	0.0162 (1)	–0.00902 (9)	20–140	17
P27 P27	13010.81266	2.269 (9)	26	0.03563 (5)	0.0185 (1)	–0.00912 (9)	20–140	17
P29 Q28	13001.70984	1.061 (5)	28	0.03313 (1)	0.0189 (1)	–0.00926 (5)	50–760	8
P29 P29	12999.95724	1.103 (4)	28	0.03334 (2)	0.0197 (1)	–0.00922 (6)	50–760	8
P31 Q30	12990.45804	0.483 (2)	30	0.03111 (3)	0.0181 (1)	–0.00908 (10)	100–760	6
P31 P31	12988.72274	0.500 (1)	30	0.03107 (3)	0.0188 (2)	–0.00934 (13)	100–760	6
P33 Q32	12978.82538	0.2098 (3)	32	0.02954 (10)	0.0245 (7)	–0.00922 (13)	429–755	7
P33 P33	12977.10738	0.2169 (3)	32	0.02987 (11)	0.0262 (8)	–0.01068 (16)	429–755	7

* Positions in cm^{-1} are HITRAN 2004 values, intensities are in units of $cm^{-1}/(molecule\ cm^{-2})$ at T=296 K and widths, collisional narrowing, and pressure shifts in units of $cm^{-1}\ atm^{-1}$ (normalized to T=296 K using the temperature-dependent exponent, n_{air}, from HITRAN 2004). The values in parentheses (1 σ uncertainty of the last digit) are Type A uncertainties and quantify the precision and reproducibility of the measurement. They are based on the quadrature sum of the fitted parameter uncertainties obtained by the Galatry lineshape fits and the standard deviation of repeated measurements. These uncertainties do not account for systematic effects associated with the lineshape model. Combined relative standard uncertainties in S_ν associated with the measurement of p, T, composition, and spectral frequency axes are estimated to be < 0.2 %. Measurements were performed for 4 to 6 pressures evenly spaced over the range reported (e.g. for J = 24 the pressures studied were 60, 47, 34, and 21 Torr).

Table 5.4: Measured Line Parameters of the Oxygen *A* Band Using Pure O_2

Assignment $\Delta N\ N''\ \Delta J\ J''$	Position*	Intensity $\times 10^{-24}$	J'	N_2 - Half Width	Collisional Narrowing	Pressure-induced Shifts
P3 P3	13114.10086	3.901 (8)	2	0.0577 (16)	0.012 (2)	–0.0051 (3)
P3 Q2	13112.01656	5.738 (8)	2	0.0584 (11)	0.015 (1)	–0.0056 (2)
P5 P5	13107.62910	5.974 (9)	4	0.0569 (11)	0.016 (1)	–0.0063 (2)
P5 Q4	13105.61750	7.557 (9)	4	0.0537 (9)	0.009 (1)	–0.0066 (1)
P7 P7	13100.82232	7.089 (9)	6	0.0531 (10)	0.009 (1)	–0.0071 (2)
P7 Q6	13098.84882	8.423 (10)	6	0.0524 (9)	0.009 (1)	–0.0070 (1)
P9 P9	13093.65632	7.256 (8)	8	0.0510 (9)	0.010 (1)	–0.0070 (1)
P9 Q8	13091.71092	8.262 (8)	8	0.0502 (8)	0.010 (1)	–0.0077 (1)
P11 P11	13086.12566	6.667 (7)	10	0.0476 (9)	0.008 (1)	–0.0072 (1)
P11 Q10	13084.20396	7.437 (7)	10	0.0498 (7)	0.013 (1)	–0.0079 (1)
P13 P13	13078.22800	5.608 (5)	12	0.0493 (8)	0.013 (1)	–0.0074 (1)
P13 Q12	13076.32780	6.113 (5)	12	0.0475 (7)	0.013 (1)	–0.0078 (1)
P15 P15	13069.96242	4.338 (4)	14	0.0461 (9)	0.015 (1)	–0.0074 (1)

* Positions in cm^{-1} are HITRAN 2004 values, intensities are in units of $cm^{-1}/(molecule\ cm^{-2})$ at T=296 K and widths, collisional narrowing, and pressure shifts in units of $cm^{-1}\ atm^{-1}$(T=296 K). Uncertainties area as reported in Table 5.3. All lines were measured at 34.50, 27.29, 19.90, and 10.99 Torr and 295.7 K.

Table 5.5: Measured Line Parameters of the Oxygen *A* Band Using Pure O_2

Assignment $\Delta N\ N''\ \Delta J\ J''$	Position*	Intensity $\times 10^{-25}$	J'	Self-Half Width	Collisional Narrowing	Pressure-induced Shifts	Pressure range (Torr)	# scans
P23 Q22	13033.20013	7.623 (29)	22	0.04100(112)	0.0154(10)	–0.00835(40)	1–6	8
P23 P23	13031.39453	7.992 (14)	22	0.04090(127)	0.0099(17)	–0.00834(45)	1–6	4
P25 Q24	13023.07905	4.205 (13)	24	0.03902 (68)	0.0160 (7)	–0.00914(27)	1–10.5	4
P25 P25	13021.29125	4.380 (14)	24	0.03891 (57)	0.0126 (7)	–0.00940(19)	1–10.5	6
P27 Q26	13012.58286	2.180 (3)	26	0.03861 (13)	0.0151 (8)	–0.00894(13)	4–20	4
P27 P27	13010.81266	2.268 (5)	26	0.03845 (16)	0.0153 (7)	–0.00877(12)	4–20	4
P29 Q28	13001.70984	1.063 (1)	28	0.03555 (26)	0.0150 (4)	–0.00914 (5)	15–50	4
P29 P29	12999.95724	1.1024 (4)	28	0.03607 (27)	0.0165 (5)	–0.00956 (7)	15–50	4
P31 Q30	12990.45804	0.4859 (6)	30	0.03425 (9)	0.0159 (2)	–0.00900 (7)	20–130	6
P31 P31	12988.72274	0.5038(13)	30	0.03411 (10)	0.0164 (2)	–0.00986 (7)	20–130	6
P33 Q32	12978.82538	0.2100 (6)	32	0.03236 (1)	0.0168 (1)	—	70–304	6
P33 P33	12977.10738	0.2164 (1)	32	0.03265 (5)	0.0168 (1)	—	70–304	6

* Positions in cm^{-1} are HITRAN 2004 values, intensities are in units of cm^{-1}/(molecule cm^{-2}) at T=296 K and widths, collisional narrowing, and pressure shifts in units of cm^{-1} atm^{-1}(T=296 K). Uncertainties area as reported in Table 5.3. Measurements were performed for 4 to 6 pressures evenly spaced over the range reported (e.g. for J = 24 the pressures studied were 10.5, 8, 5.5, and 3 Torr).

around –0.005 cm^{-1} atm^{-1} and –0.009 cm^{-1} atm^{-1} (see Table 1 in Hill et al. [20]) for $J <$ 22 transitions. Figure 5.4 compares these studies as a function of upper state J. In Fig. 5.4, the self-shifting coefficients are shown for Hill et al., Brown and Plymate, and Phillips and Hamilton. The N_2-shifting values for Phillips and Hamilton are approximately 0.005 cm^{-1} atm^{-1} lower than their self-shifting values and are not shown. Both the air- and self-shifting results of Ritter are also shown.

Accurate pressure shift measurements can be notoriously difficult to determine, as shifts are only a small portion of the linewidth; consequently, uncertainties up to 15-20% within a single study are not uncommon. However, it has been puzzling why recent high-resolution studies seem to cluster near two statistically distinct values. Although there are correlations between the datasets (for instance, the works of Hill et al. and Phillips and Hamilton used the zero-crossing method to determine line centers, whereas Brown and Plymate and Ritter determined line centers by fitting to symmetric profiles), it is likely the calibration of the frequency axis that leads to the most interesting result. Predoi-Cross et al. [46] calibrated their frequency axis using both CO and I_2 transitions. When using CO Predoi-Cross et al. retrieved pressure shifts in agreement with Brown and Plymate (who also used CO as a calibration reference) while using I_2 they retrieved shifts in accordance with Phillips and Hamilton (who used I_2). Pressure shifts in the current study were measured relative to an arbitrary cavity mode near a given O_2 transition [40], linking the shifts directly to the well-known FSR of the optical cavity (202.076539 MHz ± 100 Hz). Therefore, our values are insensitive to the calibration issues influencing the other studies.

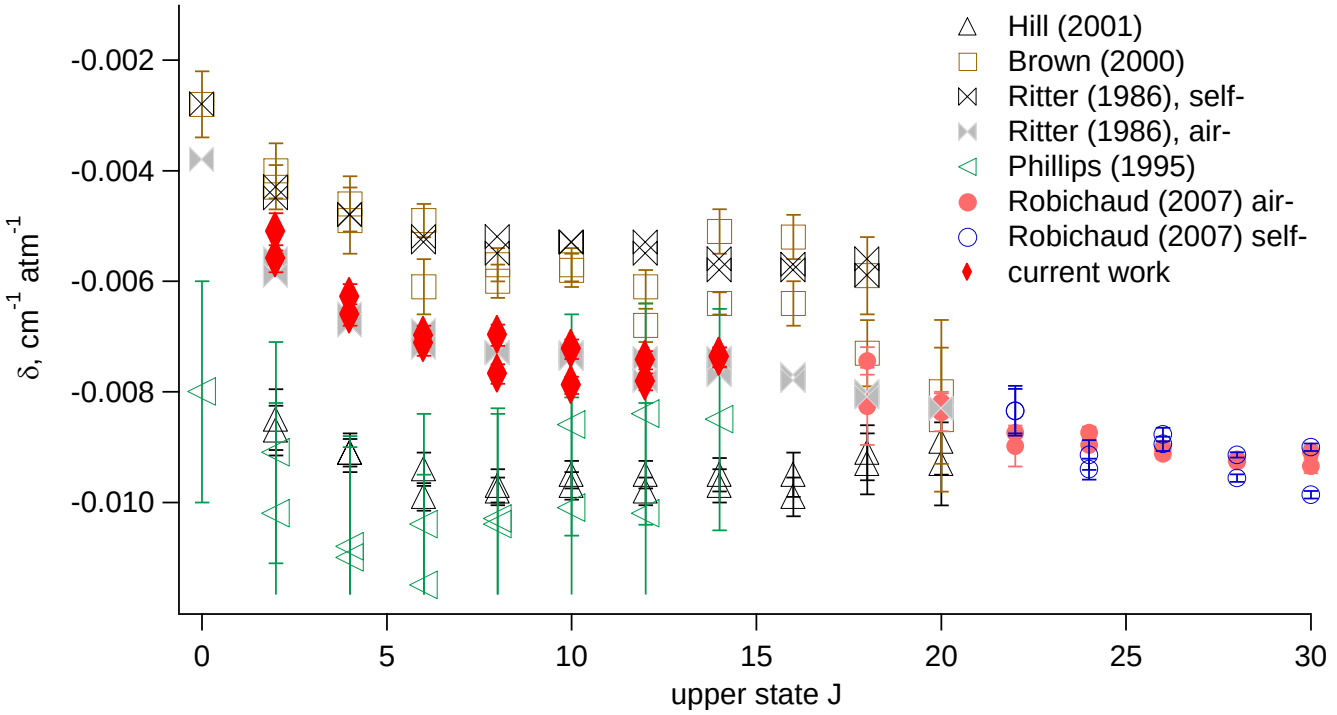

Figure 5.4. Pressure shifting coefficients, δ, as a function of J'. Only values of δ for the P-branch are shown. Uncertainties for the Ritter (open and closed bowties) are not known. All values are self-shifts unless otherwise stated.

The standard Type A line intensity uncertainties are shown in Tables 5.3-5 and are typically less than 0.5% of the measured value. Differences between the temperature measured by the thermistor on the outside of the cell and the true temperature inside the cell (<0.2 K) were likely the largest source of uncertainty in the reported precision due to the large temperature dependence on the line intensities in this region of the *A*-band (typically 1%/K). Indeed, during days in which the temperature stability of the room was good our precision was <0.1%.

Intensities, in units of $cm^{-1}/(molecule\ cm^{-2})$, were corrected to T=296 K using

$$S_i(296K) = S_i(T) \times \frac{q(T)}{q(296K)} \times \frac{e^{-E/k(296K)}}{e^{-E/kT}} \quad , \qquad (5.1)$$

where q(T) is the total partition function at temperature T, k is Boltzmann's constant, E is the lower state energy level from HITRAN, and S_i is the line intensity. Measurements made using pure O_2 and NIST standard air generally agree within their mutual uncertainties and are shown in Fig. 5.5 relative to current HITRAN values. The discrepancy at J = 30 is due to a blended transition with an O_2 $b^1\Sigma_g^+(v'=1) \leftarrow X\,^3\Sigma_g^-(v''=1)$ transition (e.g. hotband of the *B*-band). At the low pressures used in the pure O_2 study, the *B*-band

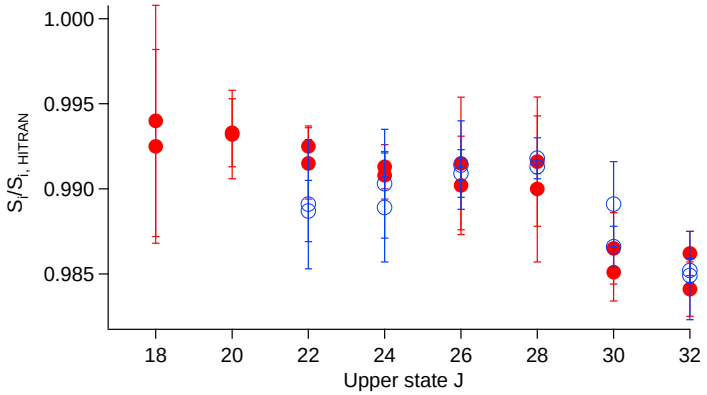

Figure 5.5. Line intensity ratio of NIST standard air (closed circles) and pure O_2 (open circles) relative to HITRAN as a function of J'. Error bars represent 1σ uncertainties as discussed in Table 3.

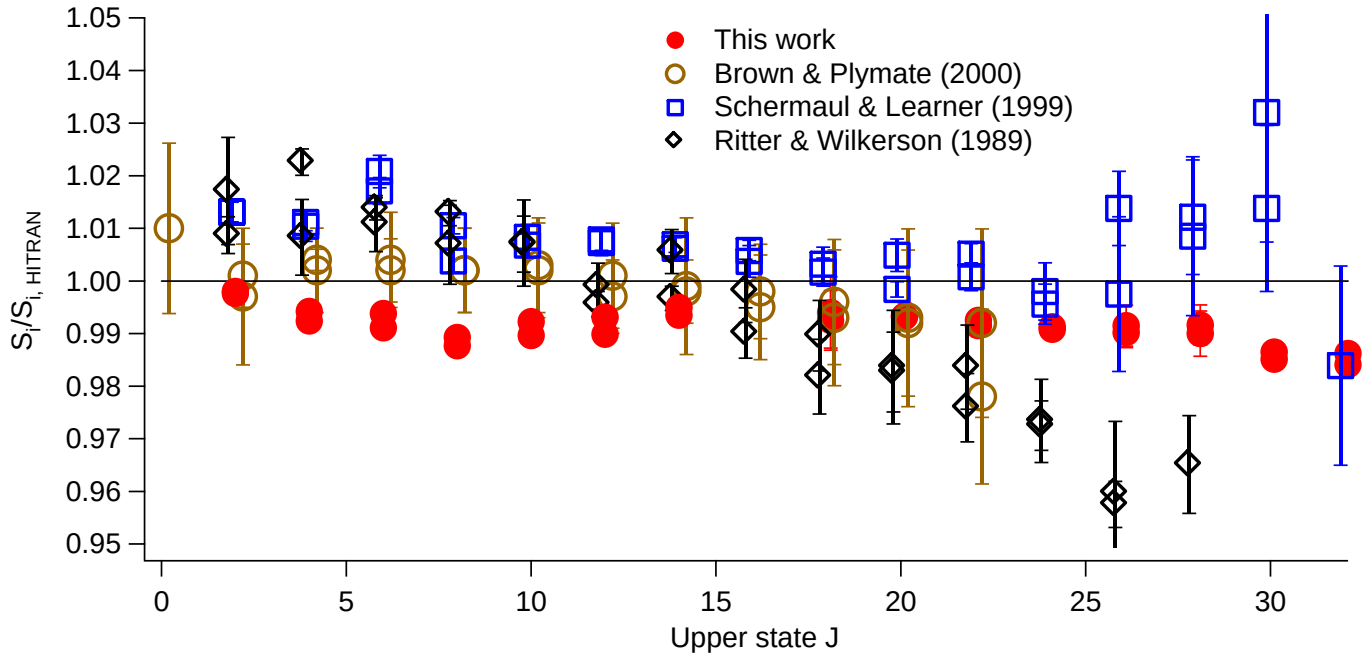

Figure 5.6. Ratio of experimental line intensities to HITRAN2004 as a function of upper state *J*. All error bars represent 1σ uncertainties. The current work line intensities are (0.9 ± 0.3) % lower than HITRAN 2004 with a typical uncertainty of 0.2% (see Table 4.1 caption details).

transition appeared as a shoulder to the J = 30 A-band feature and was readily fit. However, at the elevated pressures used in the NIST standard air measurements the B-band transition was effectively hidden by the pressure-broadened A-band line, making fitting the blended feature difficult. Therefore, the pure O_2 experiments yield more accurate results for this transition. Fig. 5.6 compares our intensities to those from HITRAN 2004 [11], Brown and Plymate [13], Schermaul and Learner [24], and Ritter and Wilkerson [14]. Note that the intensities in HITRAN 1996 [47] and later were calculated as described in Gamache et al. [48] and were based on the bandstrength of Ritter and Wilkerson, 2.28×10^{-22} $cm^{-1}/(molecule\ cm^{-2})$. Our line intensities lie in the middle of these studies and are (0.9 ± 0.3)% less than those of HITRAN 2004. Finally, our results do not support the need for a Herman-Wallis factor obtained by Schermaul and Learner [24].

Air- and self-broadening parameters are presented in Fig. 5.7. The air-broadened widths are consistently smaller than the corresponding self-broadened widths over the range of J studied. The ratio of air-/self-broadened widths ranges from 0.98 at J' = 22 to 0.92 at J' = 32. The J-dependence of the ratio is consistent with the study by Brown and Plymate

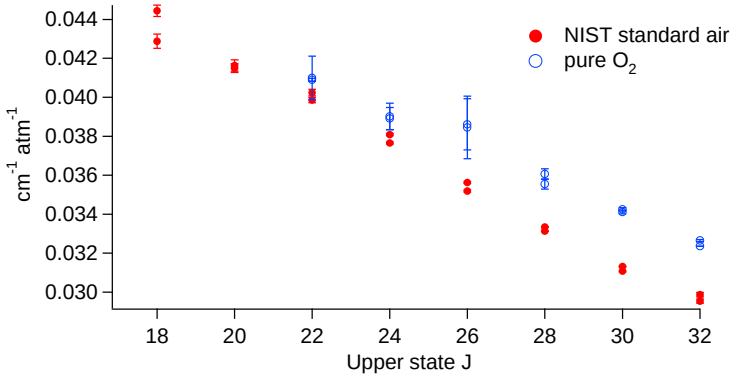

Figure 5.7. Air- (closed circles) and self- (open circles) broadening parameters as a function of upper state J at 296 K. Self-widths are always larger than air-widths for the region studied.

[13], who found that the ratio varied from 1.015 at low J' to 0.98 at $J' = 20$. The only other study to report on air- and self-broadened widths was Ritter and Wilkerson [14]. They found that the air-broadened widths were consistently larger than the corresponding self-broadened widths by 2 – 2.5% for the five air-broadened widths measured between $J' = 0$ and $J' = 20$. Similar to previous studies, there was no discernible difference between *PP* and *PQ* type widths of the same J'.

In Fig. 5.8, self-broadening parameters of the present work are compared with those of Brown and Plymate [13], Ritter and Wilkerson [14], and Yang et al. [21]. The only other high-resolution study that measured widths over a large number of transitions is the work of Pope et al. [19], which reported self-widths ~10% larger than any of the other studies; we do not consider the results of Pope et al. further. The HITRAN 2004 [11] self-widths, based solely on the data of Brown and Plymate [13], are also shown in Fig. 5.8. Clearly, the extrapolation used in HITRAN does not reproduce the measured self-broadened width coefficients for high-*J*. Yang and coworkers [10] also found that the high-*J* HITRAN widths were not optimal in fitting their high-resolution atmospheric *A*-band spectra. To address this shortcoming they determined a new functional form for the self-widths based on the available data from both the *A*-band and the 1.27 μm $a^1\Delta_g(\nu = 0) \leftarrow X^3\Sigma_g^-(\nu = 0)$ band. The data in Fig. 5.8 were fit using the empirical expression of Yang et al. [10]:

$$HWHM = A + \frac{B}{1 + c_1 J' + c_2 J'^2 + c_3 J'^4} . \qquad (5.2)$$

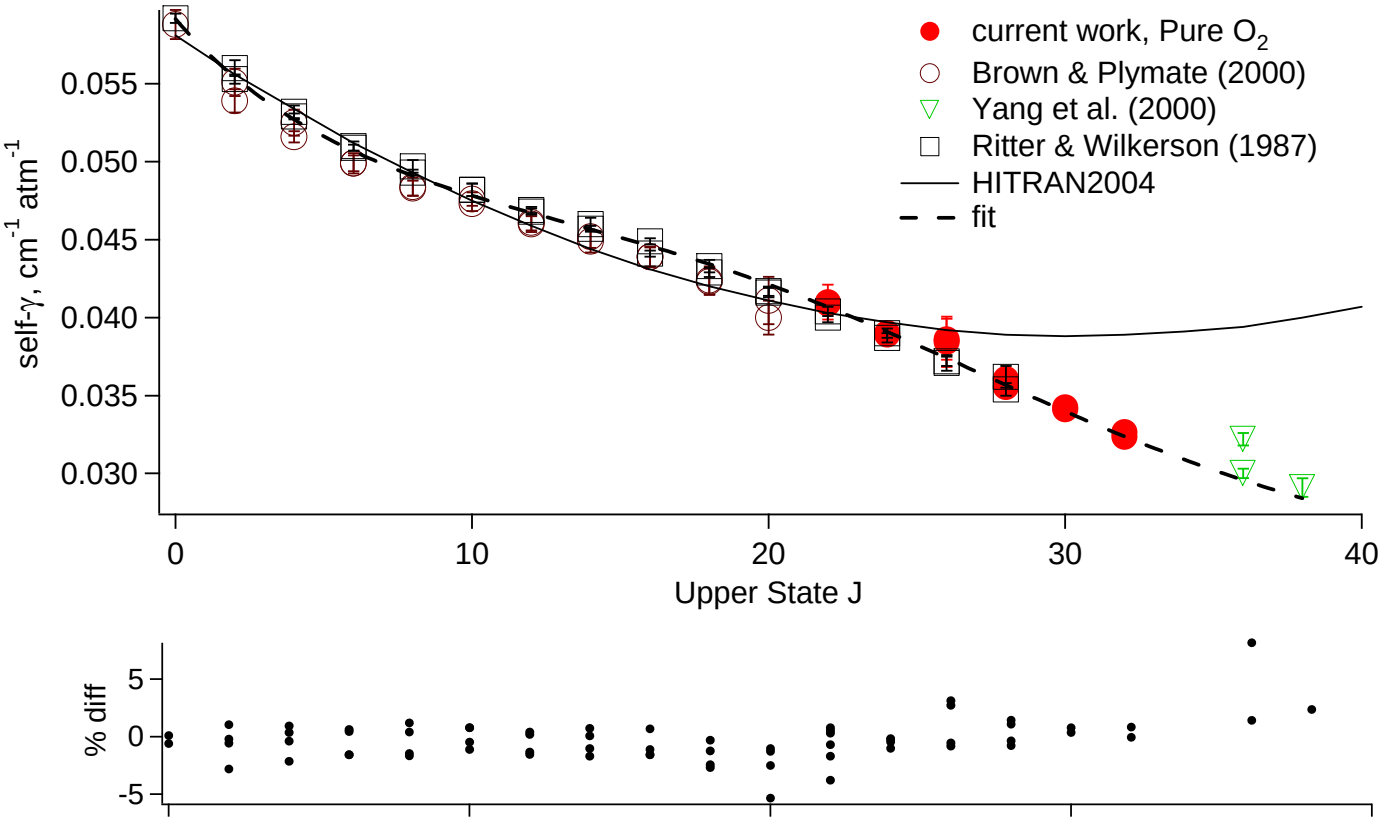

Figure 5.8. Measured self-broadening parameters as a function of upper state *J* for the oxygen *A*-band. Values from Brown and Plymate [12], Yang et al. [30], and Ritter and Wilkerson [13] are also shown. The solid line represents the values used in HITRAN 2004 [28]. The dashed line is a fit to all data based on Eq. 4.2 (see Table 4.6 and text). The bottom panel shows the %difference (obs-calc)/calc of the dashed line fit with a rms of 1.8%. Note the data from Brown and Plymate and Yang et al. were reduced using Voigt lineshapes while the current study and Ritter and Wilkerson used Galatry profiles. Fitting only Galatry widths reduces the rms of the fit to 0.9%.

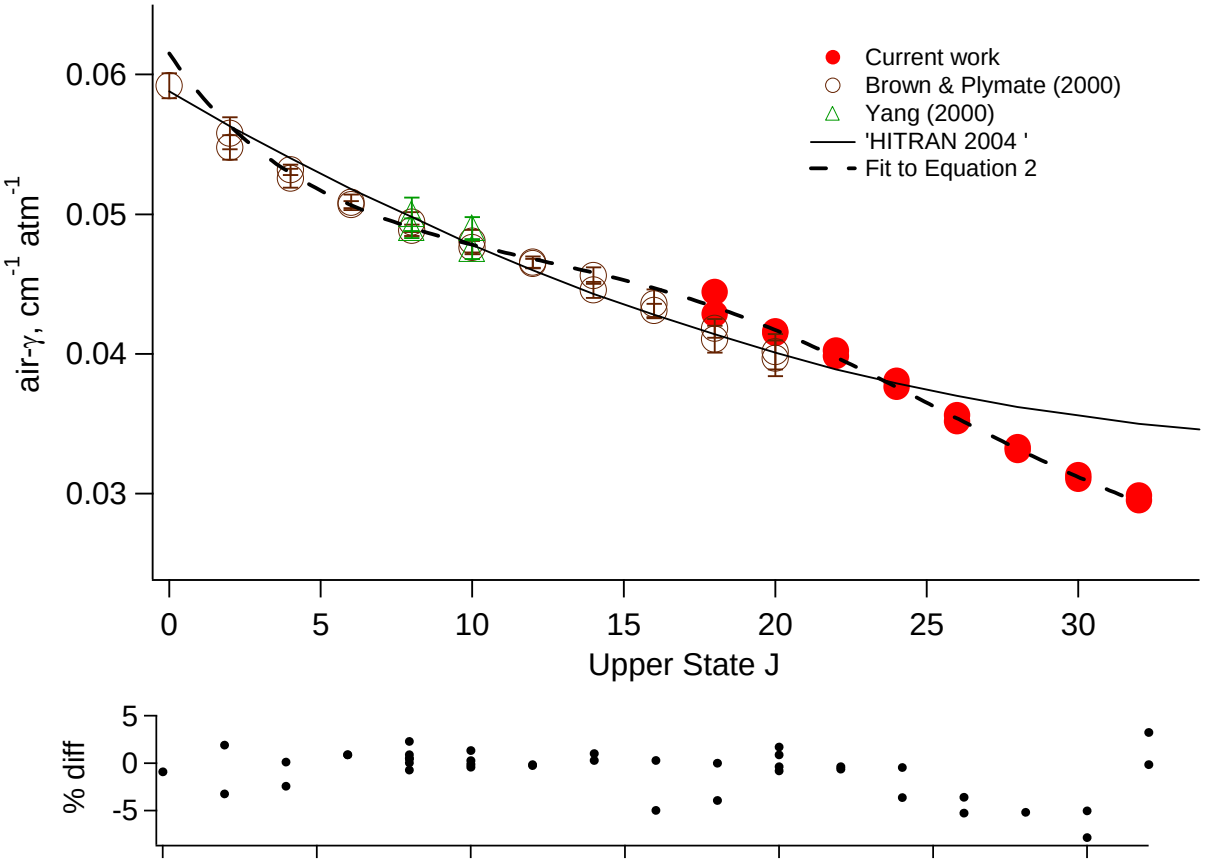

Figure 5.9. Measured air-broadening parameters as a function of upper state *J* for the oxygen *A*-band. Values from Brown and Plymate [12] and Yang et al. [30] are also shown. The solid line represents the values used in HITRAN 2004 [28]. The dashed line is a fit to all the data (see text and Table 6). The bottom panel shows the %difference (obs-calc)/calc of the fit to Eq. 5.2.

The results are presented in Table 5.6. Because the work of Brown and Plymate and Yang et al. used Voigt lineshapes while the current study and that of Ritter and Wilkerson used Galatry lineshapes, we also performed a fit of Eq. (5.2) using only the Galatry-derived widths. Similarly, a comparison of the air-broadening parameters using the data from the current study and Brown and Plymate is shown in Fig. 5.9. The discrepancy between the two datasets at J = 18, 20 is believed to be the result of lineshape effects (Galatry derived widths are known to be larger than Voigt widths). The results of fitting Eq. (5.2) to the data in Fig. 5.9 are shown in Table 5.6 as well as for fits to the data of Brown and Plymate and the current work, respectively.

Table 5.6. Coefficients used to fit air- and self-broadened widths

	A	B	c_1	c_2	c_3	% rms
Self widths						
From Yang(2005) [10]	0.02204	0.03749	0.05428	-1.19×10^{-3}	2.073×10^{-6}	
All data[a]	0.02153	0.03763	0.05870	-1.18×10^{-3}	2.315×10^{-6}	1.8%
Current + Ritter and Wilkerson [14]	0.01824	0.04081	0.04860	-1.29×10^{-3}	1.577×10^{-6}	0.9%
Air widths						
All data[b]	0.02034	0.04113	0.07806	-3.27×10^{-3}	4.184×10^{-6}	2.2%
Current data set	0.02211	0.02202	0.02816	-2.41×10^{-3}	3.417×10^{-6}	1.4%
Brown and Plymate [13]	0.02162	0.03760	0.05882	-1.92×10^{-3}	4.222×10^{-6}	0.7%

[a] Includes the current work, Brown and Plymate [13], Ritter and Wilkerson [14], and Yang et al. [21].
[b] Includes the current work, Brown and Plymate [13], and Yang et al. [21].

In the soft-collision limit, the lineshape is a Galatry profile, and the narrowing halfwidth γ_n is independent of J and given by αp. Here, p is the pressure of the collision partner, and α is the Dicke narrowing coefficient $\alpha = \beta/\omega_D$, where ω_D is the Doppler width, and β is the frictional force constant [49]. The frictional force constant is

inversely related to the mass diffusion coefficient, D, by $\beta = k_B T/mD$, where m, T, and k_B are the mass of the absorber, temperature, and Boltzmann's constant, respectively. Based on the O_2 mass diffusion coefficient of 0.2 cm^2/s [50], the Dicke narrowing coefficient should be ~0.02 cm^{-1} atm^{-1}. Measured values of α in NIST standard air are shown in Fig. 5.10. Although our narrowing coefficients are similar in magnitude to the calculated value, they display a J-dependence as well as a difference between the *PP* and *PQ* transitions; the *PQ* transitions are consistently less than the *PP* transitions of the same J'. Additionally, the narrowing coefficients shown in Fig. 5.10 are based on linear fits to narrowing width vs. number density similar to that shown in Fig. 5.3. However, data taken at $p > 600$ Torr exhibit nonlinearities in the narrowing width vs. density plots. If these high pressure data are excluded, the ratio of *PP*/*PQ* narrowing coefficients is consistently 1.11(±0.02)% over the range studied. We speculate that the nonlinear dependence of γ_n on p, the dependence of α on J, and the difference in α between *PP* and *PQ* transitions may be caused by the variable contribution of line narrowing mechanisms arising from speed-dependent effects, correlations between velocity- and phase-changing collisions, and line-mixing [37, 49, 51-55]. Even if these effects are properly treated, the observed Dicke narrowing coefficient will not necessarily equal the value derived using the mass diffusion coefficient (0.02 cm^{-1} atm^{-1}), because the collisional models (soft- or hard-) used to derive semi-classical line shape expressions are not realistic. More sophisticated lineshape models [55-58] need to be considered to simulate the O_2 *A*-band spectra within their experimental uncertainty, despite the fact that the simple Galatry line shape appears to reproduce the experimental line intensities to better than 0.1%.

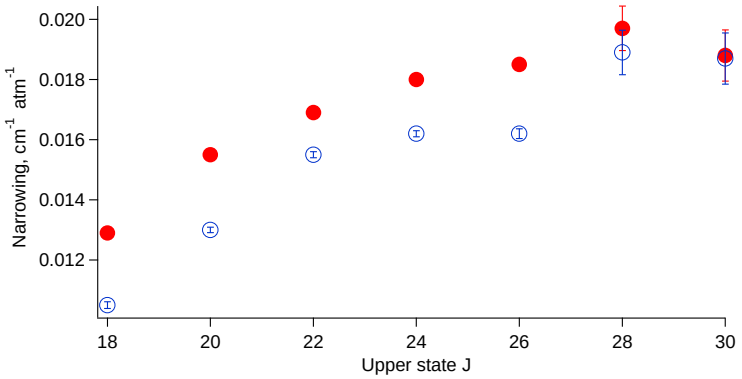

Figure 5.10. Collisional narrowing coefficient vs upper J' for NIST standard air at 296 K. Closed circles: *PP*, open circles: *PQ* transitions. *PP* transitions are consistently larger than *PQ* transitions for the same J'. If results above 600 Torr are excluded the ratio of *PP*/*PQ* transitions is 1.11(± 0.02)% over the range studied (see text).

Evidence of collisional narrowing has been seen in previous *A*-band studies [13-15, 59]; however, only two of these studies report collisional narrowing values. Ritter and Wilkerson [14] measured the narrowing parameter for numerous transitions ($J < 20$) at pressures ranging from 0.05 to 1 atm. Given the relatively large scatter in their data and their assumptions of the soft collision model (Galatry line shape), they reported a single value, $\alpha = 0.0145$ cm^{-1} atm^{-1}, which is consistent with our values for a different J range. Ray and Ghosh [59] measured narrowing coefficients for 4 transitions in the *R*-branch using 2*f* frequency modulation spectroscopy at 300 K, reporting a value of α for each transition. Their values are significantly larger (0.030 cm^{-1} atm^{-1} and 0.020 cm^{-1} atm^{-1} for $J' = 24$ and 20, respectively) than those obtained in this study and that measured by Ritter and Wilkerson. In addition, their pressure-broadening coefficients are up to 50% larger than those obtained by Ritter and Wilkerson and Brown and Plymate, which raises questions about the accuracy of the Ray and Ghosh results.

5.5 Conclusions

This study of the oxygen *A*-band has been carried out using frequency-stabilized cavity ring-down spectroscopy (FS-CRDS) to measure lineshape parameters (line strengths, widths, pressure-induced shifts, and collisional narrowing) for the $18 \leq J' \leq 32$ of the P-branch. The FS-CRDS technique allows us to record highly precise spectra without the influence of confounding instrumental functions. Spectroscopic parameters were determined using the Galatry lineshape. The Galatry profile was used in this study, not only for the better fit quality, resulting in a more accurate measure of the line intensity, but because it gives collisional broadening parameters that are more linear with pressure than Voigt-based values. Thus it is simply not possible to achieve sub-percent level accuracy using a standard Voigt profile. Although our spectra show clear evidence of speed dependence, such effects were not taken into account at this time, as they should account for < 0.2% of the line intensity. A more detailed study of lineshape effects on the transitions in the O_2 *A*-band is described in Chapter 3.

Measured line intensities agree well with previous studies of the O_2 *A*-band [13, 15, 21, 24]. Air- and self-broadened widths have shown a clear deviation from values used in HITRAN 2004 [11], which are based on a extrapolation of the Brown and Plymate dataset [13]. A new empirical function fitting all the data from this study, Brown and Plymate, Ritter and Wilkerson [14], and Yang et al. [21] has been generated, and it is recommended that this new function be utilized in the future. Finally, this is the first study that has reported collisional narrowing coefficients for the *PP* and *PQ*-type transitions as a function of the upper state rotational quantum number. It is clear that it is

not constant for all J, although this may be an artifact of not taking full account of other lineshape effects (speed dependence and/or line-mixing). The uncertainty in absolute line positions was unfortunately limited to 0.002 cm^{-1} by the wavelength meter used in this study. However, relative positions had a relatively high precision of 2×10^{-4} cm^{-1} and were in good agreement with the HITRAN 2004 values. Our pressure-shifting results lie in the middle of the previously reported values. It appears that the discrepancies between the previous studies is linked to the calibration of the frequency axes; the current study is relatively independent of such effects and should be more representative of the true shifting values. However, even with the self-shifts resolved, it is still unclear why Ritter [36] and Phillips and Hamilton [26] observe a significant (0.005 cm^{-1} atm^{-1}) change between self- and air-shifts.

We expect that the new values of the line parameters reported here will be utilized to improve the precision and accuracy of retrieval codes for upcoming remote sensing missions.

Acknowledgements

Part of the research described in this paper was performed at the Jet Propulsion Laboratory, California Institute of Technology, under contract with the National Aeronautics and Space Administration (NASA). Additional support was provided by the Orbiting Carbon Observatory (OCO) project, a NASA Earth System Science Pathfinder (ESSP) mission; the NASA Upper Atmospheric Research Program grant NNG06GD88G; and the NIST Office of Microelectronics Program.

References

[1] P. Drossart, Comp. Rend. Phys. 6 (2005) 817-824.

[2] L.C. O'Brien, H. Cao, J.J. O'Brien, J. Mol. Spectrosc. 207 (2001) 99-103.

[3] D.M. O'Brien, S.A. English, G. DaCosta, J. Atmos. and Ocean. Tech. 14 (1997) 105-119.

[4] K. Chance, J. Quant. Spectrosc. Radiat. Transfer 58 (1997) 375-378.

[5] S. Corradini, M. Cervino, J. Quant. Spectrosc. Radiat. Transfer 97 (2006) 354-380.

[6] B. van Diedenhoven, O.P. Hasekamp, I. Aben, Atmos. Chem. Phys. 5 (2005) 2109-2120.

[7] D.M. O'Brien, R.M. Mitchell, S.A. English, G.A. Da Costa, J. Atmos. and Ocean. Tech. 15 (1998) 1272-1286.

[8] A.K. Heidinger, G.L. Stephens, J. Atmos. Sci. 57 (2000) 1615-1634.

[9] G.L. Stephens, A. Heidinger, J. Atmos. Sci. 57 (2000) 1599-1614.

[10] Z. Yang, P.O. Wennberg, R.P. Cageao, T.J. Pongetti, G.C. Toon, S.P. Sander, J. Quant. Spectrosc. Radiat. Transfer 90 (2005) 309-321.

[11] L.S. Rothman, D. Jacquemart, A. Barbe, D.C. Benner, M. Birk, L.R. Brown, M.R. Carleer, C. Chackerian, K. Chance, L.H. Coudert, V. Dana, V.M. Devi, J.M. Flaud, R.R. Gamache, A. Goldman, J.M. Hartmann, K.W. Jucks, A.G. Maki, J.Y. Mandin, S.T. Massie, J. Orphal, A. Perrin, C.P. Rinsland, M.A.H. Smith, J. Tennyson, R.N. Tolchenov, R.A. Toth, J. Vander Auwera, P. Varanasi, G. Wagner, J. Quant. Spectrosc. Radiat. Transfer 96 (2005) 139-204.

[12] V.G. Avetisov, P. Kauranen, Appl. Opt. 35 (1996) 4705-4723.

[13] L.R. Brown, C. Plymate, J. Mol. Spectrosc. 199 (2000) 166-179.

[14] K.J. Ritter, T.D. Wilkerson, J. Mol. Spectrosc. 121 (1987) 1-19.

[15] B. Anderson, R.J. Brecha, Appl. Phys. B (2007) 379-385.

[16] H. Tran, C. Boulet, J.M. Hartmann, J. Geophys. Res., [Atmos.] 111 (2006).

[17] G. Di Stefano, Chem. Phys. 302 (2004) 243-249.

[18] G. Di Stefano, Chem. Phys. Lett. 426 (2006) 33-38.

[19] R.S. Pope, P.J. Wolf, G.P. Perram, J. Quant. Spectrosc. Radiat. Transfer 64 (2000) 363-377.

[20] C. Hill, D.A. Newnham, J.M. Brown, J. Mol. Spectrosc. 219 (2003) 65-69.

[21] S.F. Yang, M.R. Canagaratna, S.K. Witonsky, S.L. Coy, J.I. Steinfeld, R.W. Field, A.A. Kachanov, J. Mol. Spectrosc. 201 (2000) 188-197.

[22] S.L. Cheah, Y.P. Lee, J.F. Ogilvie, J. Quant. Spectrosc. Radiat. Transfer 64 (2000) 467-482.

[23] S. Xu, D. Dia, J. Xie, G. Sha, G. Zhang, Chem. Phys. Lett. 303 (1999) 171-175.

[24] R. Schermaul, R.C.M. Learner, J. Quant. Spectrosc. Radiat. Transfer 61 (1999) 781-794.

[25] R.D. van Zee, J.T. Hodges, J.P. Looney, Appl. Opt. 38 (1999) 3951-3960.

[26] A.J. Phillips, P.A. Hamilton, J. Mol. Spectrosc. 174 (1995) 587-594.

[27] H. Kanamori, M. Momona, K. Sakurai, Can. J. Phys. 68 (1990) 313-316.

[28] D. Crisp, R.M. Atlas, F.M. Breon, L.R. Brown, J.P. Burrows, P. Ciais, B.J. Connor, S.C. Doney, I.Y. Fung, D.J. Jacob, C.E. Miller, D. O'Brien, S. Pawson, J.T. Randerson, P. Rayner, R.J. Salawitch, S.P. Sander, B. Sen, G.L. Stephens, P.P. Tans, G.C. Toon, P.O. Wennberg, S.C. Wofsy, Y.L. Yung, Z. Kuang, B.

Chudasama, G. Sprague, B. Weiss, R. Pollock, D. Kenyon, S. Schroll, in: *Trace Constituents in the Troposphere and Lower Stratosphere*, 2004; Vol. 34, pp 700-709.

[29] C.E. Miller, L.R. Brown, R.A. Toth, D.C. Benner, V.M. Devi, Comp. Rend. Phys. 6 (2005) 876-887.

[30] C.E. Miller, D. Crisp, P.L. DeCola, S.C. Olsen, J.T. Randerson, A.M. Michalak, A. Alkhaled, P. Rayner, D.J. Jacob, P. Suntharalingam, D.B.A. Jones, A.S. Denning, M.E. Nicholls, S.C. Doney, S. Pawson, H. Boesch, B.J. Connor, I.Y. Fung, D. O'Brien, R.J. Salawitch, S.P. Sander, B. Sen, P. Tans, G.C. Toon, P.O. Wennberg, S.C. Wofsy, Y.L. Yung, R.M. Law, J. Geophys. Res. 112 (2007) D10314, doi:10.1029/2006JD007659.

[31] J.T. Hodges, R. Ciurylo, Rev. Sci. Instrum. 76 (2005) 023112.

[32] J.T. Hodges, H.P. Layer, W.W. Miller, G.E. Scace, Rev. Sci. Instrum. 75 (2004) 849-863.

[33] J.T. Hodges, D. Lisak, Appl. Phys. B 85 (2006) 375-382.

[34] D. Lisak, J.T. Hodges, R. Ciurylo, Phys. Rev. A 73 (2006) 012507.

[35] D. Lisak, J.T. Hodges, Appl. Phys. B (2007) doi:10.1007/s00340-007-2691-x.

[36] K.J. Ritter. A High-Resolution Spectroscopic Study of Absorption Line Profiles in the A-band of Molecular Oxygen. University of Maryland, 1986.

[37] J.W. Brault, L.R. Brown, C. Chackerian, R. Freedman, A. Predoi-Cross, A.S. Pine, J. Mol. Spectrosc. 222 (2003) 220-239.

[38] D. Halmer, G. von Basum, P. Hering, M. Murtz, Rev. Sci. Instrum. 75 (2004) 2187-2191.

[39] L. Galatry, Phys. Rev. 122 (1961) 1218-1223.

[40] D.J. Robichaud, J.T. Hodges, D. Lisak, C.E. Miller, M. Okumura, J. Quant. Spectrosc. Radiat. Transfer (2007) doi:10.1016/j.physletb.2003.10.071.

[41] H.D. Babcock, L. Herzberg, Astrophys. J. 108 (1948) 167-190.

[42] T.G. Adiks, V. Dianovkl, Opt. Spect.-USSR 30 (1971) 110-111.

[43] T.G. Adiks, V. Dianovkl, Opt. Spektrosk. 32 (1972) 432-435.

[44] V.D. Galkin, Opt. Spektrosk. 35 (1973) 630-633.

[45] C. Hill, J.M. Brown, D.A. Newnham, J. Mol. Spectrosc. 221 (2003) 286-287.

[46] A. Predoi-Cross, K. Hambrook, R. Keller, D. Hurtmans, C. Povey, G.C. Mellau, J. Mol. Spectrosc. (2007).

[47] L.S. Rothman, C.P. Rinsland, A. Goldman, S.T. Massie, D.P. Edwards, J.M. Flaud, A. Perrin, C. Camy-Peyret, V. Dana, J.Y. Mandin, J. Schroeder, A. McCann, R.R. Gamache, R.B. Wattson, K. Yoshino, K.V. Chance, K.W. Jucks, L.R. Brown, V. Nemtchinov, P. Varanasi, J. Quant. Spectrosc. Radiat. Transfer 60 (1998) 665-710.

[48] R.R. Gamache, A. Goldman, L.S. Rothman, J. Quant. Spectrosc. Radiat. Transfer 59 (1998) 495-509.

[49] P. Duggan, P.M. Sinclair, R. Berman, A.D. May, J.R. Drummond, J. Mol. Spectrosc. 186 (1997) 90-98.

[50] D.R. Lide, *CRC Handbook of Chemistry and Physics, 71st Edition*. CRC Press: 1990; p 6-151.

[51] D. Lisak, A. Bielski, R. Ciurylo, J. Domyslawska, R.S. Trawinski, J. Szudy, J. Phys. B: At., Mol. Opt. Phys. 36 (2003) 3985-3998.

[52] D. Lisak, G. Rusciano, A. Sasso, J. Mol. Spectrosc. 227 (2004) 162-171.

[53] A.S. Pine, J. Chem. Phys. 101 (1994) 3444-3452.

[54] A.S. Pine, J. Quant. Spectrosc. Radiat. Transfer 62 (1999) 397-423.

[55] R. Wehr, A. Vitcu, R. Ciurylo, F. Thibault, J.R. Drummond, A.D. May, Phys. Rev. A 66 (2002).

[56] A.S. Pine, R. Ciurylo, J. Mol. Spectrosc. 208 (2001) 180-187.

[57] R. Wehr, R. Ciurylo, A. Vitcu, F. Thibault, J.R. Drummond, A.D. May, J. Mol. Spectrosc. to be published.

[58] R. Ciurylo, A. Bielski, J.R. Drummond, D. Lisak, A.D. May, A.S. Pine, D.A. Shapiro, J. Szudy, R.S. Trawinski, in: C. A. Back, (Ed.) AIP: Melville, NY, 2002; p 151.

[59] B. Ray, P.N. Ghosh, Spectrochim. Acta, Part A 53 (1997) 537-543.

CHAPTER 6

Experimental Line Parameters of the $b^1\Sigma_g^+ \leftarrow X^3\Sigma_g^-$ Band of Oxygen Isotopologues Using Frequency-Stabilized Cavity Ring-Down Spectroscopy

This chapter was submitted for publication as:

D.J. Robichaud, J.T. Hodges, L.R. Brown, D. Lisak, P. Maslowski, M. Okumura, C.E. Miller, "Experimental Line Parameters of the Oxygen *A*-Band Using Frequency-Stabilized Cavity Ring-Down Spectroscopy," J. Mol. Spectrosc. (2007) submitted.

6.1 Abstract

The $b^1\Sigma_g^+ \leftarrow X^3\Sigma_g^-$ (0,0) band of the $^{16}O^{18}O$, $^{16}O^{17}O$, $^{17}O^{18}O$, and $^{18}O^{18}O$ isotopologues of oxygen were investigated using frequency-stabilized cavity ring-down spectroscopy. Positions, intensities, pressure-broadened widths, and collisional narrowing coefficients were measured. Absolute positions of 156 lines are presented with < 0.0003 cm^{-1} uncertainty, and re-determination of the excited $b^1\Sigma_g^+$ state molecular constants are presented. Line intensities of the $^{16}O^{18}O$ isotopologue are within 2% of the values currently assumed in molecular databases. However, the line intensities of the $^{16}O^{17}O$ isotopologue show a systematic offset between our results and the databases. Pressure broadening width parameters for the various isotopologues are consistent to within 2%.

6.2 Introduction

The oxygen *A*-band, $b^1\Sigma_g^+ \leftarrow X^3\Sigma_g^-(0,0)$, is the most prominent near-infrared feature in the Earth's atmosphere. It has been used extensively since the 1960's to determine cloud top heights, cloud optical properties, and aerosol optical thickness [1]. Such studies have been extended to the *A*-band spectra from the GOME [2] and SCIAMACHY [3, 4] satellite instruments. Minor isotopologue bands, particularly $^{16}O^{18}O$ and $^{16}O^{17}O$, significantly overlap with the $^{16}O_2$ *A*-band and can bias retrievals unless they are accurately accounted for [5]. The current edition of HITRAN [6] reports line positions based on the 1948 study by Babcock and Herzberg [7] for $^{16}O^{18}O$ and assumes intensities and shape parameters to be equivalent to the corresponding $^{16}O_2$ band. The $^{16}O^{17}O$ band has been updated using the balloon spectra of Camy-Peyret [8].

Since the original work by Babcock and Herzberg [7] in 1948 on the $^{16}O_2$, $^{16}O^{17}O$, and $^{16}O^{18}O$ isotopologues, there have been a surprisingly limited number of studies of the O_2 isotopologues of the $b^1\Sigma_g^+ \leftarrow X^3\Sigma_g^-(0,0)$ band [7-12] (Table 6.1). Most of the recent work has been motivated by tests for violations of the symmetrization postulate of quantum mechanics. Gagliardi and coworkers [10] were the first to investigate the $b^1\Sigma_g^+ \leftarrow X^3\Sigma_g^-(0,0)$ spectrum of $^{18}O_2$. They used FM-diode laser spectroscopy up to J''= 13 to measure line positions with uncertainties of 0.0001 cm^{-1}. Nearly simultaneously, Naus et al. [11] used cavity ring-down spectroscopy to study the line positions of all six isotopologues with 0.03 cm^{-1} accuracy. Schermaul [12] studied the intensities, line positions, and pressure-broadening widths of the $^{16}O^{18}O$ isotopologue using a "collisionally narrowed Voigt profile." Camy-Peyret et al. [8] used atmospheric balloon

Table 6.1. Summary of isotopologue studies of the O_2 $b^1\Sigma_g^+ \leftarrow X^3\Sigma_g^-$ (0, 0) band

Study	Year	Technique	Isotopologues	# lines
Current study	2007	FS-CRDS	$^{16}O^{17}O$, $^{16}O^{18}O$, $^{17}O^{18}O$, $^{18}O_2$	156
van Leeuwen and Wilson [9]	2004	NICE-OHMS	$^{16}O^{18}O$	17
Camy-Peyret [8]	2000	Balloon	$^{16}O^{17}O$, $^{16}O^{18}O$	
Schermaul [12]	1999	FTS	$^{16}O^{18}O$	71
Naus et al. [11]	1997	CRDS	$^{16}O^{17}O$, $^{16}O^{18}O$, $^{17}O^{18}O$, $^{18}O_2$, $^{17}O_2$	340
Gagliardi et al. [10]	1997	FM-diode	$^{18}O_2$	15
Babcock and Herzberg [7]	1948	Atmos. Inter.	$^{16}O^{17}O$, $^{16}O^{18}O$	119

FS-CRDS: frequency stabilized cavity ringdown spectroscopy; Balloon: atmospheric FTS balloon instrument; FTS: Fourier transform spectroscopy; FM-diode: frequency modulation-diode laser spectroscopy; FTS: Fourier-transform spectroscopy; CRDS: cavity ring down spectroscopy; Atmos. Inter.: atmospheric spectra using interferometry.

spectra to determine positions and intensities for the $^{16}O^{17}O$ isotopologue. Finally, van Leeuwen et al. [9] studied the intensities and positions of seventeen high-J $^{16}O^{18}O$ transitions using Noise Immune Cavity Enhanced-Optical Heterodyne Optical Spectroscopy (NICE-OHMS). To our knowledge, there have been no comprehensive studies of the line intensities or shapes for the $^{17}O^{18}O$ or $^{18}O_2$ isotopologues of the $b^1\Sigma_g^+ \leftarrow X^3\Sigma_g^-$ (0,0) band of O_2.

This paper extends our previous work on the $^{16}O_2$ *A*-band [13-15] to the $^{16}O^{17}O$, $^{16}O^{18}O$, $^{17}O^{18}O$, and $^{18}O_2$ isotopologues using frequency stabilized cavity ring-down spectroscopy. The $^{17}O_2$ isotopologue, although present in our spectra, was too weak to study. We present transition frequencies, intensities, and shape parameters for each of the isotopologues. These results are compared to and incorporated with previous measurements where available.

6.3 Experimental Apparatus

The frequency-stabilized cavity ring-down spectrometer (FS-CRDS) located at the National Institute of Standards and Technology (NIST), Gaithersburg, MD has been described in detail previously [13-20]. The ring-down cavity mirrors used in this study had nominal transmission losses of 200 ppm (finesse ~ 15,000) centered at 13,050 cm^{-1}, and the cavity length was nominally 74 cm. The system noise-equivalent absorption coefficient was approximately 6×10^{-10} cm^{-1} $Hz^{-1/2}$. Ring-down decays, having typical decay times of 4–12 μs, were measured using an 8 MHz Si-PIN photodetector and fit using the algorithm of Halmer et al. [21] It was determined that ring-down decay times less than 4 μs suffered from nonlinear effects in the absorption signal due to the bandwidth of the photodetector. This therefore limited the high end of the pressure range used for individual transitions. Total pressures below 1 Torr were avoided to minimize the influence of pressure gauge uncertainties in our intensity measurements.

Spectra of the O_2 isotopologues were recorded using an ^{18}O-enriched sample (Table 6.3). The temperature was measured using a NIST-calibrated 2.4 kΩ thermistor in thermal contact with the outer wall of the cell. Temperatures ranged from 295-298 K and no effort was used to stabilize or control the temperature of the cell. Typically, during the course of a single day the temperature varied by less than 1.5 K. Gas pressure was measured with two NIST-calibrated capacitance diaphragm gauges having full scale responses of 100 and 1000 Torr, respectively, and readout accuracies of < 0.01%.

Table 6.2. Experimental Conditions

All scans
Finesse: 15,000
L_{eff}: 3,500 km
Resolution: <0.0001 cm^{-1}
All scans using enriched ^{18}O sample (see Table 6.3 for composition)

Datasets A-D		Datasets E-O
Step size: 202 MHz (0.00674 cm^{-1})		Step size: 50 MHz (0.00167 cm^{-1})
Typical scan time: 1 day		Scan range: 8-12 GHz, centered on $^{16}O^{18}O$ spectral line
A: 1.004 Torr, 296.0 K	12,975 – 13,115 cm^{-1}	Typical scan time: 10 minutes
B: 9.965 Torr, 295.4 K	12,975 – 13,078 cm^{-1}	
C: 24.61 Torr, 294.0 K	12,975 – 13,076 cm^{-1}	Conditions:
D: 59.85 Torr, 295.8 K	12,975 – 13,086 cm^{-1}	E: 750.2 Torr, 296.0 K
		F: 450.2 Torr, 296.3 K
		G: 298.7 Torr, 296.8 K
		H: 145.2 Torr, 296.6 K
		I: 100.3 Torr, 296.4 K
		J: 69.12 Torr, 296.3 K
		K: 39.55 Torr, 296.4 K
		L: 15.60 Torr, 296.4 K
		M: 8.91 Torr, 296.1 K
		N: 5.10 Torr, 296.2 K
		O: 2.43 Torr, 296.3 K

Spectral scans from 12,975 cm^{-1} – 13,110 cm^{-1} (Fig. 6.1) were recorded with a nominal step size of 202 MHz (0.00674 cm^{-1}, the cavity free-spectral range, FSR). Absolute line positions were referenced against the hyperfine components of the ^{39}K D_1 ($4s\ ^2S_{1/2} \rightarrow 4p\ ^2P_{1/2}$) and D_2 ($4s\ ^2S_{1/2} \rightarrow 4p\ ^2P_{3/2}$) transitions as described previously for the $^{16}O_2$ *A*-band transitions [15]. Due to its importance in atmospheric retrievals, 10 GHz-wide micro-windows centered on selected $^{16}O^{18}O$ transitions were re-scanned at a finer stepsize (50 MHz) to improve the precision on retrieved intensities and shape parameters. Note the Doppler full width half maximum (FWHM) of $^{16}O^{18}O$ in this spectral region is ~830 MHz (0.0275 cm^{-1}) at 296 K. To conserve the enriched gas sample, the cell was charged once to 760 Torr and then successively evacuated to achieve

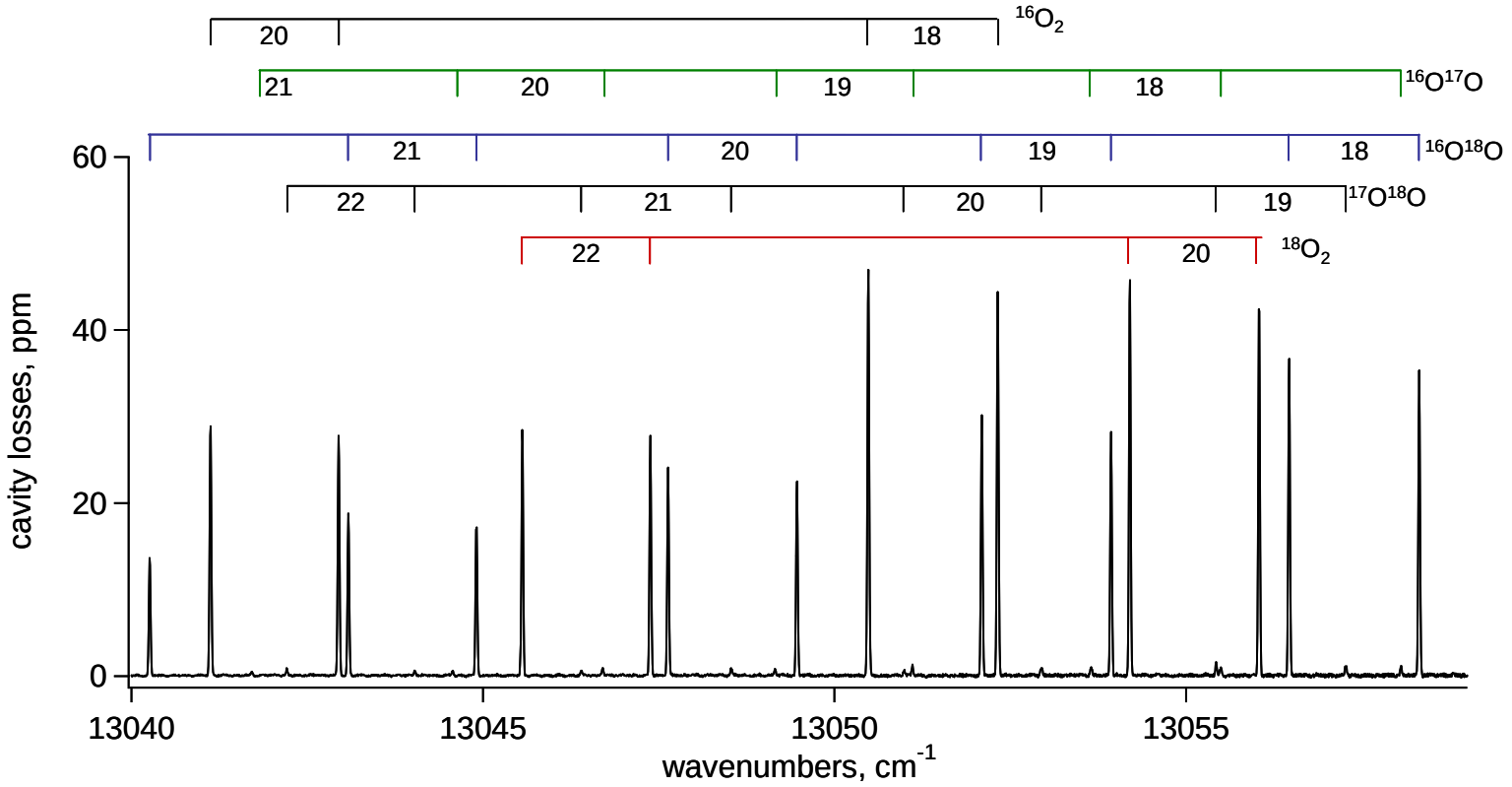

Figure 6.1. Recorded absorption spectrum of the *PP* and *PQ* branches of the O_2 *A*-band with empty cavity losses and Rayleigh scattering subtracted. Sample pressure is 1.004 Torr ^{18}O enriched gas at 296.0 K (Dataset A). Isotopologue assignments shown at top, where upper state *J* is listed between *PP* (left) and *PQ* (right) lines.

lower pressures. All recorded transitions were fit using a Galatry [22] lineshape, which is based on the soft-collision model and generalizes the Voigt profile for Dicke narrowing effects. Line intensities, pressure-induced broadening, and collisional narrowing coefficients were relaxed and determined from best fits of Galatry profiles to the data. All of the scans recorded for pressures > 40 Torr exhibited the asymmetric residuals characteristic of speed-dependent lineshape effects. Preliminary analyses indicated that errors from neglecting speed dependence were less than 0.1%. A detailed study of speed-dependent effects in the oxygen *A*-band will be the subject of a future study.

6.4 Results and Discussion

The $b^1\Sigma_g^+ \leftarrow X^3\Sigma_g^-$ band is electronic dipole forbidden by both spin and orbital angular momentum selection rules, but is allowed through its magnetic dipole [7]. The rotational levels of the O_2 states are described by the angular momentum quantum numbers N and J, where N is the rotational angular momentum, S is the spin angular momentum, and J is the total angular momentum, $J = N + S$. The $^3\Sigma_g^-$ ground state is split into three levels, $J'' = N''-1$, N'', and $N''+1$, whereas the $b^1\Sigma_g^+$ upper state has only levels $J' = N'$. For the symmetric isotopologues with nuclear spin of zero, $^{16}O_2$ and $^{18}O_2$, only the odd levels of N in the ground electronic state and the even levels in the excited state are allowed due to spin statistics. All rotational states are allowed for the asymmetric isotopologues (e.g. $^{16}O^{17}O$, $^{16}O^{18}O$, and $^{17}O^{18}O$). Thus, the $b^1\Sigma_g^+ \leftarrow X^3\Sigma_g^-$ band comprises four types of transitions represented by $\Delta N\ N''\Delta J\ J''$, limited to *PP*, *PQ*, *RQ*, and *RR*. This study focused on the *PP*- and *PQ*-type transitions due to the scanning

range of our laser system. The *PP* and *PQ* transitions are separated by approximately 2 cm^{-1}, forming pairs in the *P* branch.

Due to the importance of obtaining accurate line intensities for the minor isotopologues of O_2 (particularly $^{16}O^{18}O$ and $^{16}O^{17}O$), care was taken in determining the isotopologue abundance in the gas sample (Table 6.3). Unfortunately, the gas supplier of the ^{18}O enriched sample was only able to provide atom percentages, not isotopologue fractions as is needed. We performed our own mass spectral analysis using a JOEL JMS-600H double-focusing magnetic sector mass spectrometer with electron impact ionization. Pure aliquots from each cylinder were introduced into the mass spectrometer with a direct inlet, and mass scans were conducted from m/z = 32-36. Peak intensities were recorded and used as-is for the calculation of isotope abundances. The relative amounts of the five most abundant isotopologues ($^{16}O_2$, $^{16}O^{18}O$, $^{16}O^{17}O$, $^{18}O_2$, and $^{17}O^{18}O$) were calculated directly using normalized peak heights, assuming no contribution of $^{17}O_2$ to the ion signal at the mass spectrometer. We estimate the error due to this assumption to be 0.01%. Use of an isotope ratio mass spectrometer may improve the overall reproducibility of the abundance measurement, though improving the overall accuracy requires a reference gas of nominally similar isotope composition. As an additional check, sixteen of the $^{16}O_2$ and three of the $^{16}O^{18}O$ lines were studied in both the ^{18}O enriched sample and pure O_2 near natural abundance. Using the measured peak areas, a, and knowledge of the natural abundance of the isotopologue, I_n, the abundance in the ^{18}O enriched sample can be determined using the relation $a_n/a_e = I_n/I_e$, where the subscripts n and e refer to the natural abundant and ^{18}O enriched samples, respectively.

Table 6.3. Isotopologue Composition of the ^{18}O enriched Gas Sample

	$^{16}O_2$	$^{16}O^{17}O$	$^{16}O^{18}O$	$^{17}O_2$	$^{17}O^{18}O$	$^{18}O_2$
supplier	0.2098	0.0137	0.4827	0.0002	0.0158	0.2777
Mass Spec	**0.2784 (51)**	**0.0099 (4)**	**0.3672 (18)**		**0.0174 (4)**	**0.3271 (32)**
Ratio of Int.	0.2705 (18)		0.3769 (49)			

The supplier was only able to provide atom percentages (^{16}O = 45.8%, ^{17}O = 1.5%, ^{18}O = 52.7%). Supplier values were calculated assuming a stochastically distributed sample. For the mass spectrometer runs, the $^{16}O^{18}O$ value is actually the sum of the $^{16}O^{18}O$ + $^{17}O_2$ (i.e. mass = 34). Ratio of intensities is the ratio of intensities between a sample near natural abundance and the ^{18}O enriched sample. Values in parenthesis are 1 σ uncertainty of the last digit.

Based on our previous study [13], the reproducibility of the line intensities over several months have uncertainties of ~0.2%.

The transition frequencies, line intensities, pressure broadened widths, and narrowing coefficients for the $^{16}O^{17}O$, $^{16}O^{18}O$, $^{17}O^{18}O$, and $^{18}O_2$ isotopologues recorded in Datasets A–D are presented in Tables 6.4–7. Although the $^{17}O_2$ transitions were observed in our spectra, they were either too weak or obscured by the more dominant isotopologues for a detailed analysis to be performed. The absolute transition frequencies were calibrated using the hyperfine components of ^{39}K *D* lines as described previously [15]. Since accurate pressure shifting parameters are not known for the series of isotopologues, all transition frequencies were corrected for pressure shifting using the pressure shifting parameters for the corresponding $^{16}O_2$ values [13] (for odd values of *J*′ the values were interpolated). This is considered appropriate since the pressure shifting values are not expected to change much with isotope, and the magnitude of the pressure shifts at 1 Torr (~10^{-5} cm^{-1}) is smaller than the reported accuracies.

The transition frequencies for $^{16}O^{17}O$ were in generally good agreement (±0.002 cm^{-1}) with HITRAN 2004 [6], which was based on the atmospheric balloon spectra of

Table 6.4: Measured Line Parameters of the $^{16}O^{17}O$ Isotopologue

Assignment $\Delta N\ N''\ \Delta J\ J''$	Position	unc (10^{-4}cm^{-1})	o-c (10^{-4}cm^{-1})	J'	Intensity $\times 10^{-27}$	γ	α
P3 P3	13115.44246	*		2	2.33 (53)		
P4 Q3	13113.36584	*		3	2.18 (13)		
P4 P4	13110.30544	23	–0.9	3	2.73 (15)		
P5 Q4	13109.16274	9	–9.4	4	2.32 (13)		
P5 P5	13107.15544	11	–0.7	4	3.01 (15)		
P6 Q5	13105.90454	13	4.5	5	2.69 (17)		
P6 P6	13103.91582	*		5	1.17 (47)		
P7 Q6	13102.55938	9	8.5	6	2.68 (14)		
P7 P7	13100.58606	8	–4.5	6	3.43 (16)		
P8 Q7	13099.12544	15	–1.3	7	2.56 (18)		
P8 P8	13097.16837	7	7.2	7	3.37 (16)		
P9 Q8	13095.60489	8	4.3	8	2.93 (15)		
P9 P9	13093.65924	*		8	0.19 (9)		
P10 Q9	13091.99485	10	0.4	9	2.74 (14)		
P10 P10	13090.06084	9	–4.7	9	3.17 (15)		
P11 Q10	13088.27233	9	–7.5	10	0.23 (11)		
P11 P11	13086.37386	*		10	3.12 (15)		
P12 Q11	13084.50908	12	2.6	11	2.48 (10)		
P12 P12	13082.59713	11	2.4	11	2.71 (11)		
P13 Q12	13080.63097	13	–12.0	12	2.31 (9)		
P13 P13	13078.73043	12	0.5	12	2.46 (9)		
P14 Q13	13076.66565	13	–5.9	13	2.035 (82)		
P14 P14	13074.77485	13	5.6	13	2.159 (87)		
P15 Q14	13072.61148	17	5.4	14	1.775 (71)	0.051 (2)	
P15 P15	13070.72681	18	–17.9	14	1.883 (76)	0.050 (2)	
P16 Q15	13068.46843	21	22.5	15	1.543 (62)	0.050 (2)	
P16 P16	13066.59358	17	3.3	15	1.611 (65)	0.046 (2)	
P17 Q16	13064.23222	18	3.8	16	1.286 (52)	0.049 (5)	
P17 P17	13062.36846	14	2.9	16	1.365 (55)	0.053 (3)	
P18 Q17	13059.90827	22	4.3	17	1.071 (43)	0.053 (2)	
P18 P18	13058.05542	22	21.4	17	1.131 (45)	0.050 (2)	
P19 Q18	13055.49331	30	–7.4	18	0.874 (35)	0.052 (2)	
P19 P19	13053.64781	24	–6.9	18	0.921 (37)	0.055 (4)	
P20 Q19	13050.99494	39	45.7	19	0.718 (29)	0.047 (2)	
P20 P20	13049.15299	25	–7.4	19	0.736 (29)	0.048 (3)	
P21 Q20	13046.39702	27	3.6	20	0.544 (22)	0.037 (4)	
P21 P21	13044.56813	27	–7.3	20	0.573 (23)	0.030 (3)	
P22 Q21	13041.70709	38	–57.1	21	0.438 (17)	0.041 (2)	
P22 P22	13039.89286	33	-9.0	21	0.442 (17)	0.047 (4)	
P23 Q22	13036.93749	41	–11.5	22	0.324 (13)	0.034 (4)	
P23 P23	13035.12298	27	–53.2	22	0.343 (13)	0.038 (6)	
P24 Q23	13032.07477	41	7.4	23	0.249 (10)		
P24 P24	13030.27158	31	–7.6	23	0.269 (11)		
P25 Q24	13027.11879	*		24	0.187 (7)		
P25 P25	13025.32571	*		24	0.202 (8)		
P26 Q25	13022.07277	*		25	0.132 (6)		

P26 P26	13020.28825	*	25	0.130 (7)
P27 Q26	13016.93577	*	26	0.095 (6)
P27 P27	13015.15977	*	26	0.107 (8)
P28 Q27	13011.70759	*	27	0.081 (8)
P28 P28	13009.94008	*	27	0.073 (9)
P29 Q28	13006.38804	*	28	0.061 (7)
P29 P29	13004.62898	*	28	0.039 (6)
P30 Q29	13000.97687	*	29	0.034 (9)
P30 P30	12999.22625	*	29	0.030 (9)

Positions in cm^{-1}, transitions denoted with an * are calculated values and not used in the fit to determine the molecular constants. Intensities are in units of cm^{-1}/(molecule cm^{-2}) at T=296 K, adjusted for natural abundance (0.000742). Pressure broadening (γ) and collisional narrowing (α) coefficients are in units of cm^{-1} atm^{-1}. The values in parentheses (1 σ uncertainty of the last digit) are Type A uncertainties and quantify the precision and reproducibility of the measurement. They are based on the quadrature sum of the fitted parameter uncertainties obtained by the Galatry lineshape fits and the standard deviation of repeated measurements. These uncertainties do not account for systematic effects associated with the lineshape model, but do incorporate uncertainty in the isotope abundance as shown in Table 5.3 for the intensities. Combined relative standard uncertainties in S_i associated with the measurement of p, T, composition and spectral frequency axes are estimated to be < 0.2 %. Intensities for $J \leq 13$ are based on Dataset A only. Intensities for $J \geq 23$ are based on Datasets B-D.

Table 6.5: Measured Line Parameters of the $^{16}O^{18}O$ Isotopologue

Assignment $\Delta N\ N''\ \Delta J\ J''$	Position*	unc (10^{-5}cm^{-1})	o-c (10^{-5}cm^{-1})	J'	Intensity $\times 10^{-27}$		γ		α	
P3 P3	13114.57458	*		2	11.081	(56)				
P4 Q3	13113.62672	*		3	9.904	(90)				
P4 P4	13111.59661	*		3	13.157	(66)				
P5 Q4	13110.53305	5	–0.3	4	11.771	(59)				
P5 P5	13108.53136	7	0.2	4	14.755	(73)				
P6 Q5	13107.36492	3	1.2	5	13.171	(66)				
P6 P6	13105.37891	3	–0.9	5	15.902	(79)				
P7 Q6	13104.10978	3	0.1	6	14.072	(70)				
P7 P7	13102.13927	4	–2.2	6	16.586	(82)				
P8 Q7	13100.76953	4	0.6	7	14.559	(72)				
P8 P8	13098.81251	4	–0.4	7	16.796	(83)				
P9 Q8	13097.34351	3	–0.7	8	14.638	(73)				
P9 P9	13095.39862	3	–1.9	8	16.596	(82)				
P10 Q9	13093.83126	3	3.9	9	14.302	(71)				
P10 P10	13091.89770	4	5.3	9	15.991	(79)				
P11 Q10	13090.23265	5	–0.6	10	13.613	(68)				
P11 P11	13088.30924	4	–2.0	10	15.366	(77)				
P12 Q11	13086.54727	4	1.7	11	12.715	(63)				
P12 P12	13084.63442	4	2.4	11	13.988	(69)				
P13 Q12	13082.77522	4	–1.0	12	11.636	(58)				
P13 P13	13080.87217	4	–2.4	12	12.649	(63)				
P14 Q13	13078.91623	5	–5.3	13	10.444	(52)				
P14 P14	13077.02268	5	–5.0	13	11.303	(83)				
P15 Q14	13074.97025	5	–2.1	14	9.253	(53)	0.0468	(8)		
P15 P15	13073.08601	5	2.2	14	9.962	(52)	0.0477	(7)		
P16 Q15	13070.93727	6	–1.5	15	7.968	(41)	0.0468	(11)		
P16 P16	13069.06217	6	–6.0	15	8.585	(43)	0.0468	(4)		
P17 Q16	13066.81709	6	4.8	16	6.820	(33)	0.0454	(3)		
P17 P17	13064.95086	6	–1.2	16	7.266	(35)	0.0478	(12)		
P18 Q17	13062.60969	8	8.3	17	5.702	(28)	0.0453	(4)	0.008	(19)
P18 P18	13060.75228	7	7.6	17	6.062	(29)	0.0443	(4)	0.008	(17)
P19 Q18	13058.31486	8	5.6	18	4.689	(23)	0.0461	(3)	0.003	(13)
P19 P19	13056.46624	7	5.0	18	4.976	(24)	0.0448	(4)	0.006	(15)
P20 Q19	13053.93247	10	–0.8	19	3.801	(18)	0.0436	(4)	0.011	(14)
P20 P20	13052.09249	9	3.7	19	4.016	(19)	0.0441	(4)	0.011	(12)
P21 Q20	13049.46240	10	–2.2	20	3.031	(14)	0.0422	(3)	0.008	(13)
P21 P21	13047.63103	9	14.0	20	3.193	(15)	0.0431	(2)	0.010	(9)
P22 Q21	13044.90461	10	–13.4	21	2.380	(11)	0.0422	(3)	0.010	(9)
P22 P22	13043.08186	10	7.3	21	2.4738	(174)	0.0423	(1)	0.010	(5)
P23 Q22	13040.25880	11	–6.0	22	1.8260	(107)	0.0412	(5)	0.010	(12)
P23 P23	13038.44454	9	–16.6	22	1.9257	(191)	0.0419	(1)	0.012	(5)
P24 Q23	13035.52511	12	6.2	23	1.3923	(71)	0.0410	(1)	0.014	(6)
P24 P24	13033.71893	12	3.6	23	1.4527	(98)	0.0414	(1)	0.014	(9)
P25 Q24	13030.70321	16	–22.4	24	1.0407	(61)	0.0405	(2)	0.015	(6)
P25 P25	13028.90547	18	17.4	24	1.0859	(61)	0.0405	(1)	0.014	(4)
P26 Q25	13025.79249	24	–17.1	25	0.7732	(38)	0.03988	(9)	0.0154	(3)
P26 P26	13024.00348	27	–24.1	25	0.8026	(48)	0.04089	(18)	0.0167	(4)
P27 Q26	13020.79349	42	25.3	26	0.5613	(36)	0.03988	(9)	0.0154	(3)
P27 P27	13019.01229	47	–3.7	26	0.5829	(35)	0.03999	(11)	0.0164	(3)

P28 Q27	13015.70605	68	100.9	27	0.4048	(20)	0.03807	(10)	0.0147	(2)
P28 P28	13013.93287	80	17.3	27	0.4205	(21)	0.03866	(14)	0.0167	(3)
P29 Q28	13010.52992	135	–86.4	28	0.2889	(31)	0.03645	(5)	0.0145	(2)
P29 P29	13008.76441	154	62.2	28	0.2963	(15)	0.03725	(3)	0.0160	(1)
P30 Q29	13005.26189	216	177.1	29	0.1994	(16)	0.03586	(3)	0.0142	(2)
P30 P30	13003.50690	230	148.9	29	0.2038	(43)	0.03532	(15)	0.0133	(4)
P31 Q30	12999.90889	233	372.0	30	0.1387	(18)	0.0355	(68)		
P31 P31	12998.15880	*		30	0.1419	(8)	0.03580	(3)	0.0163	(2)
P32 Q31	12994.46173	*		31	0.0934	(5)	0.03510	(5)	0.0167	(2)
P32 P32	12992.72156	*		31	0.0959	(11)	0.03473	(6)	0.0154	(3)
P33 Q32	12988.92634	*		32	0.0624	(7)	0.03373	(9)	0.0153	(4)
P33 P33	12987.19430	*		32	0.0674	(3)	0.03470	(11)	0.0168	(4)
P34 Q33	12983.30068	*		33	0.0439	(4)	0.03313	(10)	0.0145	(6)
P34 P34	12981.57674	*		33	0.0416	(8)	0.03334	(18)	0.0156	(6)
P35 Q34	12977.58444	*		34	0.0265	(2)	0.03292	(24)	0.0147	(16)
P35 P35	12975.86859	*		34	0.0274	(3)	0.03190	(17)	0.0112	(12)

Positions in cm^{-1}, transitions denoted with an * are calculated values and not used in the fit to determine the molecular constants. Intensities are in units of cm^{-1}/(molecule cm^{-2}) at T=296 K, adjusted for natural abundance (0.00399141). Pressure broadening (γ) and collisional narrowing (α) coefficients are in units of cm^{-1} atm^{-1}. The values in parentheses (1 σ uncertainty of the last digit) and described in Table 6.4. Intensities for $J \leq 13$ are based on Dataset A only. Intensities and shape parameters for $J \geq 24$ are based on Datasets E-O.

Table 6.6: Measured Line Parameters of the $^{17}O^{18}O$ Isotopologue

Assignment $\Delta N\ N''\ \Delta J\ J''$	Position*	unc (10^{-4}cm^{-1})	o-c (10^{-4}cm^{-1})	J'	Intensity $\times 10^{-31}$	γ	α
P4 Q3	13115.09578	*		3	35.6 (14)		
P4 P4	13113.07142	*		3	49.2 (17)		
P5 Q4	13112.10287	*		4	43.0 (16)		
P5 P5	13110.10221	12	2.6	4	54.9 (18)		
P6 Q5	13109.03090	5	–3.6	5	45.4 (16)		
P6 P6	13107.04725	8	–7.8	5	58.3 (18)		
P7 Q6	13105.87826	7	–0.6	6	50.5 (20)		
P7 P7	13103.90898	7	–7.1	6	86.3 (58)		
P8 Q7	13102.64337	5	5.1	7	53.5 (17)		
P8 P8	13100.68743	4	4.5	7	64.5 (19)		
P9 Q8	13099.32387	5	–3.6	8	51.9 (16)		
P9 P9	13097.38069	5	7.9	8	62.2 (18)		
P10 Q9	13095.92232	6	2.3	9	49.4 (16)		
P10 P10	13093.98719	6	–12.9	9	61.5 (18)		
P11 Q10	13092.43607	7	–1.0	10	49.3 (16)		
P11 P11	13090.51352	5	8.1	10	56.9 (17)		
P12 Q11	13088.86679	7	4.5	11	44.7 (15)		
P12 P12	13086.95239	6	–2.0	11	53.1 (16)		
P13 Q12	13085.21272	7	2.6	12	41.7 (14)		
P13 P13	13083.30761	6	–4.7	12	48.1 (11)		
P14 Q13	13081.47398	9	–4.5	13	40.7 (9)		
P14 P14	13079.57947	7	2.9	13	43.2 (10)		
P15 Q14	13077.65057	9	–15.8	14	36.4 (8)		
P15 P15	13075.76519	8	–6.3	14	37.8 (9)		
P16 Q15	13073.74719	11	16.6	15	31.2 (7)		
P16 P16	13071.86801	9	0.4	15	32.9 (8)	0.053 (2)	
P17 Q16	13069.75413	11	–3.6	16	26.5 (6)	0.044 (2)	
P17 P17	13067.88553	11	–0.2	16	27.9 (6)	0.048 (2)	
P18 Q17	13065.67984	15	9.2	17	22.3 (5)	0.051 (3)	
P18 P18	13063.81925	13	7.7	17	23.5 (5)	0.049 (2)	
P19 Q18	13061.51612	17	–25.9	18	18.5 (4)	0.044 (2)	
P19 P19	13059.66677	13	0.8	18	19.3 (4)	0.045 (2)	
P20 Q19	13057.27275	18	–10.2	19	15.3 (4)	0.043 (2)	
P20 P20	13055.42916	14	–9.2	19	15.7 (4)	0.049 (2)	
P21 Q20	13052.94448	19	5.2	20	12.4 (3)	0.045 (2)	
P21 P21	13051.10914	17	6.0	20	12.7 (3)	0.054 (2)	
P22 Q21	13048.53518	22	60.1	21	9.7 (2)	0.051 (3)	
P22 P22	13046.70311	19	11.7	21	10.1 (2)	0.046 (3)	
P23 Q22	13044.02966	26	4.1	22	7.5 (2)	0.048 (2)	
P23 P23	13042.20854	22	–16.5	22	7.9 (2)	0.044 (3)	
P24 Q23	13039.44545	48	13.8	23	5.79 (13)	0.040 (2)	
P24 P24	13037.62971	25	–34.0	23	5.95 (14)	0.048 (3)	
P25 Q24	13034.77346	*		24	4.48 (11)	0.040 (2)	
P25 P25	13032.97056	*		24	4.49 (10)	0.055 (5)	
P26 Q25	13030.01726	*		25	3.46 (8)		
P26 P26	13028.22239	*		25	3.32 (8)		
P27 Q26	13025.17529	*		26	2.52 (7)		
P27 P27	13023.38842	*		26	2.52 (7)		
P28 Q27	13020.24737	*		27	1.89 (8)		

P28 P28	13018.46847	*	27	1.91 (7)
P29 Q28	13015.23330	*	28	1.15 (7)
P29 P29	13013.46234	*	28	1.40 (9)
P30 Q29	13010.13287	*	29	0.78 (10)
P30 P30	13008.36984	*	29	1.08 (9)
P31 Q30	13004.94587	*	30	2.56 (10)
P31 P31	13003.19074	*	30	0.61 (7)

Positions in cm^{-1}, transitions denoted with an * are calculated values and not used in the fit to determine the molecular constants. Intensities are in units of cm^{-1}/(molecule cm^{-2}) at T=296 K, adjusted for natural abundance (1.516×10^{-6}). Pressure broadening (γ) and collisional narrowing (α) coefficients are in units of cm^{-1} atm^{-1}. The values in parentheses (1 σ uncertainty of the last digit) and described in Table 6.4. Intensities for $J \leq 11$ are based on Dataset A only.

Table 6.7: Measured Line Parameters of the $^{18}O_2$ Isotopologue

Assignment $\Delta N\ N''\ \Delta J\ J''$	Position	unc (10^{-5}cm^{-1})	o-c (10^{-5}cm^{-1})	J'	Intensity $\times 10^{-30}$		γ	α
P5 Q4	13113.50532	*		4	23.373	(100)		
P5 P5	13111.50822	*		4	26.587	(18)		
P7 Q6	13107.45947	6	1.3	6	25.818	(16)		
P7 P7	13105.49276	3	6.1	6	30.166	(15)		
P9 Q8	13101.09288	3	–14.8	8	27.082	(16)		
P9 P9	13099.14936	3	2.8	8	30.624	(25)		
P11 Q10	13094.40203	3	0.3	10	25.654	(16)		
P11 P11	13092.47827	3	0.4	10	28.299	(15)		
P13 Q12	13087.38493	3	2.3	12	22.277	(15)		
P13 P13	13085.47950	3	3.0	12	24.218	(15)		
P15 Q14	13080.04082	3	–0.7	14	18.026	(14)		
P15 P15	13078.15275	3	–0.1	14	19.299	(16)		
P17 Q16	13072.36906	4	–1.1	16	13.638	(38)	0.0463 (6)	
P17 P17	13070.49778	3	0.8	16	14.475	(34)	0.0425 (8)	
P19 Q18	13064.36895	5	0.6	18	9.686	(11)	0.0473 (3)	
P19 P19	13062.51401	4	1.4	18	10.217	(8)	0.0423 (6)	
P21 Q20	13056.03963	6	–6.7	20	6.470	(3)	0.0425 (3)	
P21 P21	13054.20068	6	–1.8	20	6.787	(3)	0.0456 (2)	
P23 Q22	13047.38018	7	–5.6	22	4.068	(1)	0.0409 (3)	0.010 (1)
P23 P23	13045.55718	6	1.0	22	4.253	(1)	0.0404 (3)	0.006 (1)
P25 Q24	13038.38972	7	4.1	24	2.414	(1)	0.0401 (6)	0.010 (1)
P25 P25	13036.58230	9	6.6	24	2.513	(1)	0.0400 (3)	0.011 (1)
P27 Q26	13029.06678	10	–5.2	26	1.355	(1)	0.0386 (2)	0.014 (1)
P27 P27	13027.27477	10	10.5	26	1.402	(1)	0.0381 (2)	0.012 (1)
P29 Q28	13019.40991	23	–26.3	28	0.722	(1)	0.0381 (7)	0.016 (2)
P29 P29	13017.63324	25	–1.3	28	0.746	(1)	0.0375 (7)	0.016 (2)
P31 Q30	13009.41764	68	–21.2	30	0.363	(1)	0.0303 (23)	0.008 (5)
P31 P31	13007.65711	75	32.6	30	0.376	(1)	0.0341 (22)	0.012 (5)
P33 Q32	12999.09087	215	134.4	32	0.176	(1)	0.0356 (52)	0.022 (12)
P33 P33	12997.34441	232	202.0	32	0.180	(2)	0.0333 (62)	0.024 (14)
P35 Q34	12988.42071	*		34	0.078	(1)	0.0333 (70)	0.009 (15)
P35 P35	12986.69015	*		34	0.080	(1)	0.0262 (60)	0.002 (13)
P37 Q36	12977.41169	*		36	0.033	(1)	0.0213 (86)	
P37 P37	12975.69630	*		36	0.033	(1)	0.0189 (84)	

Positions in cm^{-1}, transitions denoted with an * are calculated values and not used in the fit to determine the molecular constants. Intensities are in units of cm^{-1}/(molecule cm^{-2}) at T=296 K, adjusted for natural abundance (4.002×10^{-6}). Pressure broadening (γ) and collisional narrowing (α) coefficients are in units of cm^{-1} atm^{-1}. The values in parentheses (1 σ uncertainty of the last digit) and described in Table 6.4. Intensities for $J \leq 14$ are based on Dataset A only.

Camy-Peyret et al. [8]. However, the $^{16}O^{18}O$ transition frequencies were in poor agreement with HITRAN 2004, deviating by 0.01 cm^{-1} at low J to 0.3 cm^{-1} at J = 34. Poor agreement with experimental spectra was also noted by van Leeuwen et al. [9].

For each isotopologue the data were incorporated into a least-squares fitting routine to derive molecular constants. For the $X\,^3\Sigma_g^-(v=0)$ ground state, the Hamiltonian of Rouillé et al. [23] was used, while for the $b^1\Sigma_g^+(v=0)$ excited state we used

$$E = T + BJ(J+1) - DJ^2(J+1)^2 + HJ^3(J+1)^3 \,. \qquad (6.1)$$

Accurate ground state constants have been previously determined for all of the isotopologues involved in this study [23-26] and are reported in Table 6.8. To maintain consistency with the HITRAN database, the ground state energy levels for the symmetric isotopologues ($^{16}O_2$ and $^{18}O_2$) were relative to the N'' = 1, J'' = 0 level, whereas the energy levels of the asymmetric isotopologues ($^{16}O^{17}O$, $^{16}O^{18}O$, and $^{17}O^{18}O$) were relative to the N'' = 0, J'' = 1 level. These ground state molecular constants were held fixed during the fitting routine. The resulting molecular constants for the excited $b^1\Sigma_g^+$ states are presented in Table 6.9 along with the constants determined by previous studies. The band origin for several of the past studies was recalculated so that the ground state zero-level was consistent with that used in the current work. The constants for $^{16}O_2$ were previously reported in Robichaud et al. [15] and are shown for comparison.

Table 6.8. Molecular constants for the $X\,^3\Sigma_g^-(v{=}0)$ ground state of O_2.

	$^{16}O_2$	$^{16}O^{17}O$	$^{16}O^{18}O$	$^{17}O^{18}O$	$^{18}O_2$
B_0	1.437 676 476 (77)	1.395 319 (3)	1.357 852 22 (16)	1.315 490 (3)	1.278 008 47 (23)
D_0	$4.842\,56\,(63)\times10^{-6}$	4.623×10^{-6}	$4.319\,(13)\times10^{-6}$	4.102×10^{-6}	3.835×10^{-6}
H_0	$2.8\,(16)\times10^{-12}$				
λ_0	1.984 751 322 (72)	1.984 709 4 (3)	1.984 674 43 (17)	1.984 632 9 (13)	1.984 596 22 (37)
λ'_0	$1.945\,21\,(50)\times10^{-6}$	$1.917\,(6)\times10^{-6}$	$1.83305\,(9)\times10^{-6}$	$1.801\,(10)\,)\times10^{-6}$	$1.738\,(14)\times10^{-6}$
λ''_0	$1.103\,(41)\times10^{-11}$		$9.84\,(83)\times10^{-12}$		
μ_0	$-8.425\,390\,(13)\times10^{-3}$	$-8.176\,12\,(13)\times10^{-3}$	$-7.955\,998\,(17)\times10^{-3}$	$-7.706\,96\,(23)\times10^{-3}$	$-\ 7.486\,48\,(10)\times10^{-3}$
μ'_0	$-8.106(32)\times10^{-9}$	$-8.0\,(10)\times10^{-9}$	$-7.317\,7(13)\times10^{-9}$	$-9.0\,(20)\times10^{-9}$	$-11.7(18)\times10^{-9}$
μ''_0	$-4.7(19)\times10^{-14}$				
Ref.	Rouillé et al. [23]	Cazolli et al. [24]	Mizushima and Yamamoto [25]	Cazolli et al. [24]	Steinbach and Gordy [26]

All values in cm^{-1}. The value in parentheses represents the uncertainty in the last significant digit. Molecular constants fixed to these values during the fit.

Table 6.9. Molecular constants for the $b^1\Sigma_g^+$ state of molecular oxygen

	T (cm^{-1})	B (cm^{-1})	D ($10^{-6}\,cm^{-1}$)	H ($10^{-12}\,cm^{-1}$)	Ref
$^{16}O_2$	13122.00580 (2)	1.391 249 4 (4)	5.3695 (17)	−2.2 (2)	This work
	13122.00575 (1)	1.391 249 6 (1)	5.3699 (3)	−1.8 (2)	Robichaud et al. [15]
$^{16}O^{17}O$	13123.803 4 (5)	1.350 271 (5)	5.110 (8)		This work
	13123.808 (3)	1.350 232 (15)	5.07 (2)		Naus et al. [11]
	13123.808 (1)	1.350 312 (6)	5.092 (5)		Camy-Peyret [8]
	13123.77 (6)	1.352 0 (1)			Babcock and Herzberg [7]
$^{16}O^{18}O$	13124.793 14 (2)	1.314 044 0 (4)	4.789 1 (16)	−4.8 (20)	This work
	13124.797 (7)	1.313 92 (9)	4.4 (2)		Naus et al. [11]
	13124.802 7 (9)	1.314 031 (14)	4.75 (4)		Schermaul [12]
	13124.800 8 (10)	1.314 051 (8)	4.808 (8)		van Leeuwen et al. [9]
	13124.795 (1)	1.314 12 (1)	5.05 (1)		Babcock and Herzberg [7]
$^{17}O^{18}O$	13125.928 2 (3)	1.273 070 (4)	4.553 (9)		This work
	13125.924 (8)	1.273 19 (8)	4.8 (1)		Naus et al. [11]
$^{18}O_2$	13126.516 15 (3)	1.236 815 8 (4)	4.253 (1)	−2.4 (13)	This work
	13126.932 7 (8)	1.236 833 (6)	4.255 (8)		Naus et al. [11]
	13126.498 (3)	1.236 80 (14)	4.0 (5)		Gagliardi et al. [10]

Molecular constants derived from the expression $E = T + BJ(J+1) - DJ^2(J+1)^2 + HJ^3(J+1)^3$, assuming fixed ground state constants from Table 6.7. Numbers in parenthesis are 1σ fit uncertainty in the last digit. Values of T for the previous studies were adjusted to keep the zero-level of the ground state consistent: see Table 6.8 for the zero-level used for each isotope. The molecular constants reported by van Leeuwen et al. [9] was based on their high-J positions and the low-J positions of Schermaul [12].

The only other study to determine molecular constants for the set of minor isotopologues is that of Naus et al. [11]. Their work used cavity ring-down spectroscopy and reported line position accuracies of 0.03 cm^{-1}. Even with such a low uncertainty, their molecular constants are in generally good agreement (within 2σ uncertainty) of the current work. However, it should be noted their band origin, T, for the $^{18}O_2$ isotopologue is anomalously large compared to the current study and the work of Gagliardi et al. [10]. Babcock and Herzberg [7] reported a centrifugal distortion constant, D, for the $^{16}O^{18}O$ isotopologue significantly larger than that determined in the current work, Schermaul [12], and van Leeuwen et al. [9]. The deviation in the distortion constant is consistent with the observed discrepancies between our observed positions and those listed in HITRAN 2004, where the discrepancy increases quadratically with J. Finally, our results are in excellent agreement with that of Camy-Peyret [8] for the $^{16}O^{17}O$ isotopologue.

Line intensities (near natural abundance), in units of $cm^{-1}/(molecule\ cm^{-2})$, were corrected to T=296 K using,

$$S_i(296K) = S_i(T) \times \frac{q(T)}{q(296K)} \times \frac{e^{-E/k(296K)}}{e^{-E/kT}} \quad , \tag{6.2}$$

where q(T) is the total partition function at temperature T, k is Boltzmann's constant, E is the lower state energy level from HITRAN, and S_i is the line intensity.

To date there are only three measurements of line intensities for the isotopologues of the $b^1\Sigma_g^+ \leftarrow X^3\Sigma_g^-(0,0)$ band [8, 9, 12]. Schermaul [12] measured all four branches of the $^{16}O^{18}O$ isotopologue to J = 20 using FTIR, whereas van Leeuwen et al. [9] measured

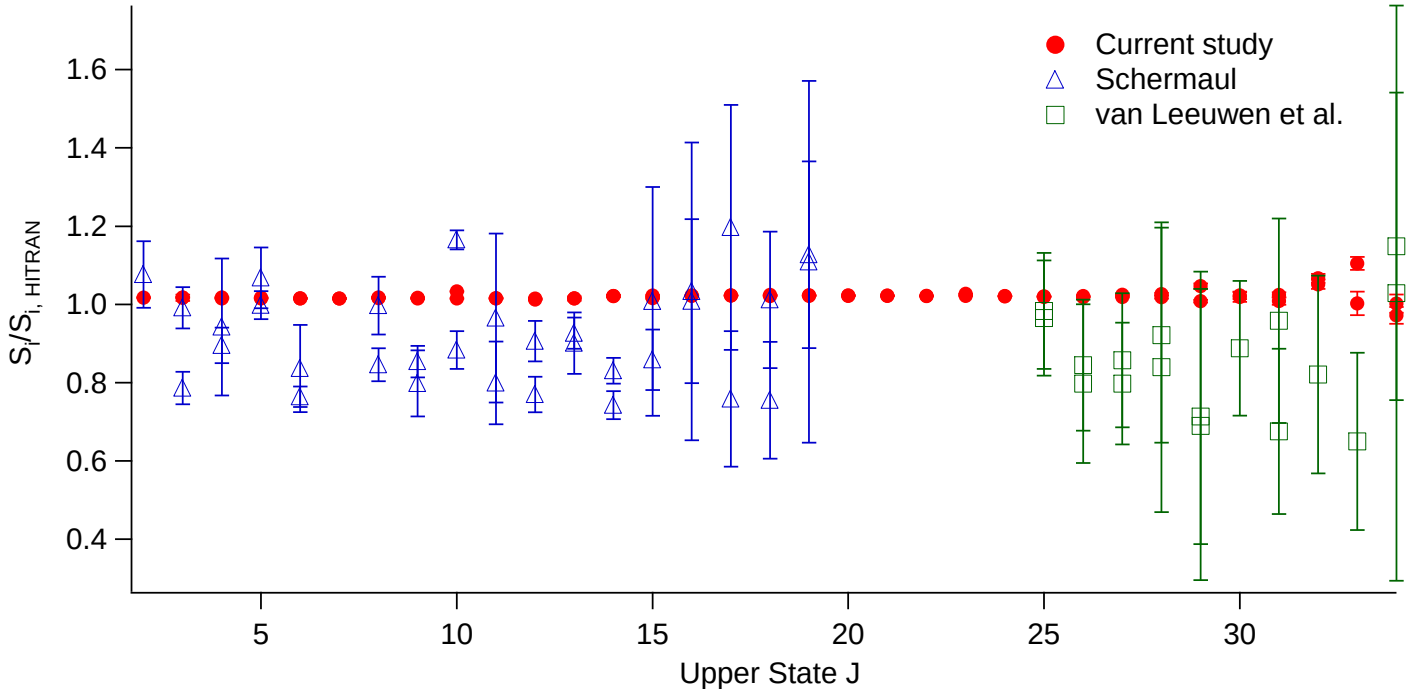

Figure 6.2. $^{16}O^{18}O$ line intensities relative to HITRAN 2004 values. Error bars on the current study represent the fit precision (as described in Table 5.4).

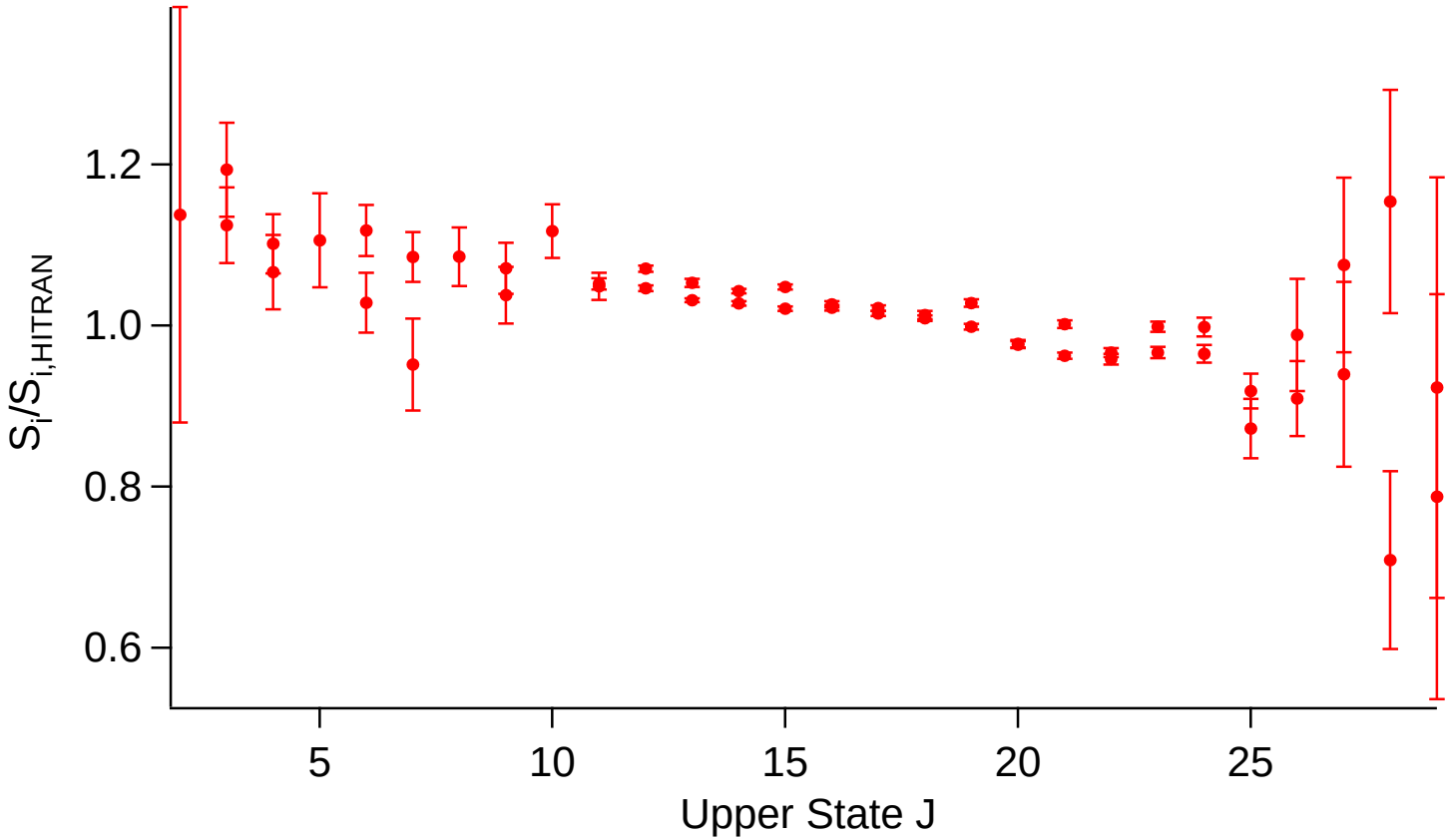

Figure 6.3. $^{16}O^{17}O$ line intensities relative to HITRAN 2004 values.

$^{16}O^{18}O$ line intensities from $25 < J < 35$ in the *PP* and *PQ* branch using NICE-OHMS. Both studies were performed using O_2 with an isotopic composition near natural abundance and have fairly large uncertainties (on average, 12% and 30% for Schermaul and van Leeuwen et al., respectively). The intensities of the $^{16}O^{18}O$ isotopologue in HITRAN 2004 [6] were calculated as described in Gamache et al. [27] and were based on the $^{16}O_2$ bandstrength of Ritter and Wilkerson [28], 2.28×10^{-22} $cm^{-1}/(molecule\ cm^{-2})$. Intensities of the current study, Schermaul, van Leeuwen et al., and HITRAN 2004 are shown in Fig. 6.2. While the intensities of Schermaul and van Leeuwen et al. are (7 ± 13)% and (14 ± 13)% lower than HITRAN, respectively, the values from the current study are (2.1 ± 1.5)% larger.

Camy-Peyret et al. [8] used atmospheric balloon spectra to determine the intensities of many $^{16}O^{17}O$ transitions and is the basis for the $^{16}O^{17}O$ intensities in HITRAN 2004. Our intensities are compared to those of Camy-Peyret et al. in Fig. 6.3. The ratios of our $^{16}O^{17}O$ intensities to Camy-Peyret et al. have a dependence on *J*: +10% at low-*J* and −10% at $J = 28$. This is in contrast to the nearly constant offset of the $^{16}O^{18}O$ intensities. To our knowledge, we are the first to report intensities for the $^{17}O^{18}O$ and $^{18}O_2$ isotopologues.

Pressure broadening coefficients are shown in Fig. 6.4. The coefficients for the $^{16}O^{17}O$ and $^{17}O^{18}O$ isotopologues have considerably more uncertainty due to their lower abundances in the gas sample. As is evident, to within a 2% uncertainty there is no difference between pressure broadening coefficients of the various isotopologues for the

same value of J. The data in Fig. 6.4 were fit using the empirical expression of Yang et al. [5]:

$$HWHM = A + \frac{B}{1 + c_1 J' + c_2 J'^2 + c_3 J'^4} \quad . \tag{6.3}$$

Compared to the self-broadening coefficients reported in Robichaud et al. [13], the current results are (4 ± 2)% larger. Gagliardi et al. [10] used frequency modulation spectroscopy to study the pressure-broadened linewidth with a Voigt profile for the $R11R11$ transition of $^{18}O_2$ in a similarly ^{18}O-enriched sample. They monitored the linewidths by varying both the total pressure of the isotopically enriched sample and by adding various amounts of pure $^{16}O_2$ to a fixed quantity of the enriched sample. They saw the broadening parameter due to the enriched bath gas to be (21 ± 5)% larger than in pure $^{16}O_2$. The corresponding $^{16}O_2$ self-broadening coefficient from HITRAN 2004 [6] was in the middle of the two determinations. Schermaul [12] used a non-standard "collisionally narrowed Voigt" profile to fit their data and reported the $^{16}O_2$ self-broadening coefficients to be (24 ± 10)% larger than the $^{16}O^{18}O$ broadening coefficients (also broadened by $^{16}O_2$). Both studies invoked resonant exchange processes in the collisional model as the cause of the difference between isotopologues, although Schermaul also suggests that the additional rotational states in $^{16}O^{18}O$ due to symmetry may play a role.

The results of Gagliardi et al. and Schermaul are in contrast to the current study. To within 2% uncertainty, the broadening due to the ^{18}O enriched gas is identical for all five of the isotopologues studied and within 4% of the $^{16}O_2$ self-broadening coefficients of our previous study [13]. To further compare our results with Schermaul, we measured

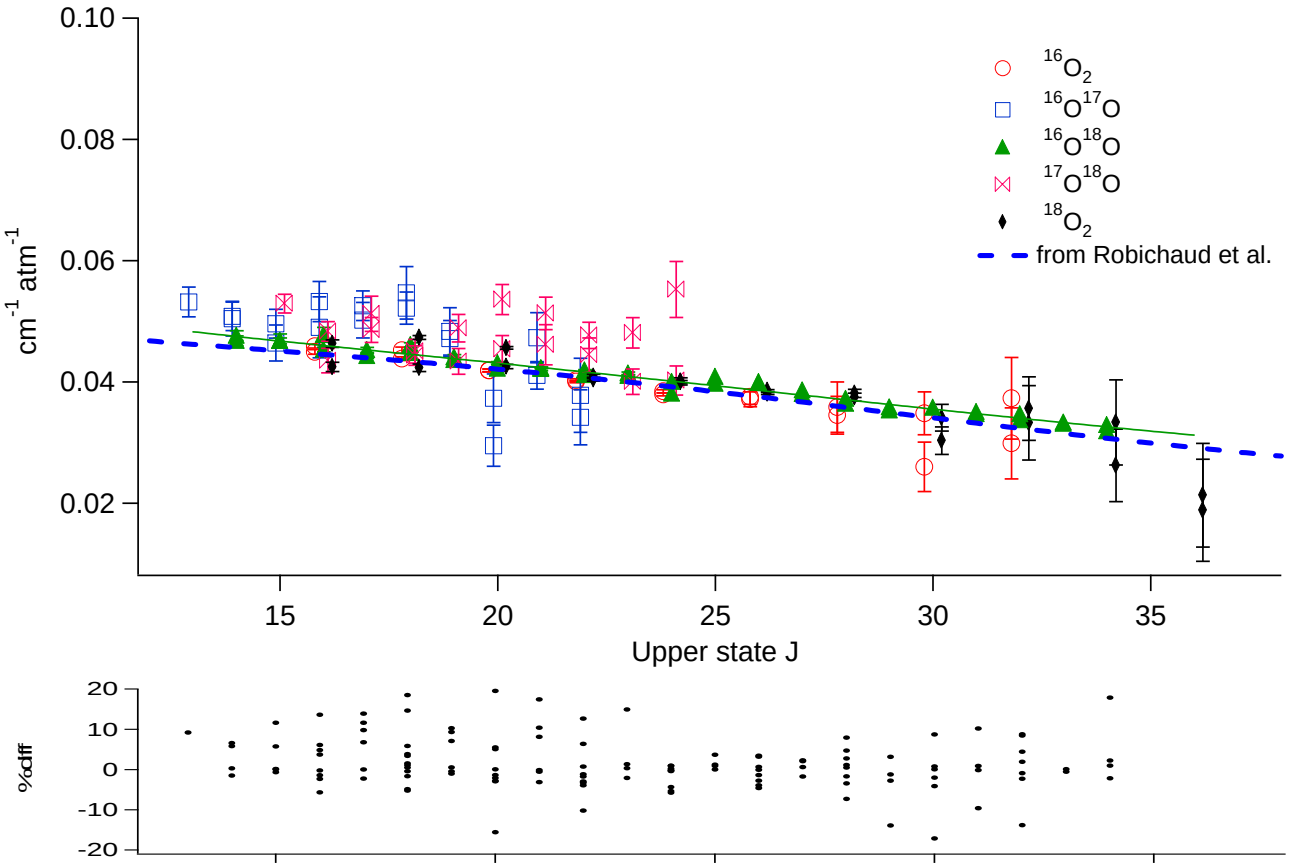

Figure 6.4. Pressure-broadening parameters as a function of upper state J for the isotopologues of the O_2 A-band in units of cm^{-1} atm^{-1} at 296 K. Values for the different isotopologues are offset on the x-axis for clarity. The dashed blue line represents the self-broadening parameters from Robichaud et al. The solid thin line represents fit to all the data shown based on Eq. 5.3 with coefficients of A = 0.02032, B = 0.04791, $c_1 = 0.0674$, $c_2 = -0.001218$, and $c_3 = 1.513 \times 10^{-6}$. Broadening coefficients in the current study are approximately (4 ± 2)% larger than the self-broadened coefficients from Robichaud et al. over the range shown. For the current dataset, there is no discernible difference between the different isotopologues.

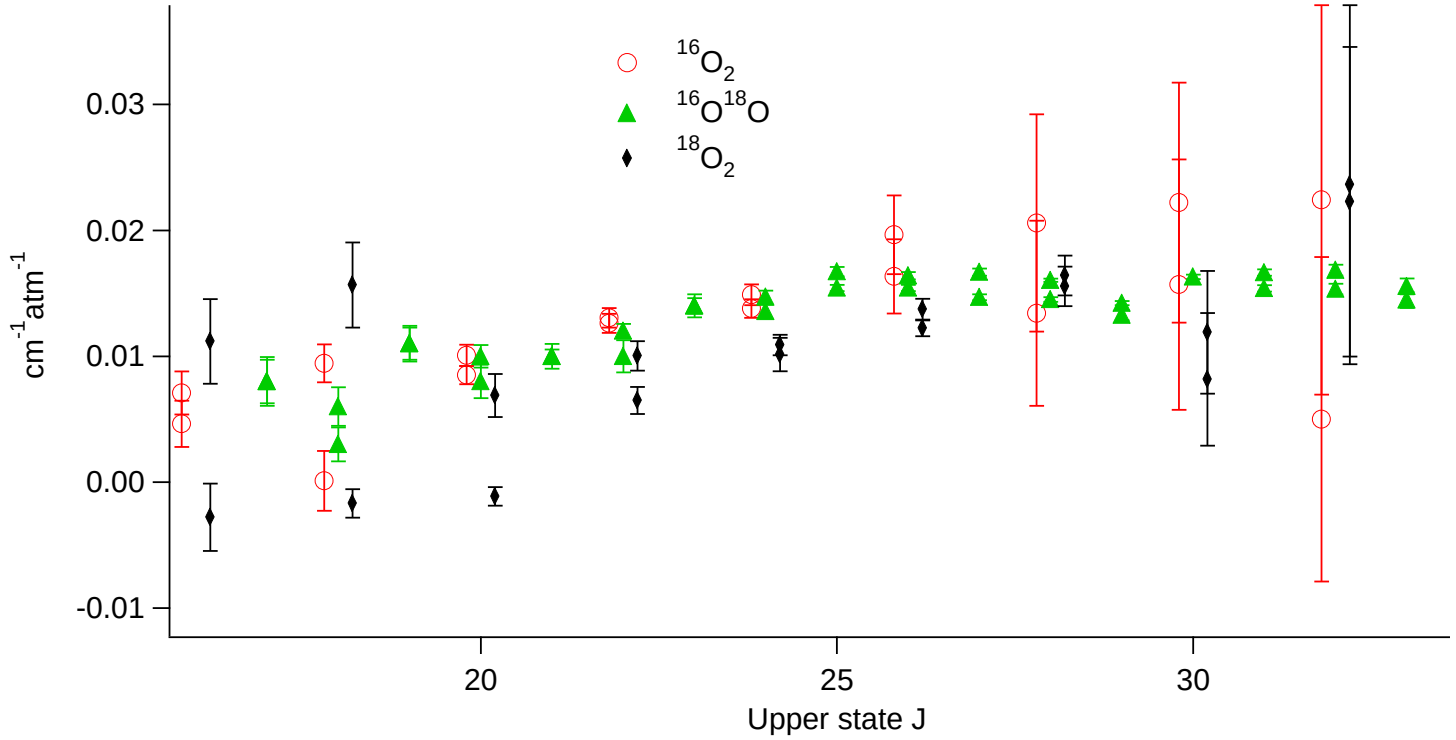

Figure 6.5. Collisional narrowing parameters as a function of upper state *J* for the isotopologues of the O_2 *A*-band in units of cm^{-1} atm^{-1}. Values for the different isotopologues are offset on the x-axis for clarity. The values for the $^{16}O^{17}O$ and $^{17}O^{18}O$ isotopologues are not shown due to their large uncertainties. The narrowing parameters from the current study is (8 ± 16) % smaller than the $^{16}O_2$ results in Robichaud et al. There appears to be a slight lowering of the narrowing parameter with increasing mass of –0.0011 (2) (cm^{-1} atm^{-1})/amu.

the broadening coefficients of three $^{16}O^{18}O$ lines ($P19$ $P19$, $P17$ $P17$, and $P15$ $P15$) in O_2 with an isotopic composition near natural abundance. The measured $^{16}O^{18}O$ broadening coefficients were identical to the $^{16}O_2$ self-broadened coefficients of the same J to within their combined uncertainties and were (4 ± 1)% smaller than the corresponding coefficients broadened by the ^{18}O enriched gas mixture. Given our ability to see subtle lineshape effects (e.g. collisional narrowing, speed dependence) [19], our reasonably high precision, and our good agreement of our $^{16}O_2$ self-broadening coefficients with other high-resolution studies [29], it is unlikely that we would not observe a 20% change in the broadening coefficient. The most likely explanation for the discrepancy between our work and that of Gagliardi et al. [10] and Schermaul [12] is lineshape effects, particularly collisional narrowing as described below.

Collisional narrowing parameters are shown in Fig. 6.5 for the $^{16}O_2$, $^{16}O^{18}O$, and $^{18}O_2$ isotopologues. The $^{16}O^{17}O$ and $^{17}O^{18}O$ are not shown due to their larger uncertainties. Of the three isotopologues shown in Fig. 6.5, there is a slight change in narrowing parameters for a given J of $-(0.0011 \pm 0.0002)$ (cm^{-1} atm^{-1})/amu when considering the highest precision data from $20 < J < 26$. This is in agreement with the collisional narrowing study of Ritter [28] in which he studied the narrowing parameter as against the series of noble gases. Ritter's work indicates a value of -0.0003 (cm^{-1} atm^{-1})/amu, which is the same sign and order of magnitude as our study. Therefore, if the collisional narrowing parameter were considered constant for all of the isotopologues, the pressure broadening parameter would err on the order of a few percent depending on the

isotopologues considered. This may account for the discrepancies in the pressure broadening parameter described above.

6.5 Conclusions

Experimental lineshape parameters have been determined for the $^{16}O_2$, $^{16}O^{17}O$, $^{16}O^{18}O$, $^{17}O^{18}O$, and $^{18}O_2$ isotopologues. The $^{17}O_2$ isotopologue was not studied due to its low abundance and signal-to-noise. Molecular constants for the excited $b^1\Sigma_g^+$ states have been determined and are in good agreement with previous studies. The current edition of HITRAN [6] has recently updated their $^{16}O^{17}O$ linelist using the Camy-Peyret et al. [8] results and are in good agreement with our numbers. However, the $^{16}O^{18}O$ linelist is still based on the original work of Babcock and Herzberg [7] and in disagreement with this work and others [9, 11, 12], by up to 0.3 cm^{-1} for $J' = 34$. These line positions should be updated in the databases.

Pressure broadening coefficients are similar for the 5 isotopologues studied and are ~4 % larger than the $^{16}O_2$-broadened coefficients of $^{16}O_2$ and $^{16}O^{18}O$. These results are in disagreement with the results of Gagliardi et al. [10] and Schermaul [12] in which large differences are reported when studying the same isotopologue with a different bath gas and different isotopologues broadened by the same bath gas. The use of inappropriate lineshape models (Voigt) or non-standard profiles (collisionally narrowed Voigt) may account for these discrepancies. However, due to the uncertainties in the experimentally determined collisional narrowing parameters it is not possible to

definitively confirm this hypothesis. Based on the current work, it is acceptable to use the $^{16}O_2$ broadening parameters for the other isotopologues for the same *J*.

Acknowledgements

Part of the research described in this paper was performed at the Jet Propulsion Laboratory, California Institute of Technology, under contract with The National Aeronautics and Space Administration (NASA). Additional support was provided by the Orbiting Carbon Observatory (OCO) project, a NASA Earth System Science Pathfinder (ESSP) mission; the NASA Upper Atmospheric Research Program grant NNG06GD88G; and the NIST Office of Microelectronics Program. Laurence Y. Yeung would like to acknowledge the support of the Davidow Graduate Fellowship in Environmental Science. Finally, we would like to acknowledge the assistance of Dr. Mona Shahgholi in performing the mass spectral analyses of our enriched gas sample.

References

[1] D.M. O'Brien, S.A. English, G. DaCosta, J. Atmos. and Ocean. Tech. 14 (1997) 105-119.

[2] K. Chance, J. Quant. Spectrosc. Radiat. Transfer 58 (1997) 375-378.

[3] S. Corradini, M. Cervino, J. Quant. Spectrosc. Radiat. Transfer 97 (2006) 354-380.

[4] B. van Diedenhoven, O.P. Hasekamp, I. Aben, Atmos. Chem. Phys. 5 (2005) 2109-2120.

[5] Z. Yang, P.O. Wennberg, R.P. Cageao, T.J. Pongetti, G.C. Toon, S.P. Sander, J. Quant. Spectrosc. Radiat. Transfer 90 (2005) 309-321.

[6] L.S. Rothman, D. Jacquemart, A. Barbe, D.C. Benner, M. Birk, L.R. Brown, M.R. Carleer, C. Chackerian, K. Chance, L.H. Coudert, V. Dana, V.M. Devi, J.M. Flaud, R.R. Gamache, A. Goldman, J.M. Hartmann, K.W. Jucks, A.G. Maki, J.Y. Mandin, S.T. Massie, J. Orphal, A. Perrin, C.P. Rinsland, M.A.H. Smith, J. Tennyson, R.N. Tolchenov, R.A. Toth, J. Vander Auwera, P. Varanasi, G. Wagner, J. Quant. Spectrosc. Radiat. Transfer 96 (2005) 139-204.

[7] H.D. Babcock, L. Herzberg, Astrophys. J. 108 (1948) 167-190.

[8] C. Camy-Peyret, S. Payan, P. Jeseck, Y. Te, T. Hawat, Paper E4, Proceedings of the International Radiation Symposium, Saint Petersburg, Russia (2000).

[9] N.J. van Leeuwen, H.G. Kjaergaard, D.L. Howard, A.C. Wilson, J. Mol. Spectrosc. 228 (2004) 83-91.

[10] G. Gagliardi, L. Gianfrani, G.M. Tino, Phys. Rev. A 55 (1997) 4597-4600.

[11] H. Naus, A. de Lange, W. Ubachs, Phys. Rev. A 56 (1997) 4755-4763.

[12] R. Schermaul, J. Quant. Spectrosc. Radiat. Transfer 62 (1999) 181-191.

[13] D.J. Robichaud, J.T. Hodges, L.R. Brown, D. Lisak, P. Maslowski, M. Okumura, C.E. Miller, J. Mol. Spectrosc. (2007) submitted.

[14] D.J. Robichaud, J.T. Hodges, D. Lisak, C.E. Miller, M. Okumura, J. Quant. Spectrosc. Radiat. Transfer (2007) doi:10.1016/j.physletb.2003.10.071.

[15] D.J. Robichaud, J.T. Hodges, L.Y. Yeung, P. Maslowski, M. Okumura, C.E. Miller, L.R. Brown, J. Mol. Spectrosc. (2007) submitted.

[16] J.T. Hodges, R. Ciurylo, Rev. Sci. Instrum. 76 (2005) 023112.

[17] J.T. Hodges, H.P. Layer, W.W. Miller, G.E. Scace, Rev. Sci. Instrum. 75 (2004) 849-863.

[18] J.T. Hodges, D. Lisak, Appl. Phys. B 85 (2006) 375-382.

[19] D. Lisak, J.T. Hodges, R. Ciurylo, Phys. Rev. A 73 (2006) 012507.

[20] D. Lisak, J.T. Hodges, Appl. Phys. B (2007) doi:10.1007/s00340-007-2691-x.

[21] D. Halmer, G. von Basum, P. Hering, M. Murtz, Rev. Sci. Instrum. 75 (2004) 2187-2191.

[22] L. Galatry, Phys. Rev. 122 (1961) 1218-1223.

[23] G. Rouillé, G. Millot, R. Saint-Loup, H. Berger, J. Mol. Spectrosc. 154 (1992) 372-382.

[24] G. Cazolli, C. Degli Esposti, P.G. Favero, G. Severi, Nuovo Cimento B 62 (1981) 243-254.

[25] M. Mizushima, S. Yamamoto, J. Mol. Spectrosc. 148 (1991) 447-452.

[26] W. Steinbach, W. Gordy, Phys. Rev. A 11 (1975) 729-731.

[27] R.R. Gamache, A. Goldman, L.S. Rothman, J. Quant. Spectrosc. Radiat. Transfer 59 (1998) 495-509.

[28] K.J. Ritter. A High-Resolution Spectroscopic Study of Absorption Line Profiles in the A-band of Molecular Oxygen. University of Maryland, 1986.

[29] L.R. Brown, C. Plymate, J. Mol. Spectrosc. 199 (2000) 166-179.

CHAPTER 7

Spectroscopy of the $\tilde{A}^2E''(v_4=0) \leftarrow \tilde{X}^2A_2'(v_4=1)$ Hotband of the Nitrate Radical using Off-Axis Integrated Cavity Output Spectroscopy

7.1 Introduction

The Nitrate Radical

The nitrate radical (NO_3) is an important species in atmospheric and combustion chemistry [1]. It is nearly non-existent in the daytime due to rapid photolysis in the visible ($\lambda < 700$ nm). However, at nighttime the nitrate radical is the dominant oxidant of the atmosphere, and thus the reactivity of NO_3 with other important atmosphere species has been extensively studied [1]. Yet, despite its apparent simplicity – 4 atoms in a D_{3h} electronic ground state configuration – the electronic structure of NO_3 has perplexed physical chemists. As an open-shell molecule with a C_3 rotational axis, NO_3 exhibits Jahn-Teller effects in its low-lying $\tilde{A}^2E''$ and $\tilde{B}^2E'$ at 7064 and 15089 cm^{-1}, respectively. The $\tilde{X}^2A_2'$ state has recently received a detailed theoretical treatment by Stanton [2]. Of the two excited states, the strong $\tilde{B} \leftarrow \tilde{X}$ transition at 663 nm is easily observed, but the spectrum is highly convoluted due to vibronic interactions, and it is difficult to determine any information about the Jahn-Teller effects from that transition [3, 4]. The electronically forbidden (weakly Herzberg-Teller allowed) $\tilde{A} \leftarrow \tilde{X}$ has only recently received any attention [5-7]. The first complete spectrum is an anion photoelectron spectrum recorded at low resolution by Weaver et al. [7]. Prior to the current work, the only high-resolution study of an $\tilde{A} \leftarrow \tilde{X}$ transition was the diode laser spectrum of a single vibronic band by Hirota et al. [5], indicating that the geometry of the $\tilde{A}^2E''$ state is D_{3h}. Using pulsed cavity ring-down spectroscopy (CRDS), Deev et al. were the first to report on the complete absorption spectrum from 5900-9000 cm^{-1} and have set the groundwork for detailed theoretical treatment of the Jahn-Teller coupling in this state [6, 8]. However, due to the low spectral resolution of the pulsed-CRDS method, they

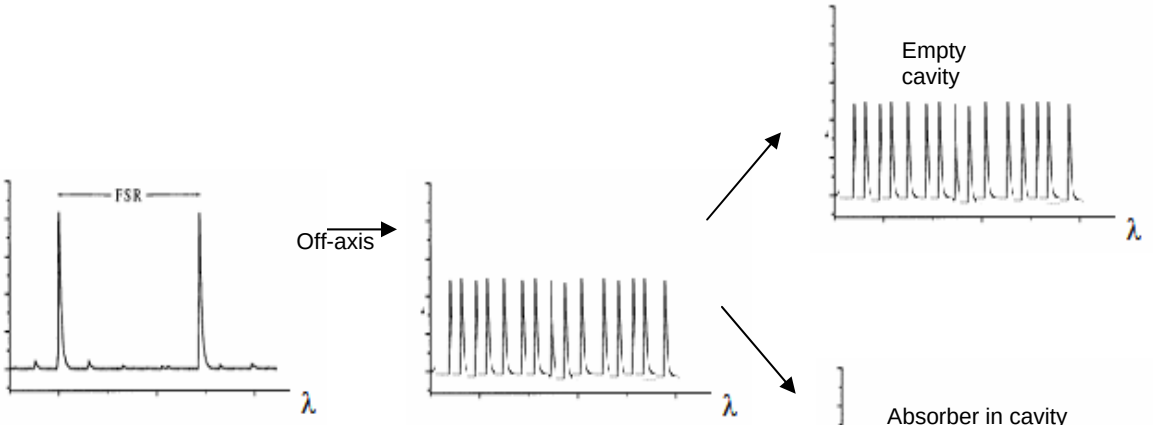

Figure 7.1. Schematic figure of modes in off-axis ICOS. The first figure shows the resonant modes of a cavity aligned on-axis. Changing to an off-axis alignment accesses the transverse modes, increasing the mode density in the region. The output of the cavity is later integrated to produce an absorbance spectrum.

were unable to resolve individual rotational transitions, limiting their ability to determine structural information of the $\tilde{A}^2E'$ state. Yet, contour analyses of the individual vibronic transitions suggest that many of the bands have a C_{2v} structure in the excited $\tilde{A}^2E''$ state. Cavity enhanced, cw techniques should allow for significantly higher resolution spectroscopy of individual vibronic bands. By resolving the rotational sub-structure, new insight can be gained in the Jahn-Teller effects in this state. Therefore, we chose to employ integrated cavity output spectroscopy (ICOS) to study the $\tilde{A}^2E'(v_4=0) \leftarrow \tilde{X}^2A_2'(v_4=1)$ hotband transition at 6700 cm^{-1} to help ascertain the geometry of the vibrationless excited state.

7.1.2 Integrated Cavity Output Spectroscopy

Integrated Cavity Output Spectroscopy (ICOS) was first developed by O'Keefe and coworkers[9] as a simple approach to cavity-enhanced spectroscopy and was later extended to an off-axis alignment by Paul et al.[10] Under normal operation an optical

cavity excited by a cw laser will exhibit high energy build-up when the laser frequency is resonant with a cavity mode, and a near-zero cavity transmission when off-resonance. Attempting to simply match the laser frequency with a cavity mode can suffer from significant noise. Because of the narrow linewidths associated with high-finesse optical cavity (~ 10 kHz), any noise in the resonance of the laser frequency with the cavity mode will result in large fluctuations (~100 %) in cavity transmission, making direct absorption spectroscopy nearly impossible. In cw-ICOS this cavity frequency to transmission noise is significantly reduced by effectively randomizing the cavity mode structure on a time scale faster than the scanning rate of the light source. In off-axis ICOS, the laser is aligned to the cavity in an off-axis arrangement (similar to a Herriot cell) such that the ray paths of the laser are spatially separated over multiple reflections within the cavity before retracing the original path. A cavity aligned in such an off-axis arrangement can be theoretically treated as a cavity that is m time longer, where m is the number of roundtrips before the beam retraces itself. Therefore, a 0.5 m cavity in a 100-pass off-axis alignment will have an effective free spectral range (FSR = $\frac{c}{2nl}$; c, n, and l are the speed of light, index of refraction, and mirror to mirror distance, respectively) of 6 MHz rather than the usual 300 MHz. Once the effective cavity FSR is sufficiently narrower than the laser bandwidth, the fringe contrast ratio approaches unity. In other words, the amount of energy coupled into the cavity is no longer a function of the laser wavelength since the laser is always interacting with at least one cavity mode. Although this condition can be difficult to meet for a fixed laser frequency, scanning the laser through many cavity modes will achieve a very similar effect.

The advantage of off-axis ICOS is that it is relatively simple to set up and can achieve sensitivities within 1-2 orders of magnitude of conventional CRDS setups. Unlike cavity ringdown which requires fast (bandwidth > MHz) detectors and digitizers, ICOS needs only kHz speed electronics. In addition, ICOS does not need optical switches (e.g. acousto-optic modulations), making the ICOS setup significantly more cost effective. However, off-axis ICOS does have several disadvantages. The sensitivity of the technique is much more dependent on the cavity dimensions. For example, off-axis ICOS requires a much larger cavity cross section due to the off-axis alignment; it is generally accepted that 2 inch mirrors are necessary. In addition, the spectral resolution (~30-40 MHz) is typically much worse than CRDS, and there is a direct tradeoff between sensitivity and resolution (discussed below). Furthermore, the scanning speed of the laser frequency can introduce asymmetries in the absorption lineshape. Finally, although the sensitivity is generally good, it is unclear as to how quantitatively accurate ICOS spectroscopy is. For instance, there are questions as to whether biases occur in line intensity determinations using this method.

7.2 Experimental

The ICOS setup is shown schematically in Fig. 7.2. The optical cavity consisted of two 1-m radius of curvature mirrors from Newport (R~99.98%) spaced 85 cm apart. The diode laser (New Focus, model 6323 external cavity diode laser) was mode matched to the optical cavity using a fiber-

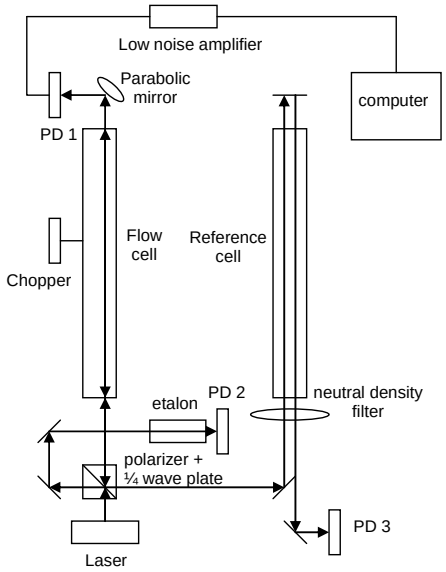

Figure 7.2 Off-axis ICOS experimental setup.

to-free space collimating lens (f = 6.2 mm, OZ Optics). An optical circulator was used to deflect the light reflected from the optical cavity and sent through a reference cell (10 Torr NH_3) and a 5 cm ultra-low expansion (ULE) etalon (FSR ~ 2GHz). Signals from the cavity transmission, etalon, and reference cell were collected on a computer using a low-noise analog-to-digital converter (KPCI-3108). LabView software was used to control the experiment and to process the data.

On-axis alignment of the optical cavity was performed by aligning the laser with respect to the center of the cavity axis. The back mirror is then put in place and adjusted such that the reflected light overlaps the incoming beam. This is repeated for the front mirror. If each mirror is aligned appropriately, then the cavity modes should be evident on the transmission detector by modulating the laser frequency greater than 1 free spectral range (~200 MHz). The alignment can be optimized by observing the mode structure on an oscilloscope, with the intent to maximize the TEM_{00} modes while minimizing all higher order modes. Off axis alignment was achieved by horizontally translating the laser approximately 0.25 cm and tilting it slightly in the vertical direction relative to the center of the cavity.

Generally, off-axis alignment can be confirmed by monitoring the transmission from the optical cavity with a CCD (charged coupled device) camera and observing the "oval" appear (for example, Fig.4 of Paul et al. [10]). In the absence of a CCD camera (as is the case here), the alignment can be optimized by monitoring the signal of an absorption feature. The cavity was charged with ~10 Torr of CO_2, and the line pattern

near 1.497 μm was used to tweak the alignment for maximum signal-to-noise. If the alignment was performed correctly, the mode structure should appear as a densely packed comb of cavity modes of equivalent intensity. It was determined that the reentrant condition (number of passes before the beam retraces its path within the cavity) was ~10 passes, which is significantly less than that achieved by Paul et al.[10] (~400 passes). Our less-than-ideal off-axis alignment was a result of two conditions. First and most important, the inner diameter of the cell is small enough that clipping of the beam likely occurred when attempting to align the setup off-axis. Second, the length of the optical cavity is important in achieving the best off-axis alignment. However, the mirror to mirror distance for these experiments was fixed based on existing components and was not optimized for sensitivity.

The ICOS technique works ideally when the spacing between cavity modes is much smaller than the laser linewidth. In this case, the laser is always on resonance with the cavity. However, in the realm where the mode spacing is larger than the laser linewidth it is necessary to "randomize" the interaction between the laser and modes to achieve a uniform baseline. Typically, randomization is achieved by either rapidly scanning the laser or by modulating the optical cavity length. The time between laser-cavity mode interactions must be small relative to the ringdown time of the cavity to prevent cavity noise. In our experiments, simply scanning the laser was insufficient, and a secondary modulation of the cavity modes was needed. However, our mirror mount design did not allow for the incorporation of a piezoelectric transducer (PZT) to modulate the cavity length. Instead it was decided to mechanically jitter the optical cavity using a

chopper wheel. Although the technique allowed us to average out much more of the cavity-mode noise, it was not ideal.

7.2.1 Sensitivity and Resolution

Due to the nature of the NO_3 experiment, it was important to achieve great sensitivity with excellent resolution. The Doppler width of NO_3 is ~312 MHz at 298 K and 6700 cm^{-1}. It is therefore preferable to have a resolution of 15-30 MHz so that 10-20 data points can be collected per line. In addition, the $\tilde{A}^2E''(v_4 = 0) \leftarrow \tilde{X}^2A_2'(v_4 = 1)$ transition is a hotband going to an electronically-forbidden state. Therefore, each line can be expected to have very weak linestrengths $<10^{-24}$ cm^{-1}/(molecule cm^{-2}). Ideally, the resolution will be determined by the linewidth of the laser (~5 MHz). However, because of the scanning procedure of the ICOS setup, the resolution is typically limited by electronic or optical bandwidth effects.

Early on, the ICOS setup as described above showed a correlation between sensitivity and spectral resolution. Resolution can be calculated by

$$resolution = span(\tfrac{ramp\ freq}{bandwidth}) \quad , \quad (7.1)$$

where *span* is the laser frequency span (~45 GHz), ramp freq is the frequency at which the laser is modulated (typically between 10-50 Hz), and bandwidth is the overall detection bandwidth (3-30 kHz). Two very important features are evident from Eq 7.1. First, the resolution is directly proportional to ramp frequency. It is suggestive that a zero ramp frequency would therefore be ideal for obtaining the highest resolution (limited simply by the laser linewidth). However, the slower the laser ramp the more time the

laser is in the vicinity of a given cavity mode. Therefore, noise in the laser frequency can result in the laser interacting with various cavity modes non-uniformly, resulting in cavity converted laser-frequency-to-amplitude noise. Second, the bandwidth used in Eq. 7.1 is the total of both optical and electronic bandwidths. The optical cavity has an inherent bandwidth of

$$BW_{cavity} = \frac{1}{2\pi\tau} \quad , \tag{7.2}$$

where τ is the ringdown time of the empty cavity and is directly proportional to the cavity finesse. For a moderate cavity finesse of 10,000, a cavity bandwidth of 16 kHz is expected. This cavity bandwidth is typically the limiting bandwidth of the system. Therefore, in order to improve the resolution of the instrument a larger bandwidth (smaller finesse) is desired. However, since sensitivity is proportional to finesse, decreasing the finesse will correspondingly decrease the sensitivity.

7.2.2 NO_3 Production

Nitrate radical (NO_3) was synthesized by mixing ozone with nitrous oxide and cryotrapping the NO_3 as N_2O_5 at –60 °C in an acetone/dry ice bath.

$$NO + O_3 \rightarrow NO_2 + O_2 \tag{R7.1a}$$

$$NO_2 + O_3 \rightarrow NO_3 + O_2 \tag{R7.1b}$$

$$NO_2 + NO_3 \leftrightarrow N_2O_5 \tag{R7.1c}$$

During the experiment, N_2O_5 was stored in a $NaCl/H_2O$ slush at –20 °C. Dry N_2 was flowed (40 sccm) through the N_2O_5 U-tube and into the heated (+360 K) ICOS cell. NO_3 was formed by thermal decomposition of N_2O_5 within the cell, producing approximately 4×10^{14} molecules/cm^3 @ 360 K as monitored by the 662 nm $\tilde{B} \leftarrow \tilde{X}$ transition. An

additional N_2 purge was used to protect the ringdown mirrors from the NO_3 radicals (30 sccm/mirror), generating a purge region of ~10 cm/mirror. The total cell pressure was held near 10 Torr to minimize pressure broadening of the rotational line shapes.

7.2.3 Ammonia Reference Gas

In order to achieve accurate line positions it was necessary to use both a reference gas and étalon. Unfortunately, in this spectral region (6650-6800 cm^{-1}) there are few spectral standards available [11]. Carbon dioxide only covers the region below 6710 cm^{-1}, is relatively sparse (<1 line per wavenumber), and is considerably weak. Water covers above 6700 cm^{-1} quite well; however, the linestrengths are also fairly weak. The best candidate for a reference spectrum was ammonia, as reported by Lundsberg-Nielson et al.[12] However, comparison of the ammonia line positions against carbon dioxide showed a disturbing offset between the Lundsberg linelist and our measurements. Although some of the offset was attributed to systematic error arising from the bandwidth of the ICOS detection relative to the direct absorption of the reference cell, there still remained a large deviation (~0.005 cm^{-1}) that could not be accounted for. Further investigation showed that other groups encountered similar discrepancies [13]; however, no group had as yet published a completed linelist for ammonia in this region. To minimize the uncertainties in the ammonia linelist we

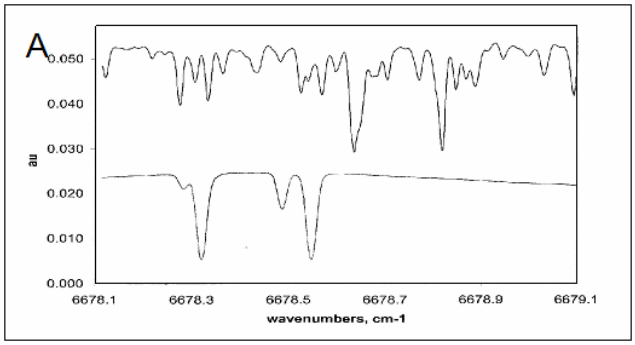

Figure 7.3 Simultaneous scan of NO_3 ICOS spectrum (Top) and NH_3 reference spectrum (Bottom).

recorded the reference ammonia spectrum simultaneously with the ICOS CO_2 and/or water spectra. Recording the reference ammonia spectrum against the ICOS CO_2 spectrum has the added advantage that it should cancel out any systematic errors inherent in the technique (such as the bandwidth deviation mentioned above).

7.3 Results and Discussion

The $\tilde{A}^2E''(v_4 = 0) \leftarrow \tilde{X}^2A_2'(v_4 = 1)$ hotband transition is shown in Fig. 7.4. To date the spectrum has yet to be assigned due to several difficulties. To start, the spectrum is highly dense with rotational transitions in part due to the elevated temperature of the probe region (360 K). Unfortunately, since this transition is a weakly allowed hotband, lowering the temperature to 296 K reduces the signal two-fold: loss of total NO_3 (from 4 $\times$ 10^{14} molecules/cm^3 at 360 K to 1 $\times$ 10^{13} molecules/cm^3 at 296 K due to decreased thermal decomposition of N_2O_5) and loss of $\tilde{X}^2A_2'(v = 1)$ Boltzmann population. In

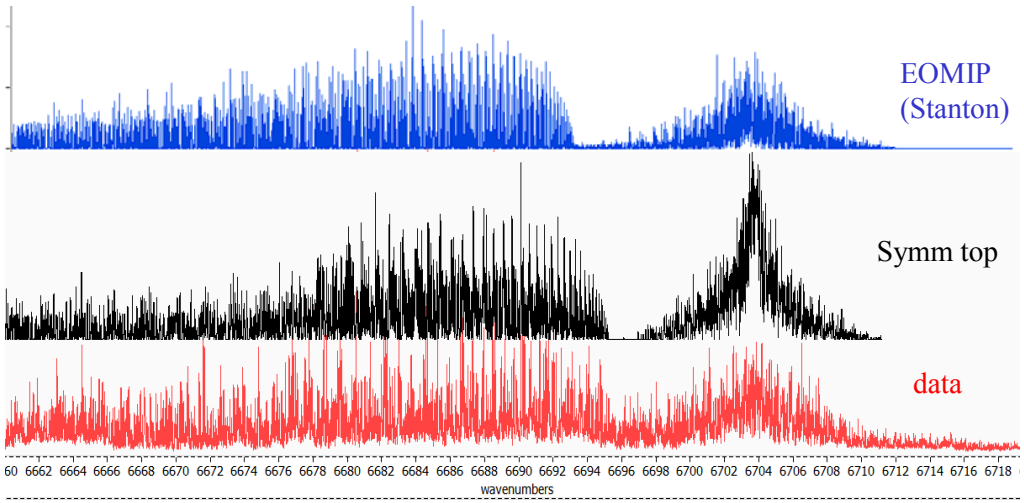

Figure 7.4 Recorded spectrum (bottom) with two simulations based on D_{3h}, symmetric top, excited state and a C_{2v} distorted geometry.

addition, it is still uncertain how to correctly account for the Jahn-Teller and pseudo Jahn-Teller coupling in the excited state. Further study of this spectrum is being carried out by Kana Takematsu of the Okumura group.

7.4 Conclusions

We have shown that the ICOS technique is a cheap and easy method to study spectroscopy in the near-IR. Although this technique may not have been ideally suited for the hotband spectroscopy of NO_3, it should be adequate to study stronger vibronic $\tilde{A}^2E'' \leftarrow \tilde{X}^2A_2'(v=0)$ originating from the vibrationless ground electronic state which are over an order of magnitude stronger due to lower state population density. However, given that the spectral axis of the ICOS technique is largely dependent on external reference gases and étalons, the line positions (absolute or relative) likely have uncertainties ~50 MHz or more. Such uncertainties will translate into increased difficulty in fitting the recorded spectra.

Using the FS-CRDS method which was described in Chapters 1 through 7 of this thesis would have several advantages over ICOS. First, the absolute line positions would be known to <5 MHz, and the spacing between rotational lines would be < 1 MHz. This would be without the need for additional external etalons or references gases (the absolute frequency axis could be linked to the hyperfine components of ^{39}K by frequency doubling). Second, the sensitivity of the FS-CRDS technique is 3-4 orders of magnitude better than that obtained with the off-axis ICOS technique. This would allow us to record spectra at temperatures as low as 250 K, even for the hotband transitions such as studied

here, reducing the rotational state population and simplifying the spectra immensely. Finally, FS-CRDS is highly quantitative and free of instrument-induced asymmetries in the lineshape, reducing unwanted systematic biases that can adversely influence fitting procedures.

References:

[1] B.J. Finlayson-Pitts, J.N. Pitts, *Chemistry of the Upper and Lower Atmosphere: Theory, Experiments, and Applications*. Academic: New York, 1999.

[2] J.F. Stanton, J. Chem. Phys. 126 (2007).

[3] H.H. Nelson, L. Pasternack, J.R. McDonald, J. Chem. Phys. 79 (1983) 4279-4284.

[4] R.T. Carter, K.F. Schmidt, H. Bitto, J.R. Huber, Chem. Phys. Lett. 257 (1996) 297-302.

[5] E. Hirota, T. Ishiwata, K. Kawaguchi, M. Fujitake, N. Ohashi, I. Tanaka, J. Chem. Phys. 107 (1997) 2829-2838.

[6] A. Deev, J. Sommar, M. Okumura, J. Chem. Phys. 122 (2005) 224305.

[7] A. Weaver, D.W. Arnold, S.E. Bradforth, D.M. Neumark, J. Chem. Phys. 94 (1991) 1740-1751.

[8] M. Okumura, J.F. Stanton, A. Deev, J. Sommar, Phys. Scr. 73 (2006) C64-C70.

[9] A. O'Keefe, J.J. Scherer, J.B. Paul, Chem. Phys. Lett. 307 (1999) 343-349.

[10] J.B. Paul, L. Lapson, J.G. Anderson, Appl. Opt. 40 (2001) 4904-4910.

[11] G. Guelachvili, K.N. Rao, *Handbook of Infrared Standards II*. Academic Press: New York, 1993.

[12] L. Lundsberg-Nielsen, F. Hegelund, F.M. Nicolaison, J. Mol. Spectrosc. 162 (1993) 230-245.

[13] J. Orphal, in: PrivateCommunication, (Ed.) 2005.